

Acceleration scenario and necessary devices
for the
KEK-Digital Accelerator

Tanuja Sushant Dixit



The Graduate University for Advanced Studies
School of High Energy Accelerator Science

Acknowledgements

Writing this acknowledgement is indeed a very precious moment for me to express my gratitude to all those who have supported me in undertaking the doctoral course and have helped me in so many ways to achieve it.

First and foremost my very special thanks go to Prof. Ken Takayama, my advisor for this study. His knowledge, enthusiasm, and attention to detail coupled with his ability to motivate towards perfection has made me realize my own abilities. Truly, I feel blessed to have had the opportunity to work on my thesis under his supervision. He even had time to care about my concerns and comfort during my entire study period. I will be able to say an appropriate thank you through my future work.

I would not have been pursuing this course here had it not been for the persistent efforts of Prof. Masayoshi Kawai, who introduced me to Prof. Ken Takayama and KEK. I thank you with appreciation and respect.

During this thesis work I collaborated with many colleagues of the Superbunch group at KEK, and received overwhelming support and co-operation from the entire Superbunch group. I would like to extend my special thanks to Arakida-san for providing me electronic circuits for the experiment, Shimosaki-san for encouraging me and especially for helping me to understand so many things during my initial days at KEK, Iwashita-san for helping in all the technical discussions during my thesis work, and Kono-san and Okazaki-san for helping me assembling the induction cell and setting up the experiment. I thank Hiraoka-san for helping me with all the administrative work, from filling in forms to giving me a ride to the city offices as just some examples. I also found a good friend in her. It has been extremely encouraging to work with so many supportive colleagues. I am truly grateful and appreciative.

I wish to extend my warm thanks to the entire staff of SOKENDAI office who have been so cooperative, helping me with whatever work I approached them with. I also gratefully acknowledge the financial support granted to me by the Japanese government, Monbukagakusho.

Seema Bahinipati had been very supportive and helpful ever since I first arrived at KEK and thereafter I found a loving friend in her. Thank you, Seema, for all your help. I also wish to thank all my friends at KEK who have stood by me at all times.

I owe my thanks to the Director, Society for Applied Microwave Electronics Engineering & Research (SAMEER), Mumbai, the organization where I work, for granting me permission to take up my Ph.D. course. I also extend my warm thanks and regards to all the present and ex-members of the MED group of SAMEER who have encouraged and supported me to undertake this study. I would like to in particular express my gratitude to Mr. Sudhakar S. Bhide for introducing me to accelerators at SAMEER.

I express my gratitude and thanks to my loving parents for supporting me, and my parents-in-law, my entire extended family and siblings for being so encouraging and

supportive and for creating the environment in which undertaking this study seemed so natural.

My husband, Sushant, has been especially supportive and encouraging. It was not an easy decision for me to undertake this study when we had a daughter, four years old. He undertook all the responsibility of bringing up my daughter for three years while I was away. Thank you and I love you so much for making my world so easy and beautiful.

I would like to dedicate my thesis to my daughter, Nandini, who grew up without me for all these years. She has been my source of energy and determination during my entire studies. She is now 7 years old. I have missed her a lot and it is so much satisfying to be about to complete my thesis and to be back with her soon.

Table of Contents

	Page
Abstract	
1. Introduction.....	5
1.1 Particle accelerators.....	7
1.1.1 Electrostatic accelerators.....	8
1.1.2 Linear accelerators.....	9
1.1.3 Cyclotrons.....	10
1.1.4 Betatrons.....	11
1.1.5 Synchrotrons.....	12
1.2 Induction synchrotron.....	13
1.3 Key components of an induction synchrotron.....	14
1.4 Proof-of-principle experiment of the induction synchrotron	19
2. Longitudinal and transverse beam dynamics	22
2.1 Longitudinal dynamics in RF synchrotrons.....	22
2.2 Longitudinal dynamics in the induction synchrotron.....	25
2.3 Synchrotron motion in the induction synchrotron.....	26
2.4 Comparison of the synchrotron motions in RF and induction synchrotrons	32
2.5 Transverse motion.....	35
3. KEK digital accelerator	37
3.1 KEK-PS booster synchrotron.....	37
3.2 The KEK-PS booster as a digital accelerator.....	39
3.3 Required modifications for acceleration.....	41
4. Digital acceleration scheme.....	42
4.1 Pulse density control.....	42
4.2 Staging.....	43
4.3 Intermittent operation and sorting.....	44
5. Simulations.....	46
6. Necessary device - long -pulse induction acceleration cell.....	54
6.1 The droop.....	54
6.2 A 2:1 transformer as a long-pulse induction acceleration cell.....	55
6.3 Characteristics of the 2-turn induction cell.....	56
6.4 Voltage profile of the modified induction cell.....	58
6.5 Sequential and parallel operation of long-pulse induction cells....	61
7. Beam Simulator	62

8. Intelligent acceleration control system for the KEK-DA.....	65
8.1 Stage selector.....	66
8.2 DSP sets for generating dynamic pulse width and amplitude.....	67
8.3 Frequency dividers for intermittent operation	68
8.4 Logic units.....	70
8.5 Induction acceleration control system.....	70
9. Experimental results of the acceleration scheme using a beam simulator	76
10. Conclusion	80
Appendix	
References	
List of figures	
List of tables	
Constants	

Abstract

A novel ion accelerator referred to as a digital accelerator, which is based on the induction synchrotron concept, is discussed here. Its operational performance is the same as that of the induction synchrotron, where acceleration and confinement of ions in the propagation direction are implemented independently with a pulsed voltage and the so-called barrier voltages. These voltage pulses are generated in the induction acceleration cell energized by the switching power supply, which is triggered with a trigger signal manipulated by an ion-bunch signal. In the digital accelerator, any ion species with its possible charge state can be accelerated since the acceleration voltage pulse generation is always synchronized with the ion circulation. Acceleration of argon ions is planned as a proof-of-principle experiment at KEK. The detailed aspects of the digital accelerator are described, including theoretical backgrounds such as beam dynamics.

The KEK-PS booster synchrotron is under renovation, aiming to become the first digital accelerator. The KEK Booster is a rapid-cycle synchrotron where the acceleration voltage amplitude changes dynamically throughout the acceleration period. The existing induction cells can provide a peak output voltage of 2 kV in 250 nsec pulse width at a maximum repetition rate of 1 MHz. Once the peak output voltage is fixed, it is difficult to change its magnitude in the same acceleration cycle. The main purpose of this thesis is to propose the realization of a dynamically changeable acceleration voltage by employing the induction acceleration system. In fact, this idea has been developed for the KEK digital accelerator. The acceleration period is divided into stages, where different acceleration voltages, pulse widths, and repetition rates are required. A novel technique, which consists of staging of the acceleration period, systematic sorting of the induction acceleration cells, and intermittent operation of the induction acceleration systems, has been developed. Particle tracking simulations in the longitudinal direction were performed in order to verify the feasibility of the scheme. The acceleration scheme has been verified experimentally for the first two stages of the acceleration period by using a beam simulator signal. The results will be presented here and the perspectives of this technique will be discussed.

Chapter 1 Introduction

The KEK digital accelerator (KEK-DA) is based on the induction synchrotron (IS) concept [1], which was demonstrated in 2006 [2]. In the induction synchrotron concept, pulse voltages are used to accelerate and confine particles. Almost rectangular-shaped voltage pulses are obtained by 1-to-1 transformers referred to as induction cells, which are energized by individual switching power supplies. The switching power supplies are fired by triggering their solid-state switching elements with digitalized trigger signals, which are generated by the bunch monitor signal. Using the pulsed-power technology newly developed at KEK, these voltage pulses can be generated at frequency values ranging from extremely low to up to 1 MHz, and are synchronized with the circulation of the ion bunch. This property makes the KEK-DA a versatile accelerator which can accelerate any kinds of ions from a very low energy.

The KEK-DA is unique from the operational point of view as it is based on a digital technique referred to as pulse density control. Using pulse density control, fixed output voltages from the induction cells can be modulated over time to provide the required energy gain to the particles. This feature is developed extensively in the KEK-DA acceleration scheme.

The KEK-DA is a modification of the KEK-PS booster ring (BR). BR had been operated at 20 Hz over more than 30 years as a rapid-cycle synchrotron (RCS). The acceleration voltage in an RCS changes dynamically throughout the acceleration period. The output voltage of the induction acceleration system, which has been developed for the IS, is fixed because of the nature of the construction. The most serious issue concerns the implementation of dynamic changes in the required acceleration voltage by the induction acceleration system with a constant output voltage. In addition, the trigger frequency, which is synchronized with the revolution frequency, must be varied over more than two orders of magnitude. The revolution frequency during the acceleration exceeds the maximum switching frequency of the present induction acceleration system.

In order to meet the technical requirements for the acceleration system of the KEK-DA by assuming the existing induction acceleration system with a maximum operation frequency of 1 MHz and 2 kV constant output voltage, a novel and specific acceleration scenario has been explored, and necessary hardware has been developed. The present thesis covers all details related to the acceleration scenario in the KEK-DA and the actual induction acceleration system for the KEK-DA. The noteworthy properties in the developed induction acceleration technique can be summarized as follows.

- (1) A pulse width is varied in accordance to the acceleration and
- (2) The effective acceleration voltage is varied in accordance to the acceleration.

The acceleration scheme combining the 2 μ sec pulse and shorter pulse voltages has been verified with the aid of computer simulation. Furthermore, the necessary long pulse induction cell was developed, and its performance was analyzed. An intelligent acceleration control system was developed for the purpose of maneuvering the long pulse induction cells and the existing short pulse induction cells. The control system was tested using a beam simulator signal as an alternative of the circulating beam, which was developed in order to verify this rather sophisticated acceleration system.

The KEK-DA is a medium-energy synchrotron, and all kinds of ions, including cluster ions in any possible charge state and mass, can be accelerated in a single ring. Such an accelerator should be attractive for researchers in various fields. Irradiation of various ions on metals, magnetic materials, ceramics, semiconducting materials and polymers produces new materials such as nano-wires, nano-transistors, quantum dots and conducting carbon tracks within diamond insulators. Deep implantation of moderate-energy heavy ions can create alloys of bulk size. Warm dense matter science studies will greatly benefit from heavy-ion beams in exploring high-density and high-temperature regions where the equation of state is not yet explored. A cost-effective hybrid cancer therapy can be realized using a single DA, from which protons and carbon ions can be provided. Ion beam mutagenesis is also an attractive and necessary application where the DNA structure of plant seeds is altered to produce new species. We might be able to create new species of plants which can retain their productivity even in the conditions of significant climate changes in this century.

In this thesis, Chapter 1 introduces various particle accelerators, followed by detailed description of the induction synchrotron concept. Its key devices and the proof-of-principle experiment are described. In Chapter 2, the longitudinal dynamics is developed for both cases of RF and induction synchrotrons and transverse dynamics is briefly introduced. Chapter 3 discusses the outline of the KEK-DA. The newly developed acceleration scheme, which is developed for the KEK-DA, is described in detail in Chapter 4. The results of the simulations carried out in order to verify the feasibility of the acceleration scheme are discussed in Chapter 5. The induction acceleration cell for a long acceleration pulse, which is required for the KEK-DA, is described together with its parameters and output waveforms in Chapter 6. The description of the development of the beam simulator is given in Chapter 7, and Chapter 8 describes the details of an intelligent control system for the KEK-DA. Subsequently, the experimental results of the induction acceleration system using a beam simulator signal are given in Chapter 9, followed by the conclusion derived from the results presented in this thesis.

1.1 Particle Accelerators

Machines capable of accelerating charged particles with the help of electromagnetic fields are referred to as particle accelerators. The charged particles can be electrons, protons, heavy ions, radioactive ions or cluster ions. The history of particle accelerators dates back to the 1930's when electrons were accelerated using DC voltage. Present-day particle accelerators have evolved considerably, currently being some of the most sophisticated devices using the latest technology. Particle accelerators can be divided into two main categories:

- a. Linear accelerators and
- b. Circular accelerators.

In linear accelerators, charged particles travel in a straight path, while in circular accelerators the particle trajectory is circular. Normally, electric field is used for accelerating the particles, and magnetic field is used for bending the trajectory of the particles.

Accelerators are indispensable tools for learning about the sub-atomic and sub nuclear dimensions. Relativistic particle beams from accelerators are capable of resolving the internal structure of the nucleus and its constituent sub-nuclear particles, similarly to a microscope. This is possible since the de Broglie wavelength, λ_B of highly energetic particles is smaller than the size of the nucleus, which is $\sim 10^{-15}$ m.

$$\lambda_B = \frac{h_p}{p} = \frac{h_p c}{E} \quad (1.1)$$

where, h_p is the Planck constant, p is the momentum, and E is the energy of the particle. The energy of the particles is expressed in terms of electron volts (eV), where $1 \text{ eV} = 1.602 \times 10^{-19} \text{ J}$. This is defined as the energy gained by an electron as it crosses a potential difference of 1 V. keV (10^3), MeV (10^6), GeV (10^9) and TeV (10^{12}) are also used as units for describing particles with higher energies.

In the past, many large-scale accelerators referred to as "colliders" were constructed for the purposes of particle physics studies in an attempt to understand and reveal the nature of the Universe. Colliders are accelerators in which a collision between two beams rotating in opposite directions is done, releasing very high energies. In this regard, KEKB in Japan collide electrons and positrons for the purpose of studying the CP violation. Tevatron in Fermilab is used to accelerate and collide protons and antiprotons. The scale of the energies handled in these machines can be fathomed by their sizes. The KEKB ring has a circumference of 3 km, and that of the main ring of Tevatron is 6.5 km. The upcoming Large Hadron Collider (LHC) at CERN, Geneva has a circumference of 27 km, and it will be utilized for accelerating protons in opposite directions. This accelerator will be used to search for the Higgs particle, as well as to study super symmetry and dark matter.

Today thousands of small accelerators exist which are used for a variety of applications, from radiotherapy for cancer treatment and material science studies to the treatment of biomedical waste, high energy physics studies and the treatment of radioactive waste among others.

A brief history of accelerator development over the years is provided below in order to understand the evolution of accelerators over time.

1.1.1. Electrostatic accelerators

The first particle accelerator was the electrostatic accelerator [3]. In an electrostatic accelerator, charges are accelerated by a ground potential to a very high potential produced by a high voltage generator, as shown in Fig. 1. The simplest example of an electrostatic accelerator is the electron gun of an ordinary TV set. Electrons flow from the cathode at ground potential towards the anode, which is kept at higher potential. The pioneering work in this field was done by Van de Graaff, and these accelerators are commonly referred to as Van de Graaff accelerators. Electrostatic accelerators can provide voltages of up to ~ 10 MV. This limit arises due to electrical breakdown. For voltages above 1 MV, pressurized gas is used to increase the breakdown limit of the high-voltage components. These accelerators are useful for low-energy applications with moderate beam currents. Normally, they act as injectors to upstream accelerators such as linear accelerators. Nowadays, tandem Van de Graaff accelerators are commonly used in which ions are accelerated from ground to high potential, after which the charge is stripped and accelerated again to ground potential, thus gaining double acceleration in the process. The main limitation of electrostatic accelerators is that the maximum achievable energy which can be obtained is directly proportional to the maximum voltage which can be applied without breakdown. RF accelerators are employed to overcome this limit.

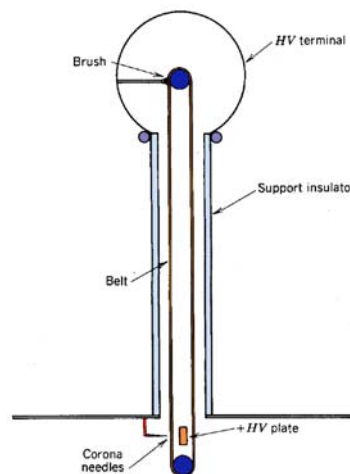


Fig.1. A schematic diagram of the Van de Graaff accelerator

1.1.2. Linear accelerators

In order to overcome the limitations of corona formation and discharge on electrostatic accelerators, Ising (1924) proposed high frequency voltage, i.e. RF voltage. In RF devices, there is no buildup of voltage with respect to the ground. Such devices were first used as linear accelerators. As the name suggests, linear accelerator accelerate particles along a linear trajectory. An abbreviated form linac is commonly used for linear accelerators. Linacs followed electrostatic accelerators and were able to accelerate charged particles to energies above MeV. Earlier linear accelerator had many short accelerating sections, each applying RF voltage. For the proper acceleration of particles, the phase of RF is adjusted in order for particles to "see" rising voltages during the transit through the gap, hence gaining energy, while at other times the particles are shielded from the decelerating RF field by the drift tube. As the particle energy increases, its velocity also increases together with the distance between gaps. As the particle become relativistic, the gap becomes almost constant. This type of accelerator was first developed by Wideroe and later in a modified form by Alvarez [4]. Linacs of the Alvarez type are still used for proton and ion beam acceleration. Linac technology is currently highly developed, giving high voltage gradient per gap and thus becoming shorter in length. The main advantage of using linear accelerators is their capability to produce high energies and high-quality beams. The high-quality attributes are small energy spread and small beam size. In principle, linear accelerators have no limits. Acceleration units can be added indefinitely, thus achieving higher and higher energies. However, the cost of the structure increases as the length increase, which determines the effective limit. Examples of linac include the 40 MeV proton linac of KEK-Proton synchrotron (KEK-PS) shown in Fig. 2, the 2-mile long electron linear accelerator developed at Stanford for acceleration of electrons, and UNILAC at GSI in Germany for the acceleration of ions. The proposed International Linear Collider (ILC) backbone is a linear accelerator. In the proposed design, a 12 km long accelerator section will accelerate electrons to 500 GeV, and another 12 km section will be used for the acceleration of positrons using superconducting cavity technologies. Linac find application as electron-positron colliders for high energy physics experiments, high-quality electron beams for free-electron lasers, pulse neutron sources for material science studies, and X-ray sources for radiotherapy to name a few.



Fig. 2. The 40 MeV Proton linac of KEK-PS

1.1.3. Cyclotrons

Cyclotrons are in the category of circular accelerators. In a circular accelerator, particles are accelerated along a circular path. Magnetic fields are used to bend the trajectory of the particles, and electric fields are used to provide the acceleration. With the ever increasing demand for higher particle energies, the cost of particle accelerators becomes an important factor. Therefore, circular accelerators were developed where particles are injected into a circular orbit, gaining energy at each turn from the RF cavities. When magnetic field is applied in perpendicular direction to the motion of a charged particle, the particle trajectory becomes circular. This principle was used by E. O. Lawrence to accelerate particles in cyclotrons [5]. The governing principle can be simply written as

$$\frac{Mv^2}{\rho} = qvB \quad (1.2)$$

where M is the mass of the particle, v is the velocity, ρ is the bending radius, $q=Ze$ is the charge of the particle, and B is the applied magnetic field. Rearranging Eq. (1.2), we can write

$$v = \frac{qB\rho}{M} \quad (1.3)$$

The time τ required for the completion of one revolution is written as

$$\tau = \frac{2\pi\rho}{v} = \frac{2\pi M}{Bq} \quad (1.4)$$

The angular frequency ω is written as

$$\omega = \frac{qB}{M} \quad (1.5)$$

Thus, the period of revolution does not depend on the velocity or the size of the orbit, but only on the strength of the magnetic field and the charge to mass ratio, since $M = A \cdot m_p$ where A is atomic mass number and m_p is the proton mass. Therefore, if all quantities are fixed, then the oscillator can be tuned to a frequency which alters the polarity of the electrodes referred to as "dees", which are shown in Fig. 3. As the velocity increases, the radius of the path also increases and the particle reaches the dee radius, where it is extracted using extraction electrodes. In early cyclotrons, magnetic field decreased with the radius, putting a limit on the total energy which can be gained due to the increase of relativistic mass. The maximum energy which can be achieved with a cyclotron depends on q/A , where A is the atomic mass number. The limit on the cyclotron is determined by the size of the magnet. These accelerators provide a good balance between cost of the structure and energy of the particles. Hundreds of cyclotrons are used throughout the world for nuclear physics experiments, as well as for industrial and medical applications. The RIKEN superconducting cyclotron facility in Japan can accelerate ions ranging from a single proton to bismuth ions in a wide range of energies. Superconducting cyclotrons use high-field superconducting-magnet techniques with the basic isochronous cyclotron technology (magnetic field changes with the radius, thus causing the revolution frequency to remain constant). This high magnetic field reduces the cost and the size of the cyclotron.

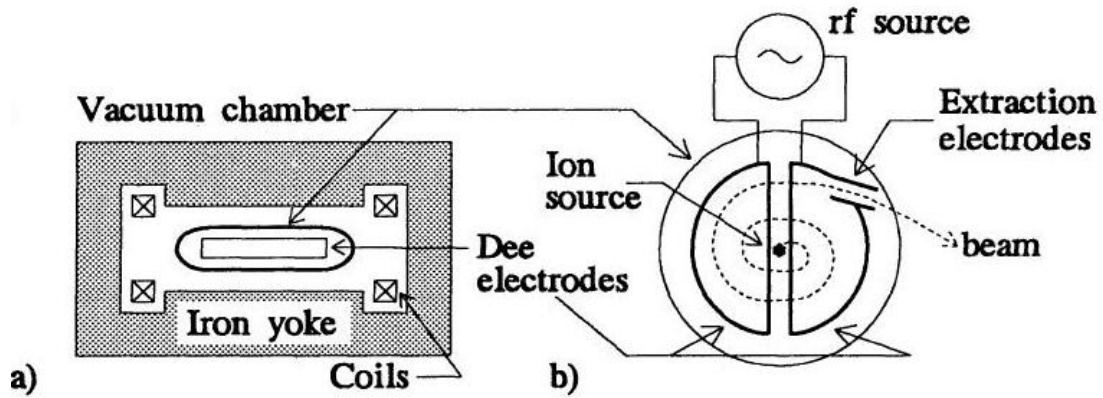


Fig. 3. A schematic diagram of a cyclotron

1.1.4. Betatron

In the cyclotron, the magnetic field remains constant and the radius of the particle trajectory increases together with the applied energy. On the other hand, in betatrons the magnetic field is increased as the particle accelerates, and the radius of the orbit is thus maintained. The acceleration fields are due to the electromotive force generated by the varying magnetic field, and this effect is also known as Faraday's law.

$$\int \vec{E} \cdot d\vec{l} = - \int_s \frac{d\vec{B}}{dt} \cdot d\vec{S} \quad (1.6)$$

The betatron makes use of the transformer principle where the secondary coil is replaced by the circulating beam in a closed doughnut-shaped vacuum chamber, as shown in Fig. 4. Betatrons were the first induction-based circular accelerators [6]. Transverse particle oscillation was first observed in a betatron, and the oscillation is now referred to as betatron motion for this reason. The magnetic fields in a betatron and the size of the magnet determine the upper limit on the maximum achievable energy. Most betatrons are used for accelerating electrons and producing hard X-rays for medical applications.

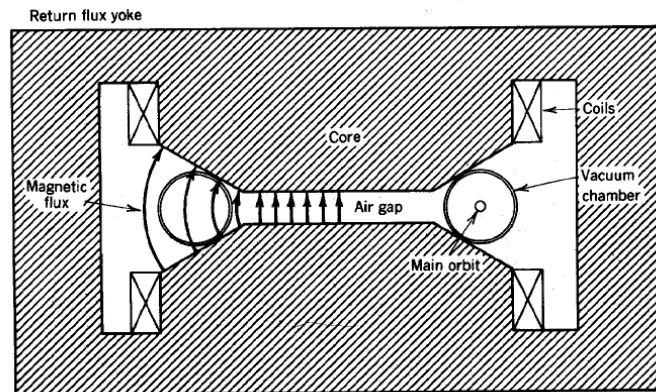


Fig. 4. A schematic diagram of a betatron.

1.1.5. Synchrotrons

Synchrotrons overcome the bulky magnet requirement posed by cyclotrons. For relativistic particles ($v \approx c$), the bending radius, ρ increases together with the energy $E=Mc^2$ according to the following equation

$$\rho = \frac{E}{qcB} \quad (1.7)$$

Instead of allowing particles to spiral outwards as they gain energy, as in cyclotrons, the particles are made to rotate at a constant radius in a synchrotron. Therefore, for a constant radius, the ratio of E/B should be constant, which means that the magnetic field B must be increased synchronously with the energy [7]. The magnets for bending and focusing are arranged in such manner that the particles are confined to an almost circular orbit. This arrangement is referred to as lattice. The lattice can consist of magnets with combined function (the same magnets are used for both focusing and bending) or with separate function (separate magnets for focusing and bending). The magnetic field cannot be varied from 0 to the maximum level, and therefore the ions need to be injected into the synchrotron with some minimum energy. For this purpose, pre-acceleration injectors such as linac are used. Synchrotrons have straight sections for injection, extraction, RF cavities, vacuum stations, and auxiliary magnets. The acceleration voltage V_{ac} is written as (Appendix A)

$$V_{ac} = \rho C_0 \frac{dB}{dt} \quad (1.8)$$

where C_0 is the circumference, and the changing magnetic field, dB/dt needs to be controlled accurately for the proper acceleration of the particles. Usually, V_{ac} is written as

$$V_{ac} = V_{rf} \sin \phi_s \quad (1.9)$$

where V_{rf} is the RF voltage provided by the RF cavity, and ϕ_s is the phase of the ideal particle referred to as synchronous particle. The phase of the particle is controlled in real time to provide the design acceleration voltage to the particles. Thus, control becomes important in these machines, where it is usually provided by RF feedback systems.

To date, synchrotrons produce the highest energies, usually reaching TeV. KEK-PS, shown in Fig. 5, is a 12 GeV proton synchrotron, KEKB is an 8 GeV electron-positron collider, JPARC has a 3 GeV and a 50 GeV ring for protons, and LHC is a 7 TeV proton-proton collider.



Fig. 5. KEK-12 GeV proton synchrotron ring composition

1.2 Induction synchrotron

The concept of induction synchrotron (IS) was proposed by Takayama and Kishiro in 2000 for the purpose of overcoming the limits posed by RF acceleration [1].

In this concept, the acceleration and the confinement of the particles is achieved independently by using two transformers instead of the resonant cavity in the RF synchrotron. The almost rectangular-shaped voltage pulses are obtained by 1-to-1 transformers referred to as induction cells, which are energized by individual switching power supplies. The switching power supply is fired by triggering solid-state switching elements (power MOSFET) with trigger signals generated in a digital signal processor, DSP, where the bunch monitor signal is manipulated digitally. Consequently, the acceleration and the confinement are automatically synchronized with the beam revolution. The IS concept was demonstrated in its complete form in a proof-of-principle experiment in 2006 [2]. The principle is shown in Fig. 6(a) together with that of the RF synchrotron.

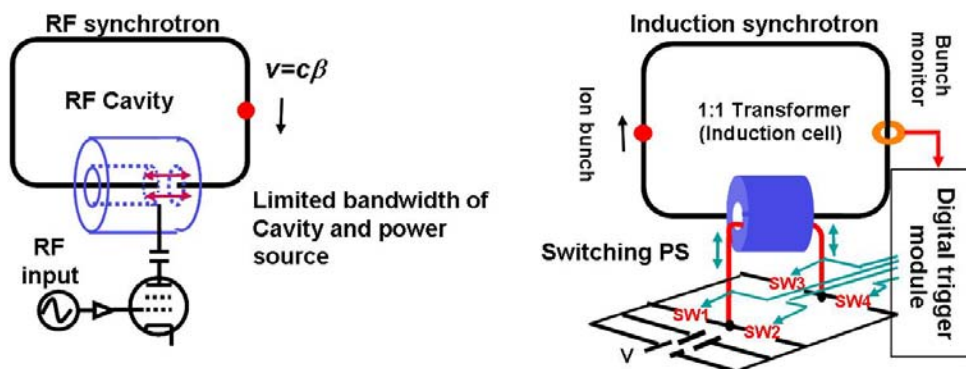


Fig. 6(a). A Schematic diagram of the RF synchrotron and the induction synchrotron.

This characteristic feature allows us to accelerate any ions in any of their possible charge states from an extremely low energy to high energy in a single ring. Namely, an injector-free synchrotron can be realized as shown in Fig. 6(b).

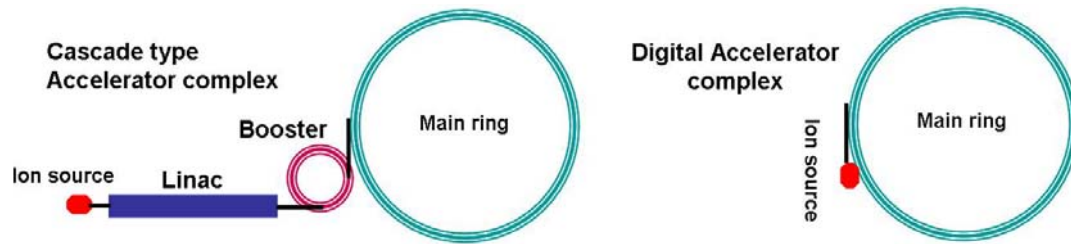


Fig. 6(b) Accelerator configuration

The acceleration and the longitudinal confinement of the charged particles are independently carried out using induction pulse voltages, as shown in Fig. 7. A long-pulse voltage generated in the induction acceleration cells provides the acceleration voltage. A pair of pulse voltages with opposite signs, which is generated in other induction cells, is capable of providing longitudinal focusing forces. This property is rather effective for increasing the freedom of beam handling in longitudinal direction. By increasing the time duration between barrier voltages used for confinement, the longitudinal phase space, which is available for capturing ions, is effectively expanded to increase the average beam intensity while keeping the local line density below the transverse space-charge limit.

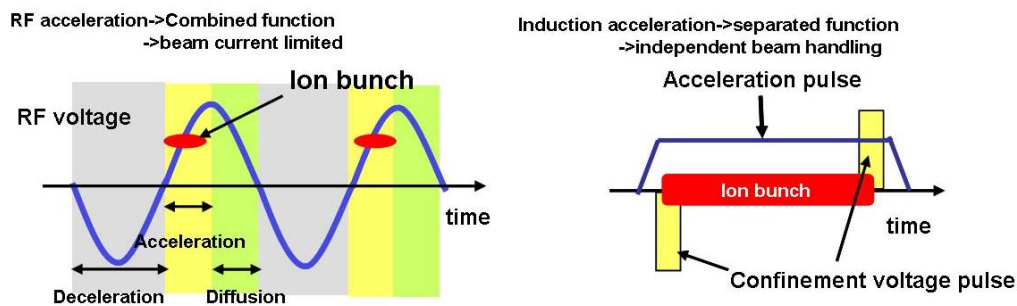


Fig. 7. Voltage profile of the induction synchrotron

The equivalent circuit diagram of the induction acceleration system is shown in Fig. 8. A DC power supply (DC-P.S.) energizes the switching power supply, and the high-voltage pulses are transferred to the induction cell via a 120Ω transmission line. A matching resistance Z is connected in parallel to the induction cell to minimize reflections. R is the resistance representing the core loss. L is the inductance of the magnetic material, and C is the capacitance of the induction cell. In essence, the induction cell works as a 1:1 transformer, where the beam sees almost the same voltage as the one supplied by the DC P.S.

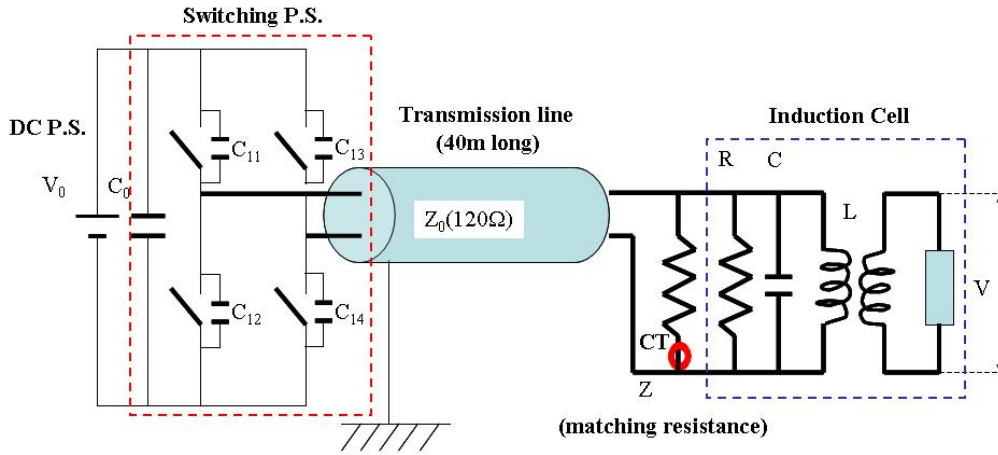


Fig. 8. Equivalent circuit for an induction acceleration system.

1.3 Key components of the induction synchrotron

The key components of the induction synchrotron are the induction cells, which provide pulse voltages, the switching power supply, which drives the cells, and a gate trigger control system, which fires the solid-state switching elements of the switching power supply. The following section will elaborate on these key components.

Induction cell

The induction cell is a key device in the induction acceleration system. The present induction cell was developed for the proof-of-principle experiment of the induction synchrotron using the KEK-PS, which was operated at a repetition rate of 667-882 kHz. The voltage induced through the induction cell is given by the following relation

$$V_{ind} \cdot \tau_p = -B_{max} \cdot k \cdot S \quad (1.10)$$

where V_{ind} is the induced voltage, τ_p is the pulse length, B_{max} is the maximum flux, k is the number of disks, and $S = w \cdot d$ is the cross-section of the single disk-shaped magnetic material of thickness d and width w . The choice of magnetic material was very important due to high repetition rate, where a magnetic material with high permeability and low core loss was desired. Therefore, Finemet[®] FT-3M was used in the induction cell [8,9]. It is a nanocrystalline alloy with very high relative permeability, $\mu \sim 10^4$. The core loss depends on the excitation rate dB/dt and the flux swing ΔB . Therefore, core operation in a small B-H loop is desired. In the present design, ΔB is restricted to under 0.2 T. The magnetic core, being prone to corrosion, is cooled with silicon oil with a flow rate of 80 l/min. The oil is in turn cooled by water through a heat exchanger. The total heat load was estimated to be 18 kW. The cross-sectional view of the developed induction cell is shown in Fig. 9 [10]. Each induction cell consists of 6 Finemet[®] bobbins. The electrical parameters of the induction cell are given in Table 1. The maximum output voltage of the present induction cell is 2 kV. The induction acceleration cell is connected to the switching power supply by a 120 Ω transmission line. In order to ensure the proper matching with the transmission line impedance, a matching resistance of 210 Ω is connected in parallel to the induction cell.

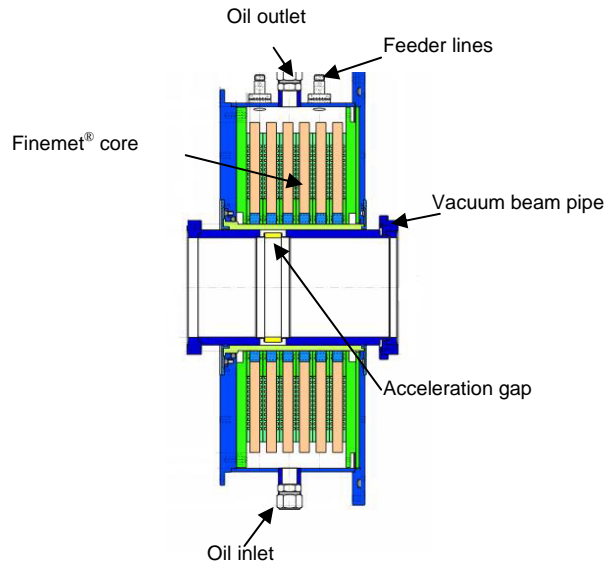


Fig. 9. Cross-sectional view of the induction cell.

Table 1. Electrical parameters of the induction cell

Capacitance	(pF)	260
Inductance	(μ H)	110
Resistance	(Ω)	330

Switching power supply

The switching power supply is a kind of power modulator [11], which is capable of generating bipolar rectangular-shaped voltage pulses at a maximum repetition rate of 1 MHz, as shown in Fig. 10. It consists of a DC power supply and a switching power supply. The switching power supply works as a full bridge circuit consisting of four identical switching arms, where each arm is composed of 7 power metal oxide semiconductor field effect transistors (MOS-FETs), MOS-FET DE475-102N21A by IXYSRF, connected in series. Each arm is capable of handling a maximum of 2 kV and 20 A. The MOS-FET gates are driven by their own gate driving circuits which are electrically isolated with extremely low capacitive DC-DC converters from their primary power source. The gate signals are generated by converting optical signals, which are provided from the pulse controller, into electronic signals. The maximum switching frequency is limited to 1 MHz due to heat deposition problems in the switching elements. The MOS-FET's are attached to a copper heat sink which is cooled by water. The rating of the switching power supply, which was developed in collaboration between KEK and Nichicon Company, is given in Table 2 [12].

Table 2. Specifications of the switching power supply

DC power supply	(kW)	50
Output voltage	(kV)	2.5
Peak output current	(A)	20
Duty of pulse	(%)	50
Power loss at switching element	(W)	200

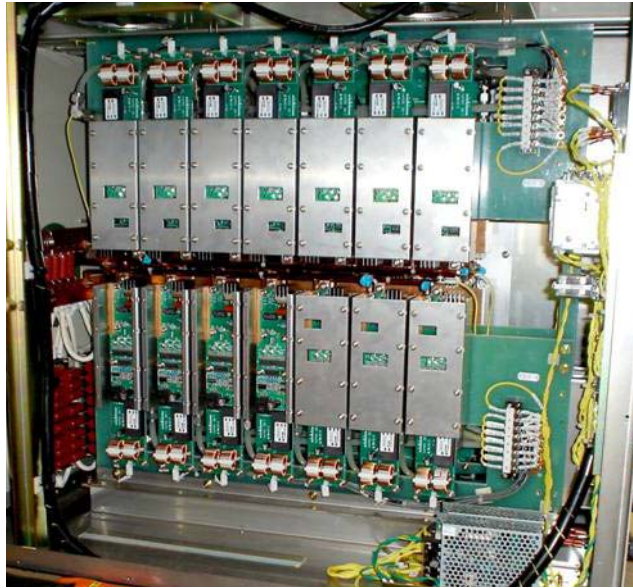


Fig. 10. Switching power supply

The DC Power supply (DC-PS) is used for energizing the switching power supply at a maximum rating of 2.5 kV at 20 A.

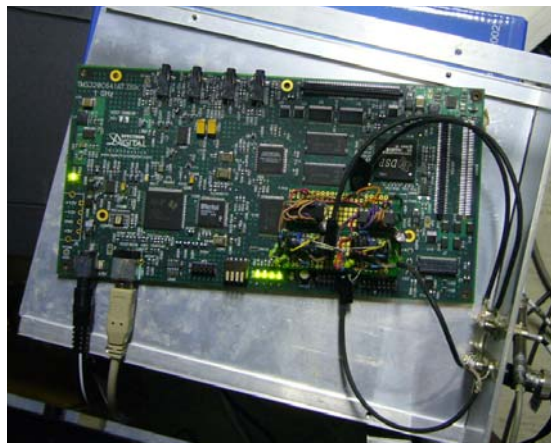


Fig. 11. DSK 6416 unit

The bunch signals are processed with a Texas instruments C6000 series 1 GHz DSP for generating the gate trigger signals for the switching power supply, which is shown in Fig. 11. A master signal for the gate trigger signal is first transferred to an optical trigger unit, which is shown in Fig. 12, and is then divided into the necessary number of signals which need to be sent through an optical fiber cable to individual switching elements in the gate driving circuit, thus maintaining the insulation from the high-voltage circuit.



Fig. 12. Optical trigger unit

The layout of the hardware components is shown in Fig. 13. The induction cells were installed in the main ring of the proton synchrotron. Gate trigger generation and observation was performed at the central control room (CCR). The DC power supply was placed inside the power supply building of the booster magnet, and the switching power supply was placed at a distance from the induction cell in the accelerator tunnel in order to avoid radiation exposure of the switching elements.

Hardware components of Induction Synchrotron

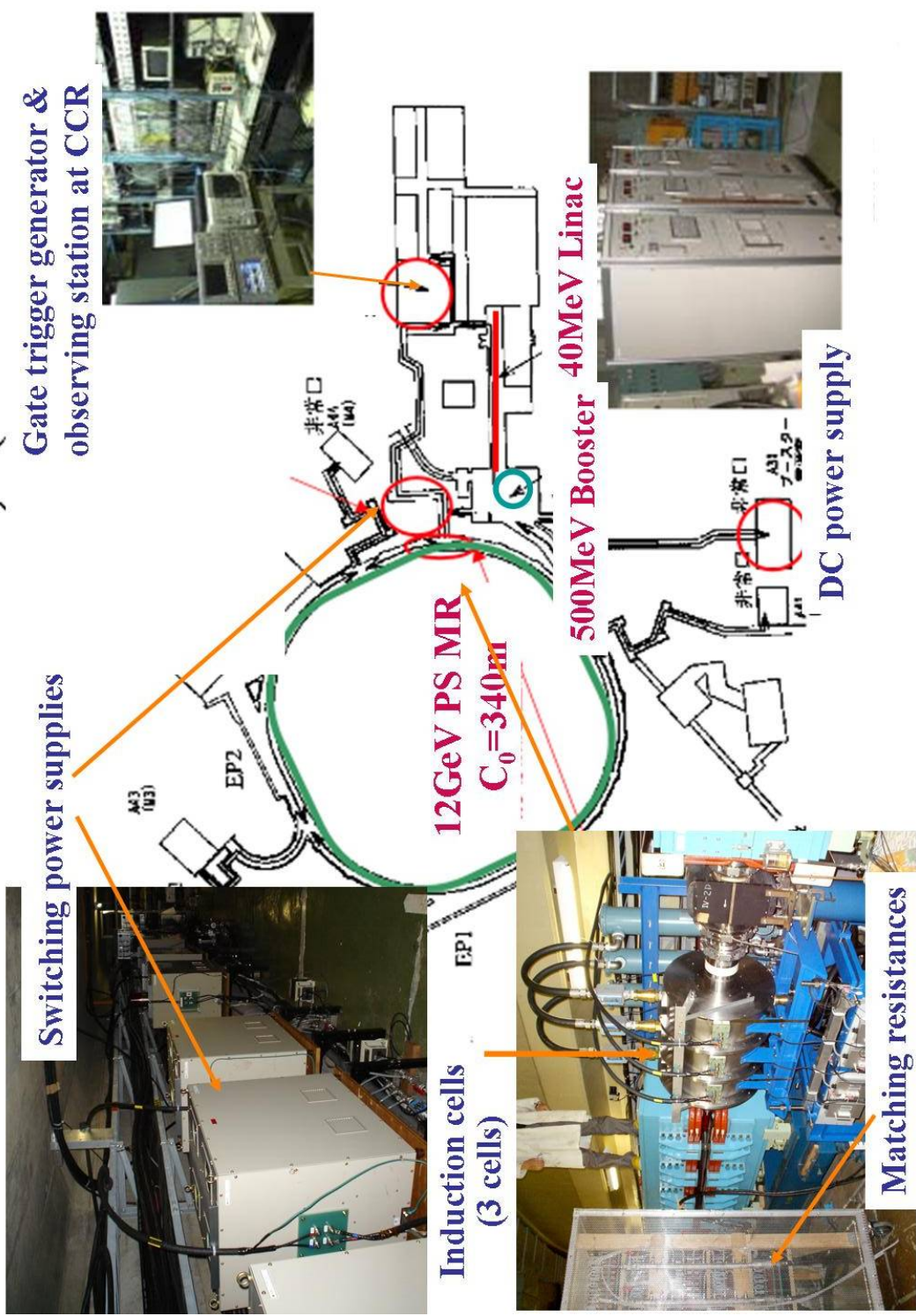


Fig. 13. Hardware components of the induction synchrotron.

1.4 Proof-of-principle (POP) experiment of the induction synchrotron

The induction acceleration experiment was carried out using the KEK 12 GeV proton synchrotron (12GeV-PS) in a series of proof-of-principle (POP) experiments in order to demonstrate the concept of the induction synchrotron. As the first step, the induction acceleration in a high-energy circular ring was demonstrated in 2004 [13], in which a single proton bunch injected from the 500 MeV booster ring and captured in an RF bucket was accelerated from 500 MeV to 8 GeV. This means that a hybrid synchrotron with functional separation in the longitudinal direction had been realized. As the second step, barrier bucket trapping was demonstrated where a proton bunch captured by the induction barrier voltages at an injection energy of 500 MeV survived for more than 450 msec [14]. In the experiment in the third and final step in 2006, particles were confined and accelerated by induction pulse voltages provided by induction cells. The gate signals used to turn on the MOS-FETs were generated in the gate control system by manipulating both signals—one monitored using the fast bunch monitor and the other using the beam position monitor—using a digital signal processor and active delay modules [15]. A schematic diagram of the control system is shown in Fig. 14. The machine and the induction cell parameters are given in Table 3. In this demonstration, the beam-orbit control was the most important issue, as in any other synchrotron. Without this function, charged particles are not efficiently accelerated in the vacuum chamber. The so-called ΔR -feedback system is equipped to meet this requirement similarly to a conventional RF synchrotron, where the RF phase seen by the bunch center is automatically adjusted in real time to compensate for any surplus or shortage of acceleration. A similar feedback system [15], where the gate pulse generation was determined by integrating the digital gate pulse generator with the orbit information proportional to the momentum error, $\Delta p/p$, was introduced in the IS. The beam position monitor directly gives $\Delta R = D(s)\Delta p/p$, where $D(s)$ is the momentum dispersion function at the location of the beam position monitor. When the signal amplitude exceeds a preset threshold value, the gate trigger signal is blocked in the DSP. Accordingly, the acceleration voltage pulse is not generated in the next turn, and the momentum of the bunch centroid approaches the correct value, which is uniquely determined by the bending field. Throughout the acceleration process, the central orbit of the bunch was kept at a constant value, as expected.

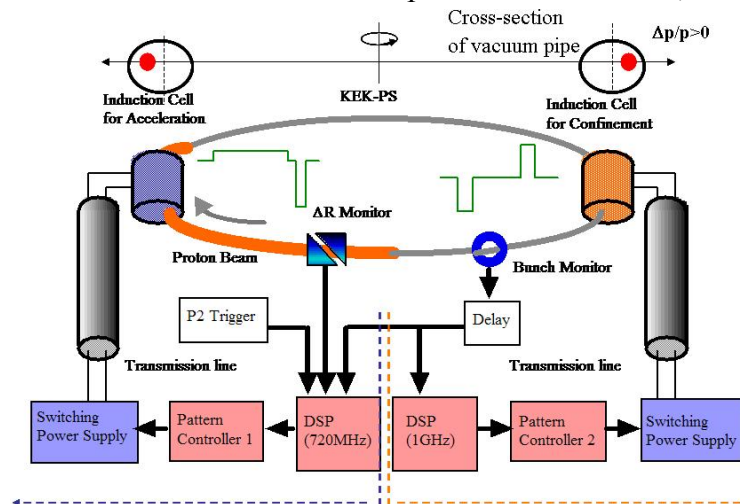


Fig. 14. A schematic diagram of an induction synchrotron control system used in the POP experiment.

The results of the proof-of-principle experiment are shown in Fig. 15. The KEK PS is essentially a slow cycling synchrotron. It was operated at a repetition rate of 0.25 Hz for this experiment. Its operational pattern in the present experiment is composed of a constant minimal field period of about 450 msec and an acceleration period of 2.2 sec for the 6 GeV acceleration pattern. A single proton bunch with an energy of 500 MeV was injected from the booster ring into the main ring and was accelerated to an energy of 6 GeV, which was determined by the ramping pattern of the bending magnet. The first waveform is the ΔR signal, which shows the orbit of the beam throughout the acceleration process. The slow intensity monitor signal (yellow) shows some beam loss at the beginning and 400 msec after the onset of the acceleration. Furthermore, the acceleration voltage pulse is shown in pink, the bunch monitor signal is shown in blue, and the magnet ramping profile is shown in orange.

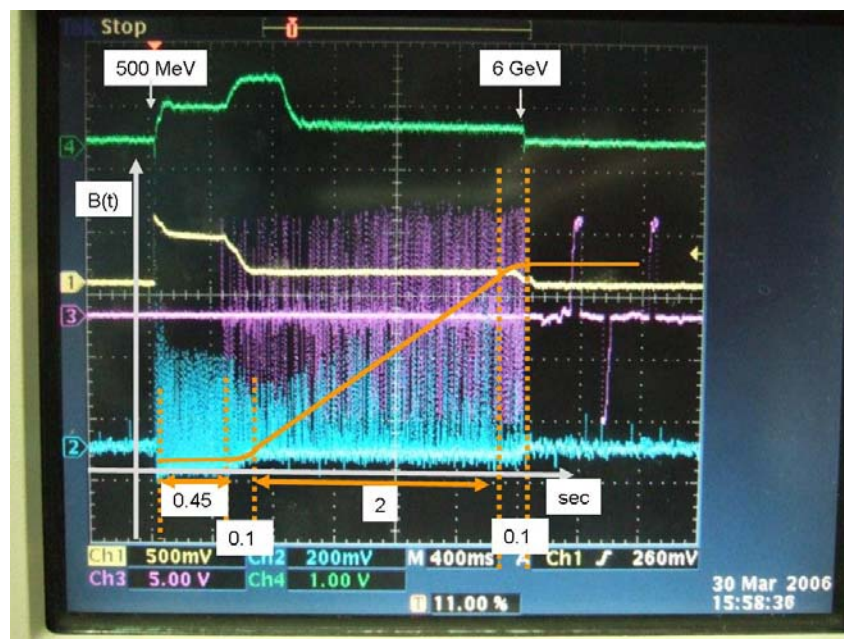


Fig. 15. Results from the proof-of-principle experiment of the induction synchrotron. From top to bottom, ΔR feedback signal (green), slow intensity monitor signal (yellow), acceleration voltage pulses (pink), bunch monitor signal (blue), and bending magnet ramping pattern (orange).

Table 3. Machine and induction cell parameters for the POP experiment

Machine parameter	Value
Injection energy (MeV)	500
Transition gamma, γ_t	6.63
Circumference, C_0 (m)	339.48
Bending radius, ρ (m)	24.4
Induction parameter	Value
Acceleration voltage (kV)	6.4
Barrier voltage (kV)	10.8

Chapter 2 Longitudinal and transverse beam dynamics

In contrast to the RF synchrotron, the functions of acceleration and confinement of particles are separated in the induction synchrotron, as shown in Fig. 7. The longitudinal motion in the case of RF and induction synchrotrons is given in detail in order to distinguish the features in each case [16]. Understanding the concept of longitudinal motion in the induction synchrotron is required for controlling the barrier voltage parameters for the proper confinement of the particles. A detailed derivation of the synchrotron motion in the induction synchrotron is given. The analytical results are verified with the experimental results, obtained during the proof-of-principle experiment for the induction synchrotron, by using computer simulations. The software was then used for longitudinal particle acceleration simulations for the KEK-DA. Transverse motion remains the same for ions (Appendix B).

2.1 Longitudinal dynamics of RF synchrotrons

In the case of RF synchrotrons, energy and phase equations can be written in a discrete form assuming that RF devices are placed at a certain position in the accelerator ring shown in Fig. 16. The synchronous particle is always accelerated with the designed acceleration voltage V , which is uniquely determined by the magnetic ramping pattern of the accelerator given by Eq. (1.8). Its dynamical variable is denoted by a subscript 's'. The schematic of RF voltage and the bunch position is shown in Fig. 17. Two dynamical variables, the energy E and the phase ϕ , are used for developing the model. The former is the total energy of a particle and the latter is defined by $\omega_s t$, where ω_s is the angular frequency of the ideal particle (synchronous particle), and t is the time. These dynamical variables are measured immediately before entering the RF acceleration device. The total energy E gained by a synchronous particle after $(n+1)^{\text{th}}$ turn is given by Eq. (2.1).

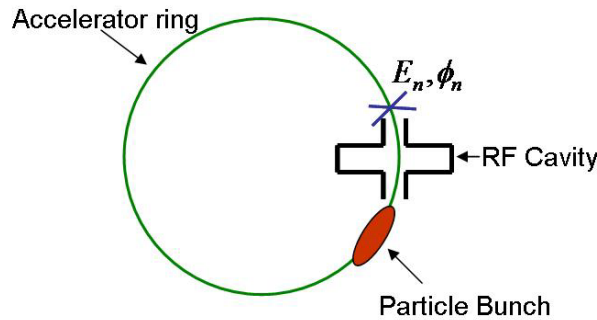


Fig. 16. A schematic diagram of the accelerator ring showing an observation point.

$$E_{n+1}^s = E_n^s + ZeV \sin \phi_s \quad (2.1)$$

where E_{n+1}^s is the energy of the synchronous particle at the $(n+1)^{\text{th}}$ turn

E_n^s is the energy of the synchronous particle at the n^{th} turn
 ϕ_s is the synchronous phase
 V is the acceleration voltage as seen by the synchronous particle
 e is the unit charge
 Z is the charge state of the particle

The energy of an arbitrary particle after $(n+1)^{\text{th}}$ turn is given by

$$E_{n+1} = E_n + ZeV \sin \phi \quad (2.2)$$

where E_{n+1} is the energy of the synchronous particle at the $(n+1)^{\text{th}}$ turn

E_n is the energy of the synchronous particle at the n^{th} turn

ϕ is the phase of an arbitrary particle

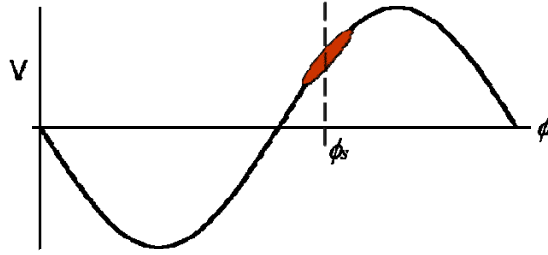


Fig. 17. RF acceleration voltage and synchronous particle phase.

The Difference in energy between an arbitrary particle and the synchronous particle at the $(n+1)^{\text{th}}$ turn is written as

$$\Delta E_{n+1} = \Delta E_n + ZeV (\sin \phi - \sin \phi_s) \quad (2.3)$$

Similarly, the difference in phase between an arbitrary particle and the synchronous particle is written as

$$\Delta \phi_{n+1} = \Delta \phi_n + \eta 2\pi h \left(\frac{\Delta p}{p} \right)_{n+1} \quad (2.4)$$

where
$$\left(\frac{\Delta \tau}{\tau} \right)_{n+1} = \eta \left(\frac{\Delta p}{p} \right)_{n+1} \quad (2.5)$$

$\omega_{rf} = h \omega_s$ is the angular frequency of the RF voltage

h is the harmonic number

p is the momentum

τ is the time to complete one revolution

η is the slippage factor,
$$\eta = \frac{1}{\gamma_t^2} - \frac{1}{\gamma_s^2} \quad (2.6)$$

γ_t is the transition gamma, and γ_s is the relativistic gamma for the synchronous particle.

Changing from the turn variable 'n' to the time variable 't', it is assumed that the energy increments and accordingly the time period increments are small in comparison to the overall time changes, and therefore can be taken as constant over a

small time interval. Introducing a new variable $W = \Delta E/\omega_s$ and taking the average of Eq.(2.3) over a revolution time period of $2\pi/\omega_s$, we have

$$\frac{dW}{dt} = \frac{1}{2\pi} ZeV(\sin \phi - \sin \phi_s) \quad (2.7)$$

and

$$\frac{d\phi}{dt} = \frac{\eta h \omega_s^2}{\beta_s^2 E_s} W \quad (2.8)$$

Equations (2.7) and (2.8) are equations of motion in (W, ϕ) space. Since the parameters change slowly with respect to time, we can assume the Hamiltonian to be independent of time, thus obtaining

$$H(W, \phi) = \frac{\eta h \omega_s^2}{2\beta_s^2 E_s} W^2 + \frac{ZeV}{2\pi} (\cos \phi - \cos \phi_s + (\phi - \phi_s) \sin \phi_s) \quad (2.9)$$

The Hamiltonian contour plot below the transition energy is shown in Fig. 18. The particles which lie inside the separatrix are stable, and particles which lie outside the separatrix are neither bound nor accelerated. The area of the separatrix decreases as the synchronous phase increases for the same RF voltage. Therefore, the number of particles which can be accelerated are limited in the case of RF synchrotron.

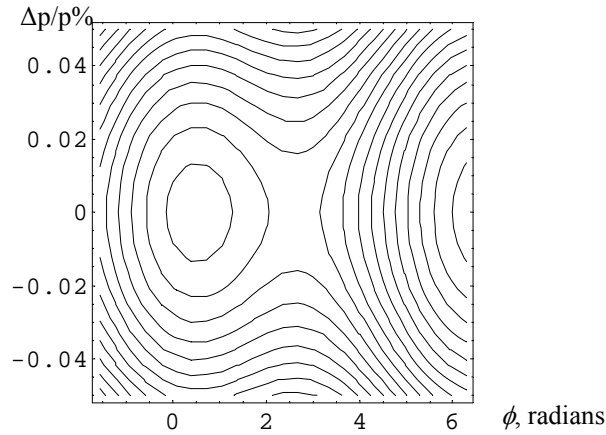


Fig. 18. Hamiltonian contours in phase space for the RF voltage

For small amplitude phase oscillations, i.e. $\Delta\phi = \phi - \phi_s \ll 1$, we can write

$$(\sin \phi - \sin \phi_s) = \sin(\Delta\phi + \phi_s) - \sin \phi_s \approx \Delta\phi \cos \phi_s \quad (2.10)$$

Therefore, Eq. (2.7) can be written as

$$\frac{dW}{dt} = \frac{ZeV}{2\pi} \cos \phi_s \Delta\phi \quad (2.11)$$

$$\frac{d^2(\Delta\phi)}{dt^2} = \frac{\eta h \omega_s^2}{\beta_s^2 E_s} \frac{dW}{dt} = \frac{\eta h \omega_s^2}{\beta_s^2 E_s} \frac{ZeV}{2\pi} \cos \phi_s \Delta\phi \quad (2.12)$$

$$\frac{d^2(\Delta\phi)}{dt^2} + (\Omega_s^2) \Delta\phi = 0 \quad (2.13)$$

The synchrotron frequency Ω_s is given by

$$\Omega_s = \sqrt{\frac{ZeVh\omega_s^2|\eta \cos \phi_s|}{2\pi\beta_s^2 E_s}} \quad (2.14)$$

For stable particle motion, the synchrotron frequency must be real. As η is negative below the transition energy, the synchronous phase is set to be in the range $0 < \phi_s < \frac{\pi}{2}$. Above the transition energy, η is positive, and therefore the synchronous phase is set in the range $\frac{\pi}{2} < \phi_s < \pi$. At the transition energy, the synchrotron motion freezes, and there is no phase focusing.

2.2 Longitudinal dynamics of the induction synchrotron

The induction acceleration cells in the KEK induction synchrotron are localized at several places. For the sake of simplicity, these cells, including the induction cells used for confinement, are represented as a single device in the present acceleration model. Ignoring the transit time through the acceleration device, the changes in E and ϕ per turn can be given by

$$(\Delta E)_{n+1} = (\Delta E)_n + Ze\{V(\phi_n) - V_{ac}\} \quad (2.15)$$

$$\phi_{n+1} = \phi_n + \frac{2\pi\eta h}{\beta_s^2 E_s} (\Delta E)_{n+1} \quad (2.16)$$

where $\Delta E = E - E_s$, $V(\phi_n)$ is the induction voltage as seen by the accelerated particle, as shown later, η is defined as above, and γ_s and β_s are relativistic gamma and beta, respectively. Introducing $W = \Delta E/\omega_s$ as defined earlier, and taking the average over a revolution time period of $2\pi/\omega_s$, we have

$$\frac{dW}{dt} = \frac{Ze\{V(\phi_n) - V_{ac}\}}{2\pi} \quad (2.17)$$

$$\frac{d\phi}{dt} = \frac{\eta h \omega_s^2}{\beta_s^2 E_s} W \quad (2.18)$$

These canonical equations are derived from the following Hamiltonian:

$$H(W, \phi) = \frac{\eta h \omega_s^2}{2\beta_s^2 E_s} W^2 - \frac{Ze}{2\pi} \int_{\phi}^{\phi} \{V(\phi') - V_{ac}\} d\phi'. \quad (2.19)$$

As $V(\phi_n) = V_{bb} + V_{ac}$, the integrand in Eq. (2.19) is simplified. It is reasonable to regard the Hamiltonian as a constant for a short time period, during which the changes in η , β_s , and E_s are rather small. A typical contour for the Hamiltonian is shown in Fig. 19.

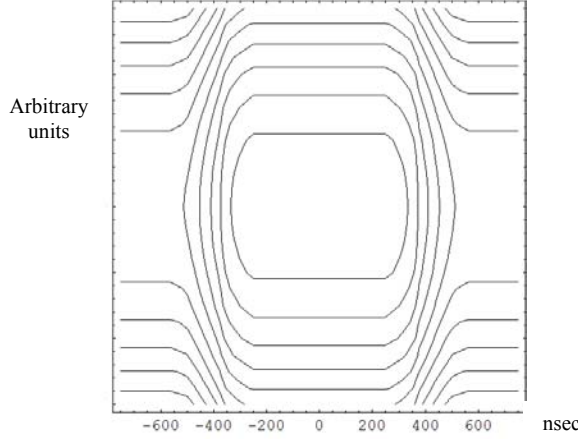


Fig. 19. A schematic diagram of the Hamiltonian contours in an induction synchrotron.

The bucket height in the case of the induction synchrotron can be calculated from the Hamiltonian given in Eq. (2.19). If $V(\phi') = V_{bb}(\phi) - V_{ac}$, then the Hamiltonian reduces to

$$H(W, \phi; t) = \frac{\omega_s^2 \eta}{2\beta_s^2 E_s} W^2 - \frac{Ze}{2\pi} \int_{\phi'} V_{bb}(\phi') d\phi' \quad (2.20)$$

For the rectangular barrier voltage profile shown in Fig. 20, where the barrier amplitude is V_{bb} , $\phi_{pulse} = \omega_s \tau_{pulse}$ and τ_{pulse} is equal to the flat top time, the integration of $V(\phi')$ gives $V_{bb} \tau_{pulse} \omega_s$. No rise time and fall time is assumed. Therefore, we can write

$$H(W, \phi; t) = \frac{\omega_s^2 \eta}{2\beta_s^2 E_s} W^2 - \frac{Ze \omega_s V_{bb} \tau_{pulse}}{2\pi} \quad (2.21)$$

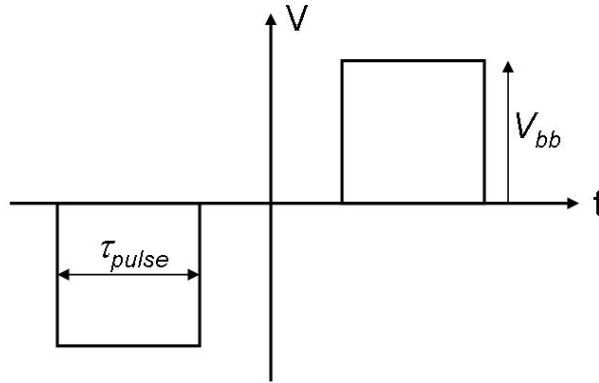


Fig. 20. Voltage profile of the rectangular barrier

In order to calculate the barrier height, we determine the maximum W at $\phi = 0$,

$$H(W_{\max}, 0; 0) = \frac{\omega_s^2 \eta}{2\beta_s^2 E_s} W_{\max}^2 - \frac{Ze \omega_s V_{bb} \tau_{pulse}}{2\pi} = 0 \quad (2.22)$$

This gives

$$W_{\max}^2 = \frac{\beta_s^2 E_s Z e \omega_s V_{bb} \tau_{pulse}}{\omega_s^2 \eta 2\pi} \quad (2.23)$$

or, in terms of $\left(\frac{\Delta p}{p}\right)$, where

$$\frac{\Delta p}{p} = \frac{\Delta E}{\beta_s^2 E_s} \quad (2.24)$$

we obtain

$$\left(\frac{\Delta p}{p}\right)_{\max} = \sqrt{\frac{ZeV_{bb}\tau_{pulse}\omega_s}{\beta_s^2 E_s \eta \pi}} \quad (2.25)$$

The barrier bucket height is thus proportional to the square root of the product of the barrier voltage and its pulse length in the induction synchrotron.

2.3 Synchrotron motion in the induction synchrotron

In order to calculate exactly the synchrotron frequency in the induction synchrotron, we start with a trapezoidal profile (more realistic with finite rise and fall times) of the barrier voltages V_{bb} , as depicted in Fig. 21(a). In Fig. 21(b), the outer edges on the phase axis represent the oscillation amplitude of the particle. The motion in the barrier bucket is quantitatively divided into three regions: (1) drift in the null voltage region, (2) focusing in the parabolic potential, and (3) focusing in the linear potential. It should be noted that the motion in region (2) and (3) is subjected to adiabatic damping, as well as that the exact solution throughout the region is known for the abovementioned short time period.

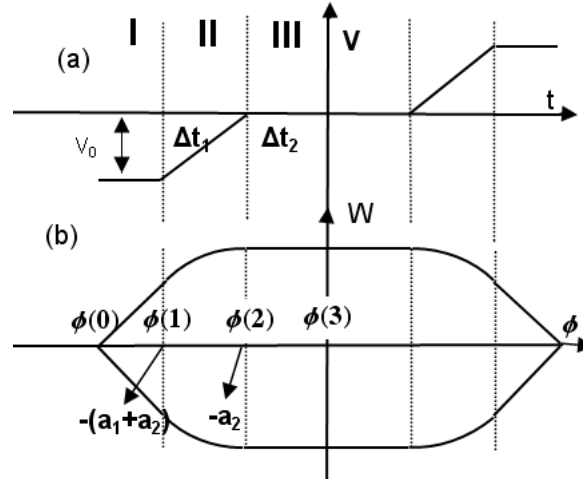


Fig. 21. (a) Barrier voltage shape with three distinct regions encountered by the particles (b) A schematic diagram of the Hamiltonian contour in phase space (W, ϕ).

In order to analyze the temporal evolution of this oscillation amplitude associated with the acceleration, we start from the canonical Eqs. (2.17) and (2.18). Differentiating Eq. (2.18) with respect to time and substituting Eq. (2.17) into the result, we obtain the second-order differential equation,

$$\frac{d^2\phi}{dt^2} - \frac{(dA/dt)}{A(t)} \frac{d\phi}{dt} + \frac{ZeV_{bb}(\phi)A(t)}{2\pi} = 0 \quad (2.26)$$

where the abbreviation, $A(t) = h|\eta|\omega_s^2/\beta_s^2 E_s$ is used. The temporal change in the phases of individual particles is governed by Eq. (2.26). Since the parameters in this equation include all the information associated with the acceleration, its solution can provide the motion in phase space throughout the acceleration period. In order to eliminate the damping term, a new variable, $u(t) = \phi(t)/v(t)$ is introduced. When $v(t) = \sqrt{A(t)}$, Eq. (2.26) reduces to

$$\frac{d^2u}{dt^2} + \left\{ \frac{d^2A/dt^2}{2A(t)} - \frac{3}{4} \frac{(dA/dt)^2}{A^2(t)} \right\} u(t) + B(t) = 0 \quad (2.27)$$

where $B(t) = ZeV_{bb}(\phi)\sqrt{A(t)}/2\pi$. Since $A(t)$ is a slowly varying function of time, its first-order and second-order derivatives with respect to time are small. Accordingly, the second term in the left-hand side of Eq. (2.27) can be ignored in the following derivation. We arrive at a final form of the phase oscillation equation which must be solved,

$$\frac{d^2u}{dt^2} = -B(t) \quad (2.28)$$

The restoring force $B(t)$ can be assumed to be constant during a single synchrotron oscillation period T , which is much shorter than $(dA/dt)/A$. In addition, the synchrotron oscillation is symmetric in phase space, as depicted in Fig. 21 (b). If we obtain the exact solutions in regions I, II, and III as shown in Fig. 21 (a), the synchrotron frequency $\Omega_s = 2\pi/T$ can be written in an analytic form. The instantaneous amplitude of the phase, $\langle\phi\rangle$ is written using the WKB approximation as

$$\langle\phi\rangle = C \frac{\sqrt{A}}{\sqrt{\Omega_s}} \quad (2.29)$$

where, C is a constant coefficient determined from the initial conditions.

Analytical solution for a trapezoidal barrier

Since all parameters are assumed to be constant throughout a single synchrotron oscillation period, the solution of Eq. (2.28) can be written analytically. In region I, it is written as

$$u_I(t) = \frac{1}{2}|B(t)|t^2 + c_1 = \frac{ZeV_0\sqrt{A(t)}}{4\pi}t^2 + c_1 \quad (2.30)$$

where c_1 is calculated from the initial condition, and V_0 is the amplitude of the barrier voltage pulse. In region II, Eq. (2.28) is described by

$$\frac{d^2u_{II}}{dt^2} = -A(t) \cdot k \cdot \left(u_{II} + \frac{a_2}{v} \right) \quad (2.31)$$

Introducing $k = ZeV_0/2\pi a_1$, where $a_1 = \omega_s \Delta t_1$ and Δt_1 is the length of linear region of the barrier voltage, we obtain $a_2 = \omega_s \Delta t_2$. The solution of Eq. (2.31) is well known, and is written as

$$u_{II}(t) = \frac{c_2}{v} \sin \left\{ \sqrt{kA(t)} (t - t_1) + \delta \right\} - \frac{a_2}{v} \quad (2.32)$$

where c_2 , δ and t_1 are constants which are determined from appropriate boundary conditions. Using these analytical solutions, the respective time periods of the motions in regions I and II are evaluated as

$$t_1 = \sqrt{\frac{4\pi \{ \langle \phi \rangle - (a_1 + a_2) \}}{ZeV_0A(t)}} \quad (2.33)$$

$$t_2 = t_1 + \frac{1}{\sqrt{kA(t)}} \sin^{-1} \left(\frac{a_1}{c_2} \right) \quad (2.34)$$

In region III, which is a drift region, the time period is straightforwardly written as $a_2/c_2 \sqrt{kA(t)}$, where $a_2 = \omega_s \Delta t_2$ and Δt_2 is the drift length of the barrier voltage pulse. Thus, the time period to complete one quarter of an oscillation cycle, which is denoted with t_3 , is given by

$$t_3 = \sqrt{\frac{4\pi \{ \langle \phi \rangle - (a_1 + a_2) \}}{ZeV_0A(t)}} + \frac{1}{\sqrt{kA(t)}} \sin^{-1} \left(\frac{a_1}{c_2} \right) + \frac{a_2}{c_2 \sqrt{kA(t)}} \quad (2.35)$$

The synchrotron oscillation period $T = 2\pi/\Omega_s = 4t_3$ leads to

$$\Omega_s = \frac{\pi}{2t_3} \quad (2.36)$$

Here, we note that the synchrotron frequency depends on both the rise time and the drift length of the barrier voltage pulse. We can use these parameters to control the bunch length as desired.

Analytical solution when the bunch edge lies within the linear region

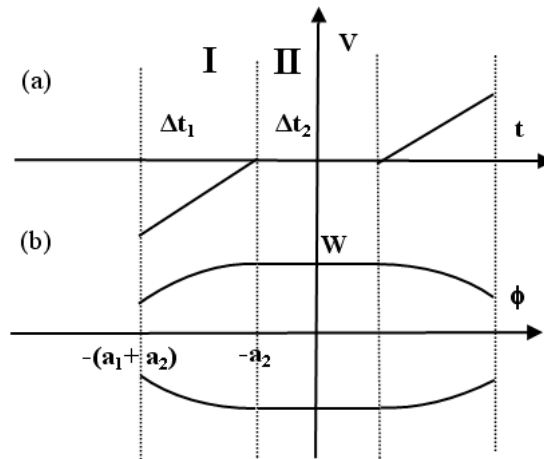


Fig. 22.(a) A schematic diagram of the rise-and-fall shape of the barrier pulse. (b) A Hamiltonian contour in phase space (W , ϕ).

When the bunch edge is in the linear region, i.e., $\langle \tau \rangle < (\Delta t_1 + \Delta t_2)$, as shown in Fig. 22, the respective solutions for $u(t)$ in regions I and II are given by

$$u_I(t) = \frac{c_1}{v} \sin \left\{ \left(\sqrt{kA(t)} \right) t + \delta \right\} - \frac{a_2}{v} \quad (2.37)$$

$$u_{II}(t) = m(t - t_1) + u_I(t_1) \quad (2.38)$$

where c_1 , δ , m and t_1 are constants determined from the boundary conditions. The total time for the motion of a particle in regions I and II is given by

$$t_2 = \frac{1}{\sqrt{kA(t)}} \left\{ \frac{\pi}{2} + \frac{a_2}{(\langle \phi \rangle - a_2)} \right\} \quad (2.39)$$

The time period of the synchrotron oscillation in this case is $T = 2\pi/\Omega_s = 4t_2$.

$$\Omega_s = \frac{\pi}{2t_2} \quad (2.40)$$

Hence, in the linear region the synchrotron frequency is a function of the drift length of the barrier voltage pulse. The part of the bunch which falls in the constant and linear focusing region is subjected to adiabatic damping. The barrier conditions $V_{bb}, \Delta t_1$ and Δt_2 are determined from the chosen operation conditions, and the parameters ω_s, β_s, E_s and η are uniquely determined once the accelerator has been designed.

If the barrier profile is maintained constant, a particle whose oscillation amplitude initially extends to the flat barrier region (I) will fall into the linear barrier region (II) as a result of the adiabatic damping. Beyond the boundary between the linear and quadratic potentials, the analytical form for the synchrotron oscillation changes in the regions where $\langle \tau \rangle > (\Delta t_1 + \Delta t_2)$ and $\langle \tau \rangle < (\Delta t_1 + \Delta t_2)$, respectively. The two solutions should be connected at $\langle \tau \rangle = (\Delta t_1 + \Delta t_2)$.

The present result has been obtained under the assumption of a trapezoidal profile of the barrier voltage. It is straightforward to determine the temporal evolution of the oscillation amplitude $\langle \tau \rangle$ for more extreme profiles, such as a rectangular profile ($\Delta t_1 = 0$). For a rectangular profile, we obtain

$$\langle \tau \rangle^2 = C^2 \sqrt{\frac{8\eta}{\omega_s \pi Z e V_{bb} \beta_s^2 E_s}} \left\{ \sqrt{2(\langle \tau \rangle - \Delta t_2)} + \frac{\Delta t_2}{\sqrt{2(\langle \tau \rangle - \Delta t_2)}} \right\} \quad (2.41)$$

This form suggests a particular feature of the adiabatic damping in the induction synchrotron which can be distinguished from that in an RF synchrotron. The solution of Eq. (2.41) is always written in terms of $\langle \tau \rangle = g(t, \Delta t_2) + \Delta t_2$, where $g(t, \Delta t_2)$ is a slowly varying function of t which is subjected to adiabatic damping and gradually becomes small. Since the isolated offset term of Δt_2 is controllable, the oscillation amplitude can be strictly controlled throughout the acceleration, as expected.

The analytical results were confirmed by verifying the bunch length variation data obtained during the proof-of-principle experiment of the induction synchrotron. The results were verified using computer simulations [16]. The software was then used to carry out KEK-DA simulations, as discussed in Chapter 5.

2.4 Comparison of the synchrotron motions in RF and induction synchrotrons

The equation of motion of the phase of the particles in the case of RF is written as

$$\frac{d^2(\Delta\phi)}{dt^2} = \frac{\eta h \omega_s^2}{\beta_s^2 E_s} \frac{ZeV}{2\pi} (\cos\phi - \cos\phi_s + (\phi - \phi_s) \sin\phi_s) \quad (2.42)$$

Eq. (2.42) is non-linear, and its analytical solution is difficult to obtain. However, if a small phase oscillation amplitude approximation is carried out near the center of the phase space shown in Fig. 23, where the variation in $\Delta p/p$ is almost constant, then the synchrotron frequency can be written analytically. The equation of motion can be reduced to a linear form over a small region of the RF voltage where $\sin\phi \approx \phi$. The small-amplitude synchrotron frequency is given by Eq. (2.14). For a stationary bucket with $\phi_s = 0$, we can write the synchrotron frequency as

$$f_{synchrotron} = \frac{1}{T_s} \sqrt{-\frac{ZehV\eta}{2\pi\beta_s^2 E_s}} \quad (2.43)$$

The synchrotron frequency for protons using KEK-PS parameters at injection is 5.383 kHz. The parameters are tabulated in Table 4. The synchrotron tune, which is defined as

$$\nu = \frac{f_{synchrotron}}{f_{revolution}} = \sqrt{\frac{ZheV|\eta|}{2\pi\beta_s^2 E_s}} \quad (2.44)$$

is calculated to be $8.015 \cdot 10^{-3}$.

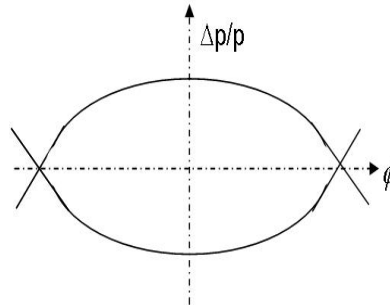


Fig. 23. A schematic diagram of the stationary bucket in RF acceleration

If a large oscillation amplitude is considered, i.e. for large $\Delta p/p$, then the synchrotron frequency is given by

$$f_{RFsynch} = \frac{\pi\nu}{2T_s} \frac{1}{K(x)} \quad (2.45)$$

where $K(x) = \int_0^{\pi/2} \frac{dw}{\sqrt{1-x^2 \sin^2 w}}$ is complete elliptical integral of the first kind, $x = \frac{h\eta}{2\nu} \delta$, and $\delta = \frac{\Delta p}{p}$. The fluctuation of the synchrotron tune is plotted as a function of $\Delta p/p$ in Fig. 25.

Table 4. Parameters for the calculation of the synchrotron frequency of protons.

RF Parameter	Value
Injection energy (MeV)	500
Slippage factor, η_s	-0.4027
Harmonic number, h	9
Revolution period, T_s (μ sec)	1.489
RF voltage, V (kV)	92
Induction parameter	
Barrier pulse separation, Δt (nsec)	60
Barrier voltage, V_{bb} (kV)	10.8

Synchrotron frequency in the case of IS is derived using the canonical equations (2.17) and (2.18). The motion of the particles in the barrier bucket consists of drift in zero-voltage regions between barrier pulses and the motion in barrier pulse regions shown in Fig. 24. The time taken by the particles in each region is calculated as follows.

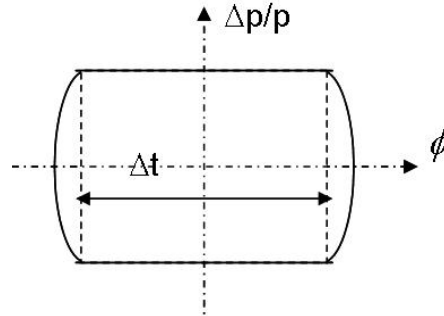


Fig. 24. A schematic diagram of the stationary bucket in an induction synchrotron

The period in the drift region is calculated directly using Eq. (2.18) as

$$\frac{d\phi}{dt} = \frac{\eta h \omega_s^2}{\beta_s^2 E_s} W \Rightarrow \tau_d = 2 \frac{\Delta t / \omega_s}{\eta h \omega_s^2 W / \beta_s^2 E_s} \quad (2.46)$$

where Δt is the distance between different barrier pulses. Using Eq. (2.24), the time in the drift region can be written as

$$\tau_d = 2 \frac{\Delta t}{|\eta| \left(\frac{\Delta p}{p} \right)} \quad (2.47)$$

Similarly the motion in the linear region is obtained by differentiating Eq. (2.18) as

$$\frac{d^2\phi}{dt^2} = \frac{\eta h \omega_s^2}{\beta_s^2 E_s} \frac{dW}{dt} \quad (2.48)$$

If $V(\phi') = V_{ac} - V_{bb}$, then Eq. (2.17) becomes

$$\frac{dW}{dt} = -\frac{ZeV_{bb}}{2\pi} \quad (2.49)$$

Substituting Eq. (2.49) into Eq. (2.48), we obtain

$$\frac{d^2\phi}{dt^2} = -\frac{\eta h \omega_s^2}{\beta_s^2 E_s} \frac{ZeV_{bb}}{2\pi} = C \quad (2.50)$$

Integrating Eq. (2.50), we obtain

$$\phi(t) = \frac{1}{2} Ct^2 + \dot{\phi}(0)t = t\left(\frac{1}{2} Ct + \dot{\phi}(0)\right) \quad (2.51)$$

The time taken in the drift region is written as

$$\frac{\tau_b}{2} = -\frac{2\dot{\phi}(0)}{C} \quad (2.52)$$

This gives τ_b as

$$\tau_b = 4T_0 \left(\frac{\beta_s^2 E_s}{ZeV_{bb}} \right) \left(\frac{\Delta p}{p} \right) \quad (2.53)$$

The synchrotron period is written as

$$T_{synchrotron} = \tau_d + \tau_b = \frac{2\Delta t}{|\eta|(\Delta p/p)} + 4T_s \beta_s^2 \left(\frac{E_s}{ZeV_{bb}} \right) \left(\frac{\Delta p}{p} \right) \quad (2.54)$$

In addition, the synchrotron frequency can be written as

$$f_{synchrotron} = \frac{1}{\frac{2\Delta t}{|\eta|(\Delta p/p)} + 4T_s \beta_s^2 \left(\frac{E_s}{ZeV_{bb}} \right) \left(\frac{\Delta p}{p} \right)} \quad (2.55)$$

The synchrotron tune as a function of $\Delta p/p$ for protons in RF and induction synchrotrons is plotted in Fig. 25. The synchrotron motion behaviour is different in each case for very small and very large $\Delta p/p$. For the case of RF, at very small amplitudes the synchrotron tune is the same as that of the small oscillation amplitude. It decreases monotonically as $\Delta p/p$ increases, and the synchrotron tune decreases rapidly near the separatrix. On the other hand, in the case of IS, for very small amplitudes the synchrotron motion is almost zero. It increases with $\Delta p/p$ and reaches a maximum value, after which it decreases for higher $\Delta p/p$. Therefore, in induction synchrotrons there is no single synchrotron frequency. This feature helps in reducing coherent instabilities in a relatively simple manner as compared to RF synchrotrons.

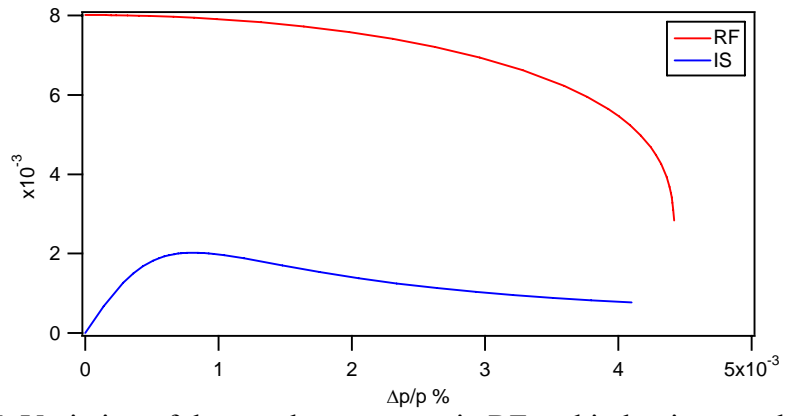


Fig. 25. Variation of the synchrotron tune in RF and induction synchrotrons.

2.4 Transverse motion

Perturbed betatron motion

The orbit of a circulating particle is closed at 2π due to the bending force exerted by the bending magnetic fields. The process of focusing the particles in transverse direction is performed by quadrupole and dipole magnetic fields. The motion of such particles in transverse direction is governed by a second-order differential equation known as the betatron oscillation equation

$$x'' + K(s)x = f(s) \quad (2.42)$$

where $K(s) = \frac{dB/dx}{B\rho}$ is the quadrupole strength which is written as the periodic

function $K(s+C) = K(s)$. A quadrupole with positive strength in one plane is intrinsically negative in the other plane with the same magnitude. Thus, quadrupoles are usually arranged in the so-called FODO pattern where F stands for focusing, D stands for defocusing, and O indicates the drift space. Thus, it provides focusing in both planes. The perturbing term $f(s)$ is usually due to a momentum error and field errors. The former is written as $\frac{1}{\rho} \frac{\Delta p}{p}$, where $\rho(s)$ is the bending radius, which is a

function of the orbit coordinate “ s ”, and $\Delta p/p$ is the excursion from the ideal momentum. The latter is given by $-\frac{\Delta B(s)}{B\rho}$ [17]. The specific (periodic) solution of Eq. (2.42) is written as

$$x(s) = \frac{\sqrt{\beta(s)}}{2 \sin(\mu/2)} \int_s^{s+C} f(s') \sqrt{\beta(s')} \cos \left[\frac{\mu}{2} - |\Psi(s) - \Psi(s')| \right] ds' \quad (2.43)$$

where

$$\mu(s) = \Psi(C) = \int_0^C \frac{ds'}{\beta(s')} = 2\pi Q \quad (2.44)$$

Q is referred to as the betatron tune and $\beta(s)$ is the beta function.

The particles in a bunch usually have a finite momentum spread. This momentum error gives rise to a change in the deflection angle as compared to a particle with the designed momentum. The momentum error deforms the equilibrium beam orbit which is traced out by a particle with the design momentum. For a normalized momentum error of $\Delta p/p=1$, we define a dispersion function $D(s)$ which is a specific solution of Eq. (2.42), i.e. $D(s+C)=D(s)$. Thus, the equilibrium orbit of an arbitrary particle with a momentum error of $\Delta p/p$ is written as

$$x_{eq}(s) = D(s) \frac{\Delta p}{p} \quad (2.45)$$

If the momentum of the bunch center is shifted from the ideal momentum by $\Delta p/p$, the bunch monitor will induce an electric signal proportional to $\Delta R = D(s) \Delta p/p$, where s is the position of the bunch monitor. This signal will become important later on in the discussion regarding the correction of the momentum error.

The magnets in the accelerator ring are not perfect, and the same is valid for their alignment. Error fields produced as a result of imperfections also deform the ideal orbit. Dipole errors caused by magnet imperfections and misalignments induce the closed orbit distortion (COD), which is written by using the specific solution of Eq. (2.45). In most cases, COD is corrected to a certain extent by a correction system employing steering magnets.

When the above two terms are taken into account, then the solution of the perturbed betatron equation is given by a superposition of both terms as follows

$$x(s) = x_{cod}(s) + D(s) \frac{\Delta p}{p} \quad (2.46)$$

Chapter 3 KEK Digital Accelerator

The KEK digital accelerator is based on the 500 MeV booster synchrotron of the KEK proton synchrotron. Argon ions are planned to be accelerated in the proof-of-principle experiment. Necessary modifications in the booster ring are currently under progress.

3.1 KEK-PS booster synchrotron

The KEK-PS booster synchrotron is a rapid-cycle synchrotron (RCS). The magnetic field varies sinusoidally at a repetition rate of 20 Hz. A schematic description of the KEK-PS booster synchrotron is shown in Fig. 26 along with a photograph of the facility in Fig. 27. The KEK-PS booster synchrotron was used as a dedicated injector for the 12 GeV KEK-proton synchrotron between 1974 to 2006. It is capable of accelerating proton beams converted from H^- beams of 40 MeV to 500 MeV. The booster lattice is formed of 8 combined function magnets. The machine parameters are given in Table 4. In addition, the dispersion function is plotted in Fig. 28 for $1/8^{\text{th}}$ of the ring circumference, and its beta functions are given in Fig. 29. The maximum value of the dispersion function, which is almost flat in the straight section, is 1.4 m. Two RF cavities were used to provide the acceleration voltage.

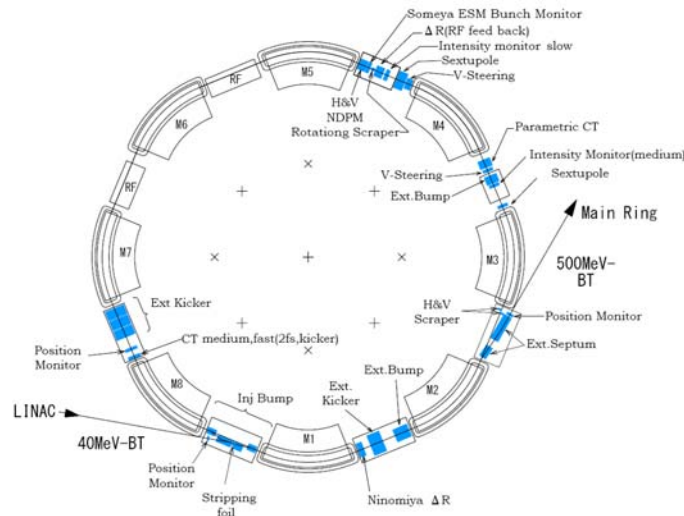


Fig. 26. A schematic diagram of the KEK-PS booster synchrotron.



Fig. 27. Picture of the KEK-PS booster synchrotron.

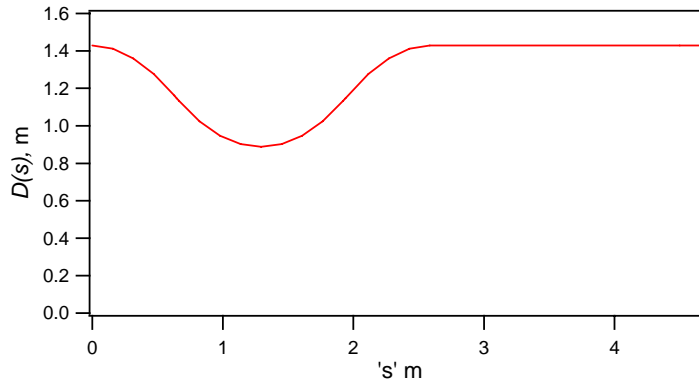


Fig. 28. Dispersion function plot of the KEK-PS booster synchrotron.

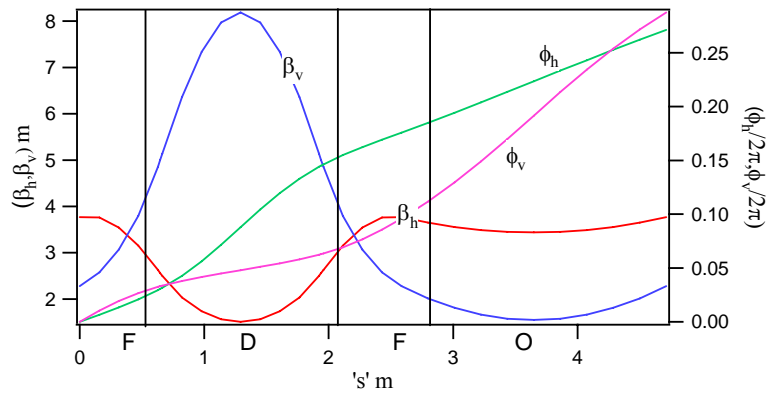


Fig. 29. Plot of the beta functions and the phase advance of $1/8^{\text{th}}$ of the KEK-PS booster synchrotron.

Table 4. Machine and lattice parameters of the KEK-PS booster synchrotron

Machine parameters		Value
Bending radius, ρ	(m)	3.3
Circumference, C_0	(m)	37.71
Magnetic flux density, B_{min}	(T)	0.27
Magnetic flux density, B_{max}	(T)	1.1
Injection energy	(MeV)	40
Extraction energy	(MeV)	500
Frequency	(Hz)	20
Transition gamma, γ_t		2.3
Lattice parameters		Value
Super-periodicity		8
Lattice		FDFO
Combined function triplet bending angle, θ		$\pi/4$
Arc length, $\rho\theta$	(m)	2.5918
Drift length, $2l$	(m)	2.1206
Period length, $\rho\theta+2l$	(m)	4.7124
Tune, Q_x/Q_y		2.17/2.32
$ n $ - value of F/D		12.091

3.2 The KEK-PS booster as a digital accelerator

In a small RF synchrotron, the RF frequency corresponds to the revolution frequency of the accelerated bunch since $h=1$, and it must be varied with time for the purpose of synchronizing it with the acceleration. However, the dynamic range of radio frequency devices, such as RF cavities and RF sources, is limited to an order of magnitude. Accordingly, it is not realistic to accelerate particles from extremely low energies to relativistic energies in the same RF synchrotron. Therefore, RF synchrotrons require injector systems in order to guarantee a certain revolution frequency from the very beginning. On the other hand, the switching power supply energizing the induction cell, which is triggered by the gate control signal created from the bunch monitor signal, can provide a pulse voltage at an arbitrary frequency. Therefore, even a very low-energy particle requiring a switching frequency of the order of kHz can be accelerated in a DA, which effectively frees the digital accelerator from the need to use injectors [18]. Only an ion source is required to provide ions. An ECR ion source, which is currently under development, will provide argon ions for the proof-of-principle experiment [19]. The ion source will be embedded into the 200kV high voltage terminal, and the ions will be ejected with an initial kinetic energy of $Z \times 200 \text{keV}$, after which they will be injected into the KEK - DA through a low-energy beam transport line. A schematic diagram is shown in Fig. 30, and its parameters are given in Table 6. Some modifications need to be implemented in the existing accelerator setup in order to turn it into a digital accelerator [20].

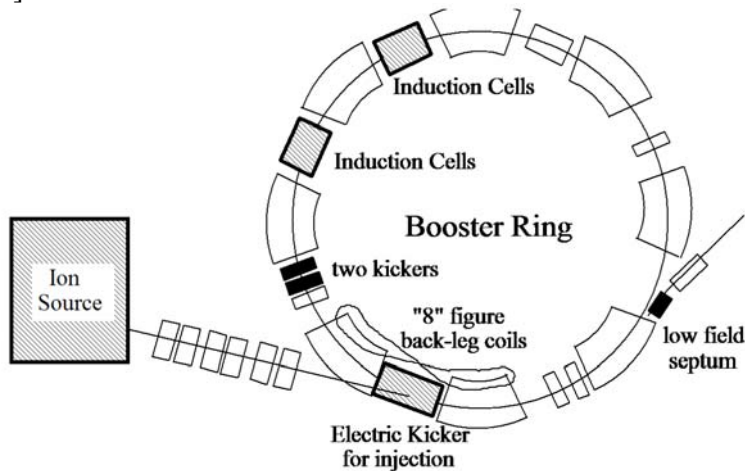


Fig. 30. A schematic diagram of the KEK-digital accelerator

Table 6. The KEK-DA parameters

Machine Parameters	Value
Maximum acceleration voltage (kV)	2.4
Injection voltage (kV)	200
Magnetic flux density, B_{min} (T)	0.02916
Magnetic flux density, B_{max} (T)	0.6429
Frequency of magnet ramping, f (Hz)	10

The change of magnetic flux density, $B(t)$ in the booster ring is given by

$$B(t) = \left(\frac{B_{\max} + B_{\min}}{2} \right) - \left(\frac{B_{\max} - B_{\min}}{2} \right) \cos \omega t \quad (3.1)$$

where B_{\max} and B_{\min} represent the maximum and minimum magnetic flux density, respectively, and ω is the angular frequency of the magnet ramping. The designed acceleration voltage V_{ac} is written as

$$V_{ac} = \rho C_0 \frac{dB(t)}{dt} \quad (3.2)$$

The acceleration voltage always changes over the ramping period and has a maximum value in the middle of the acceleration period. The peak acceleration voltage for the booster ring is 2.4 kV for the 10 Hz operation frequency. For a fully stripped argon ion, the revolution frequency changes from ~ 100 kHz to greater than 2 MHz during the acceleration, as shown in Fig. 31. Both the required voltage and the revolution frequency exceed the present performance limit of the induction cell and the switching power supply. Therefore, a new acceleration scheme using superposition, dynamic sorting, and intermittent operation, as described in Chapter 4, is under development [21].

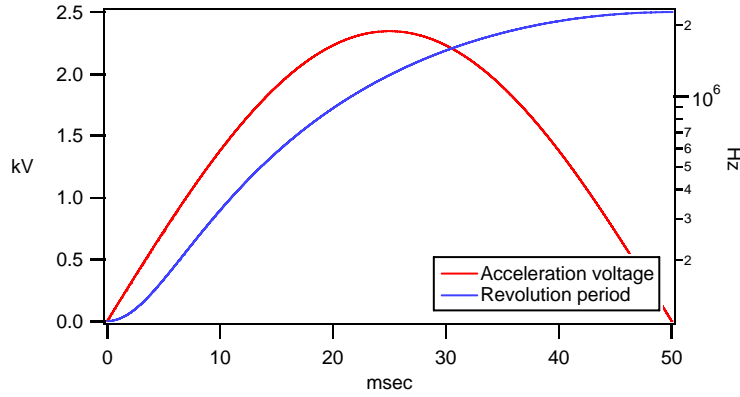


Fig. 31. Plot of the designed acceleration voltage and revolution period for the KEK-DA at 10 Hz operation for a fully stripped argon ion.

There are other issues regarding the dynamics of the beam due to the extremely low injection energy. Electron capture by the injected heavy ions or stripping as a result of collision with residual gas molecules is an important issue. The cross-section of these processes depends strongly on the relativistic beta of the particles, and hence the requirement for vacuum of the order of 10^{-7} Pa in the vacuum chamber for the survival of 90% of the particles. Also, the remnant magnetic fields and fields induced by eddy current on the vacuum metal chamber gives rise to closed-orbit distortion [22].

3.3 Required modifications for acceleration

It is necessary to implement certain modifications in the present 500 MeV booster ring in order to be able to accelerate argon ions for the proof-of-principle experiment. An ECR ion source, which is under development, will be connected to the booster via a low-energy beam transport line. Furthermore, the injection and extraction kickers are also modified for the injection and extraction of the bunch, and the RF cavities will be replaced with induction cells. The resonant power supply of the main magnets of the booster will be modified to ramp at a frequency of 10 Hz. The requirement of very high vacuum $\sim 10^{-7}$ Pa in the KEK-DA entails the modification of the bump magnets, which are located inside vacuum tanks, where the magnets must be placed outside the vacuum chamber. Also, the evacuation of the vacuum chamber with high-capacity pumps is inevitable. Remnant fields of magnitude ~ 0.0005 T in the main magnets become an issue at low injection flux density of ~ 0.02 - 0.03 T. Thus, remnant fields are reduced by 8-shaped back-leg coils which wind around two poles of adjacent main magnets in order to cancel the induced voltage associated with the excitation shown in Fig. 32. Also, a very low current and very wideband beam monitors are required for a low-intensity ion beam. The relevant details have been discussed in [20].

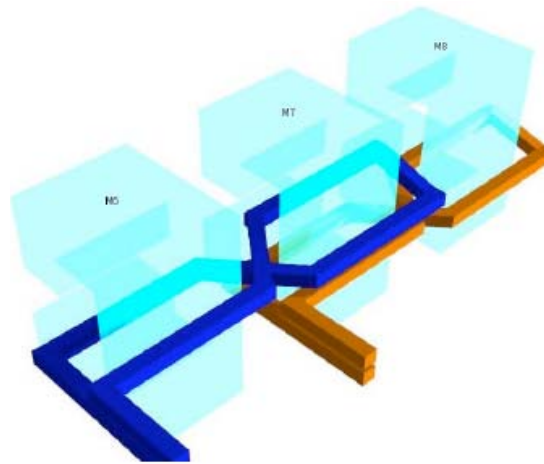


Fig. 32. A schematic diagram of the 8-shaped back-leg coil

Chapter 4 Digital Acceleration scheme

In a rapid-cycle synchrotron, the accelerating voltage must change in order to satisfy the acceleration condition $V_{ac} = \rho C_0 dB/dt$. The acceleration voltage in DA is not variable due to the nature of the induction cell. Its output voltage is always the same as the voltage of the switching power supply or that of the DC power supply, which is not varied for short time periods of the magnitude of milliseconds. Fixed voltage is applied to the circulating particles throughout the entire acceleration time period if the switching power supply is triggered at every turn. This will immediately violate the acceleration condition. In order to ensure the desired acceleration, a technique referred to as pulse density control, which was proposed in the previous experiment, has been extensively developed for the present KEK-DA. Its details are discussed below.

4.1 Pulse density control

The pulse density control is a unique feature of the induction synchrotron. It is also known as pulse density modulation in the digital domain. Pulse density modulation is used for audio signals for a variety of applications in cell phones and audio CD's. In our application, the acceleration voltage needs to be varied to provide optimum energy for the particles to follow the ramping of the magnet. The required energy gain ΔE during a short time period from t to $t+\Delta t$ is written as

$$\Delta E = \int_t^{t+\Delta t} Ze \cdot V_{ac}(t) \cdot f(t) dt \quad (4.1)$$

where V_{ac} is the design acceleration voltage and $f(t)$ is the revolution frequency. Assuming a constant acceleration voltage V_0 , we can determine the modified pulse density from

$$g(t) = \frac{\Delta E}{V_0 \Delta t} \quad (4.2)$$

Here, $g(t)$, which is a function of time, can be referred to as switching frequency of the induction acceleration system. As schematically shown in Fig. 33, the pulse density gradually increases just after the injection. If the switching frequency or the pulse density is controlled in the entire acceleration region, the desired acceleration should be secured [18].

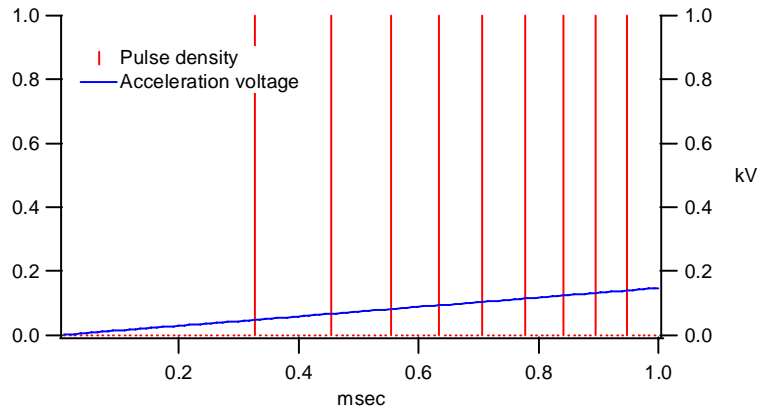


Fig. 33. A schematic representation of the pulse density control

4.2 Staging

In the KEK-PS booster, which is an RCS, there is a requirement for the acceleration voltage to change continuously between 0 V and 2.4 kV. Also, the revolution frequency of argon ions changes from ~ 100 kHz at injection to greater than 2 MHz near the extraction in the case of the acceleration shown in Fig. 31. Therefore, the pulse width of the acceleration voltage needs to be varied as a function of the revolution frequency.

In order to accommodate the requirement of a long pulse length and a large acceleration voltage with the existing induction acceleration system, which is characterized by a short pulse width and a fixed voltage, the acceleration period has been divided into four stages. In each stage, the induction cells are used in different configuration depending on the acceleration voltage and the pulse width. Since the bunch length is ~ 4 μ sec at the beginning, a long acceleration voltage pulse is required. This stage is called Stage I. In Stage II, a higher acceleration voltage is required in order to meet the acceleration voltage requirement. The revolution frequency exceeds 1 MHz in Stage III, requiring the intermittent operation and dynamic sorting of the induction cells. In Stage IV, the revolution frequency becomes greater than 2 MHz.

A chopped ion bunch (shown in red in Fig. 34) with a duration of 4 μ sec is assumed as an injected bunch from the ECR ion source. The bunch is confined by two barrier voltage pulses with opposite polarity (shown in pink and blue) and a long rectangular pulse for acceleration (shown in black). A negative polarity pulse resetting the magnetic core is used to protect it from saturating.

In Stage I, a long acceleration voltage pulse with a duration of 4 μ sec is required to properly accelerate the ions in the bunch. This long acceleration pulse with positive polarity can be generated by sequentially triggering two induction acceleration cells with the same output voltage and pulse length [23]. For the sake of convenience, the cells are labeled as ID#1 and ID#2. As indicated in Fig. 34, the reset voltage pulse is also generated in the same turn. Furthermore, the confinement voltage pulses are generated at both sides of the bunch, and two different induction cells are used for generating barrier pulses. The amplitude of cell ID#1 & ID#2 is assumed to be 0.8 kV, with maximum flat top pulse width of 2 μ sec.

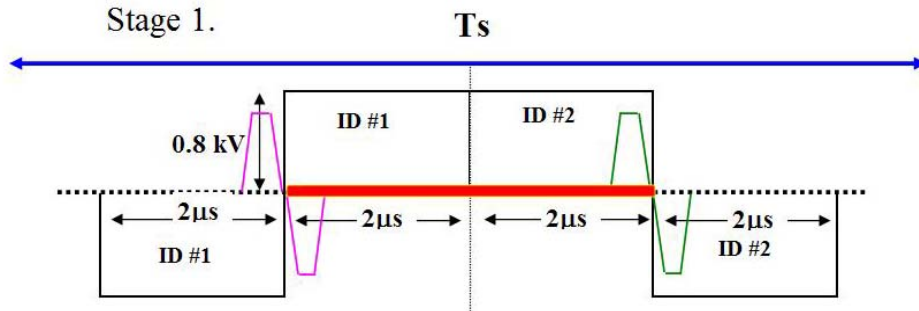


Fig. 34. A schematic diagram of the acceleration and confinement voltage pulse profile in Stage I. The confinement voltage pulses are given in pink and green, the acceleration voltage pulse in black, and the bunch in red.

In Stage II, the acceleration voltage requirement exceeds 0.8 kV, and therefore cells ID#1, ID#2, and ID#3 is triggered simultaneously in order to generate a superimposed voltage of 2.4 kV, as shown in Fig. 35. This stage lasts until the revolution period becomes $\sim 1 \mu\text{sec}$. At the end of this stage, the revolution frequency of the bunch becomes greater than 1 MHz, and the limit of the switching power supply is reached.

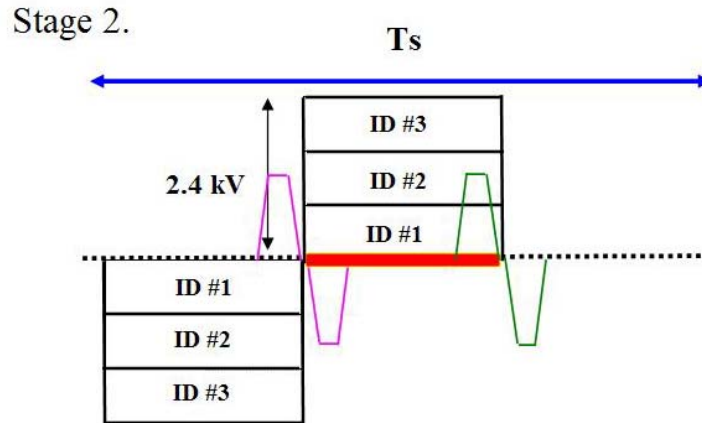


Fig. 35. A schematic diagram of the acceleration and confinement voltage pulse profile in Stage II. The confinement voltage pulses are given in pink and green, the acceleration voltage pulse in black, and the bunch in red.

4.3 Intermittent operation and sorting

In Stage III, the particle revolution frequency becomes greater than 1 MHz, and therefore two additional induction acceleration cells are required in the subsequent turn shown in Fig. 36. The new cells are identified as ID#4 & ID#5. Therefore, ID#1 and ID#4 are triggered in combination with ID#2 and ID#5 in subsequent turns in order to meet the designed acceleration voltage requirement. In this stage, a single cell is used for generating a confinement voltage pulse, with the bunch located at its center. In the subsequent turn, another induction cell is triggered, generating another confinement voltage pulse. Thus, intermittent operation of the induction acceleration cells starts from this stage onwards. Also, sorting of the induction cells is required in this stage for the purpose of choosing the correct pair.

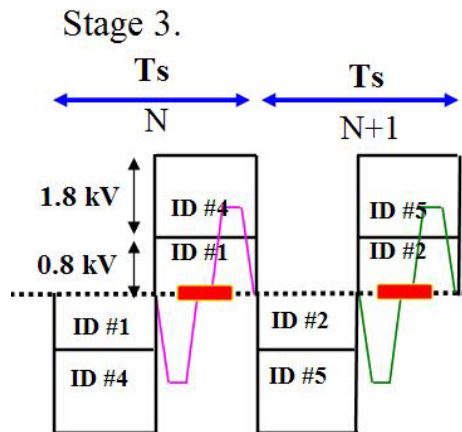


Fig. 36. A schematic diagram of the acceleration and confinement voltage pulse profile in Stage III. The confinement voltage pulses are given in pink and green, the acceleration voltage pulse in black, and the bunch in red.

Finally, in Stage IV, the particle revolution frequency becomes greater than 2 MHz, and therefore another pair of induction acceleration cells is required since the cells triggered in the previous two turns cannot be triggered in the subsequent turns shown in Fig. 37. Thus, each cell has a dead time of the order of 2 turns to recover and generate an acceleration voltage when triggered.

Stage 4.

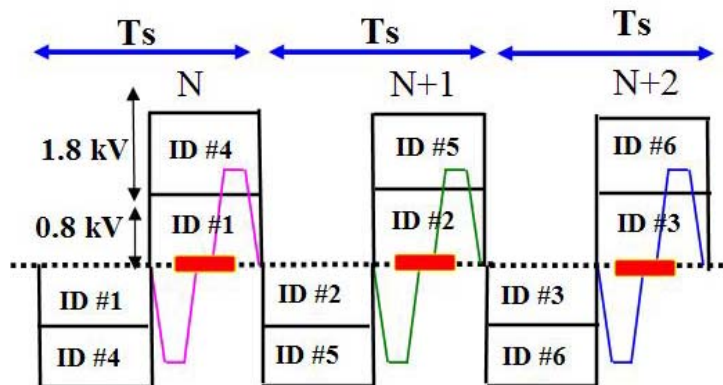


Fig. 37. A schematic diagram of the acceleration and confinement voltage pulse profile in Stage IV. The confinement voltage pulses are given in pink, green, and blue, and the acceleration voltage pulse in black, and the bunch in red.

In the entire acceleration period, the acceleration voltage provided by the induction cell is shown in Fig. 38. In the present scheme, the generation of a reliable trigger becomes pertinent. For example, in the sequential operation in Stage I, mistripping can result in a sharp dip or rise in voltage in the middle of the acceleration voltage, causing serious issues with the beam dynamics. In Stage III and IV, the switching power supplies must be prevented from triggering pulses greater than 1 MHz. Therefore, the intermittent trigger should not at any point exceed this limit.

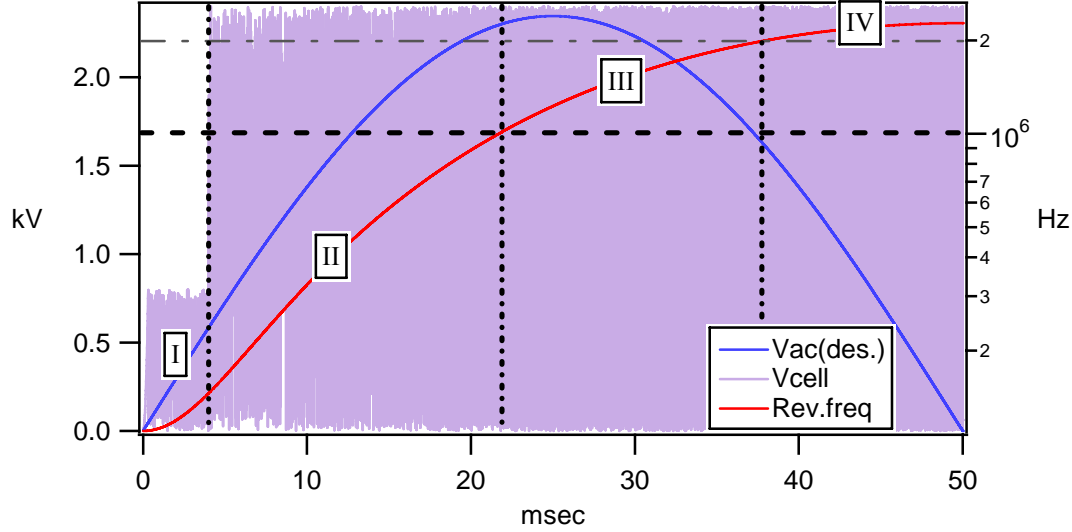


Fig. 38. The designed acceleration voltage is shown in blue, revolution period is shown in red and the acceleration voltage provided by the induction cell throughout the acceleration period is shown in purple.

Chapter 5 Simulations

The particle tracking software used in this work is based on a the code developed earlier for the purpose of studying the longitudinal dynamics in the proof-of-principle experiment of the induction synchrotron concept, which was written in the C language [24]. The software essentially tracks individual particles indicated by the ' j ' superscript by using Eq. (2.15) for the changes in particle energy, depending on the acceleration voltage and the barrier voltage, and Eq. (2.16) is used for calculating the changes in phase of the individual particles in each turn:

$$(\Delta E)_{n+1}^j = (\Delta E)_n^j + Ze \{ V(\phi_n^j) - V_{ac} \} \quad (5.1)$$

$$(\Delta \phi)_{n+1}^j = (\Delta \phi)_n^j + \frac{2\pi\eta}{\beta_{n+1}^s E_{n+1}^s} (E_{n+1}^j - E_{n+1}^s) \quad (5.2)$$

where, $j=1 \dots N$

The adiabatic damping of the bunch length was confirmed by comparing the simulation results with the experimental results and the analytical results [16]. The software was then modified to include the KEK-DA parameters. Certain new functions necessary for the KEK-DA have been implemented as listed below.

Following are the notable changes included in the software:

1. *Modification of the acceleration pattern* - specific to the KEK-DA rapid-cycle synchrotron
2. *Staging acceleration scheme* - The acceleration scheme as described in the preceding section is included into the software.

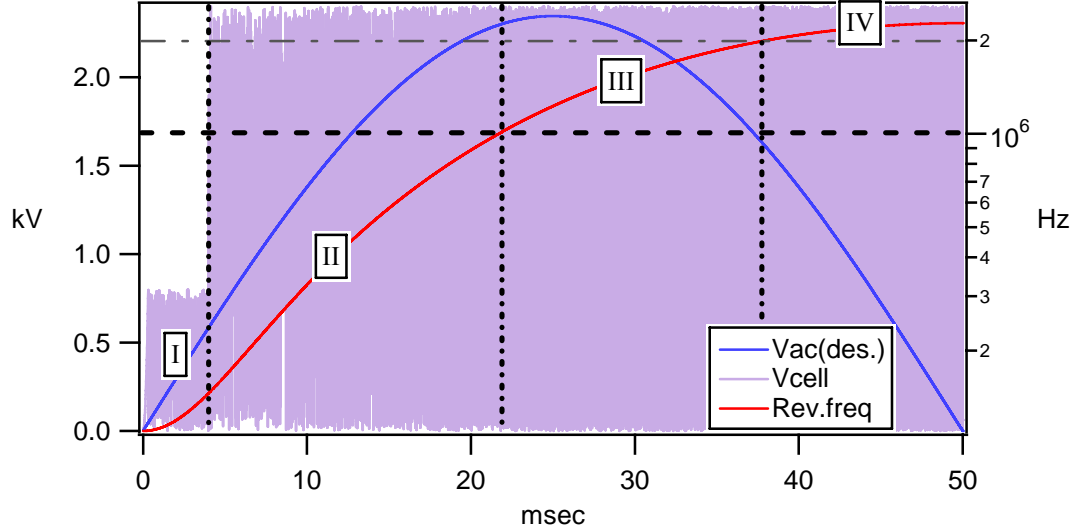


Fig. 38. The designed acceleration voltage is shown in blue, revolution period is shown in red and the acceleration voltage provided by the induction cell throughout the acceleration period is shown in purple.

Chapter 5 Simulations

The particle tracking software used in this work is based on a the code developed earlier for the purpose of studying the longitudinal dynamics in the proof-of-principle experiment of the induction synchrotron concept, which was written in the C language [24]. The software essentially tracks individual particles indicated by the ' j ' superscript by using Eq. (2.15) for the changes in particle energy, depending on the acceleration voltage and the barrier voltage, and Eq. (2.16) is used for calculating the changes in phase of the individual particles in each turn:

$$(\Delta E)_{n+1}^j = (\Delta E)_n^j + Ze \{ V(\phi_n^j) - V_{ac} \} \quad (5.1)$$

$$(\Delta \phi)_{n+1}^j = (\Delta \phi)_n^j + \frac{2\pi\eta}{\beta_{n+1}^s E_{n+1}^s} (E_{n+1}^j - E_{n+1}^s) \quad (5.2)$$

where, $j=1 \dots N$

The adiabatic damping of the bunch length was confirmed by comparing the simulation results with the experimental results and the analytical results [16]. The software was then modified to include the KEK-DA parameters. Certain new functions necessary for the KEK-DA have been implemented as listed below.

Following are the notable changes included in the software:

1. *Modification of the acceleration pattern* - specific to the KEK-DA rapid-cycle synchrotron
2. *Staging acceleration scheme* - The acceleration scheme as described in the preceding section is included into the software.

3. *Barrier voltage optimization* - The required barrier voltage is optimized for the software and was verified with the analytical value of the barrier height provided by the barrier voltage.
4. *Pulse density control* - Pulse density control is an important feature of the digital acceleration scheme, as described in Section 4.1.
5. *Barrier voltage generation based on the bunch signal data of the preceding turn* - The induction acceleration system generates gate trigger signals depending on the circulating bunch signal. Therefore, in subsequent turns, depending on the bunch signal from the preceding turn, barrier voltages and acceleration voltages are produced exactly in time. This feedback is taken into consideration in the simulations.
6. *Jitter of the barrier voltage pulse with respect to time* - Barrier voltages are produced after processing the bunch monitor signal data in the DSP. As DSP is a clock-based system, the DSP clock has an inherent clock jitter with respect to time, which amounts to a maximum of 8 nsec. The effect of the jitter on the survival rate is studied using the software.
7. *Realistic acceleration voltage profile* - The shape of the acceleration voltage profile as obtained from the existing induction cell deviates from the ideal trapezoidal voltage profile, and the reflection voltage is superposed onto the flat top part. These perturbations are included into the software.

For the KEK-DA simulations, an initial chopped beam of 4 μsec with a maximum momentum spread of $\pm 0.4\%$ is given as an input file. The input file is generated on the basis of the parameters set in the software for argon ions. The number of particles N in the bunch, the initial kinetic energy of the argon ions, the barrier voltage amplitude, and the width and position of the pulse are specified. The maximum momentum spread $(\Delta p/p)_{max}$ of the initial chopped beam and its maximum width dt_{max} are also set in the software. The program then randomly creates initially set particles with the appropriate momentum and position using a random number generator within the specified limits. The initial distribution thus obtained is shown in Fig. 39.

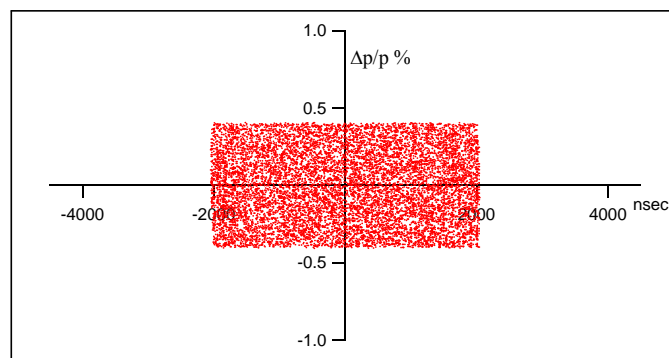


Fig. 39. Initial distribution of the argon ions for the simulations

Table 7. KEK-DA simulation parameters

Parameter	Value
Argon atomic mass	40
Argon atomic charge	+18
Width of the injected bunch	4 μsec
Momentum aperture	$\pm 1\%$

$\Delta p/p$ of the injected bunch	$\pm 0.4\%$
No. of acceleration cells	6
No. of confinement cells	3
Number of particles tracked	10000

The software performs particle tracking by following the discrete Eqs. (5.1) and (5.2) taking into consideration the acceleration and barrier voltage profiles at each turn. The machine and simulation parameters are given in Tables 6 and 7, respectively. The barrier voltage is required for confining the particles in the induction synchrotron. It should provide an optimum bucket size to accommodate the maximum number of particles. In the acceleration scheme described in Chapter 4, in Stage I and Stage II, two independent induction cells (1 turn configuration) are used to provide barrier voltage, while from Stage III onwards a single induction cell is used to provide barrier voltage, where the bunch is placed at the center as shown in Fig. 36. The set and reset pulse of the barrier voltage at the end of the acceleration period should be accommodated in a single turn. Therefore, it sets a limit on the maximum pulse width of the barrier voltage. Also, due to hardware limitations, the barrier voltage amplitude (1.8 kV maximum) cannot be changed in time. Therefore, after a process of trial and error, a barrier voltage pulse of 160 nsec for both set and reset is assumed in the simulations. These parameters of the barrier voltage give a maximum bucket height of 0.98% at the beginning of the acceleration.

The information regarding the phase of the bunch is used to generate the trigger timing for the barrier voltage pulse and the acceleration voltage pulse. The information about the acceleration voltage amplitude in each stage is stored in the program and, depending on the acceleration stage, the appropriate values are chosen. Perturbations from the ideal acceleration voltage profile and jitter in the barrier voltage generation timing are taken into account. The simulation diagram is depicted in Fig. 40.

Trigger timing manipulation

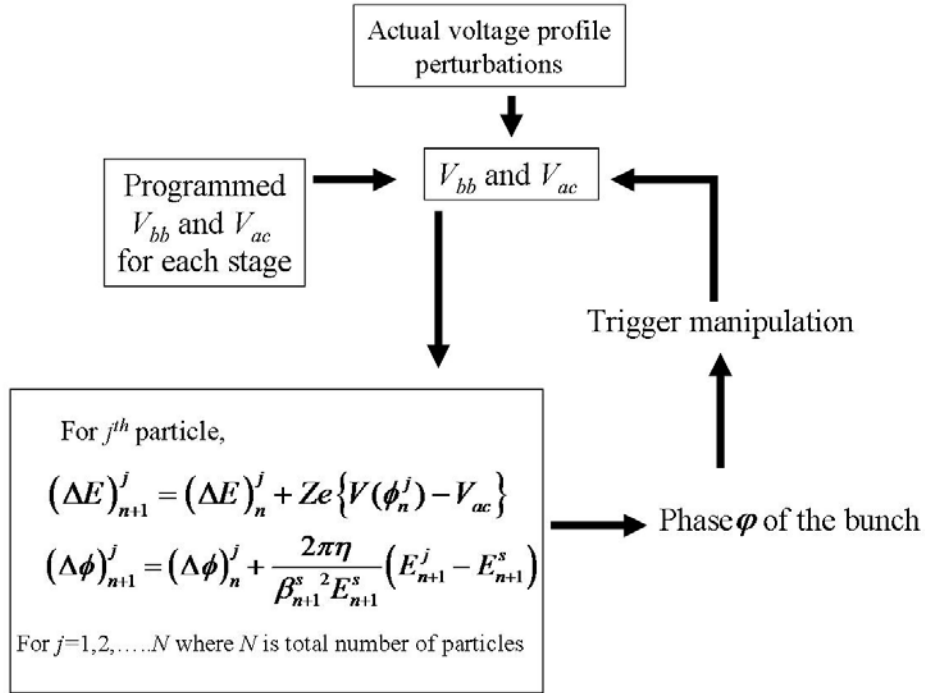


Fig. 40. Simulation diagram

In order to determine the timing to trigger the barrier voltages, it is crucial to know the position of the beginning, the center, and the end of the bunch with respect to time. Let us assume a bunch profile as shown in Fig. 41. The timing t_1 for the profile curve, represented by a solid red line crossing a preset threshold in the vertical direction, is defined as the beginning of the bunch. Next, a number of particles belonging to each fine time bin is integrated over all bins. Then, the timing t_2 for the integrated curve, represented by a blue solid line crossing 50% of the integrated value at the end, is defined as the center of the bunch. Thus, the other edge of the bunch is determined by $t_3=2 \cdot (t_2 - t_1)$. Using the timing information about t_1 and t_3 , the barrier voltages for the next turn are generated in the simulations. In addition, a few other conditions were implemented in the simulation code. The pulse duration between the two barriers should not exceed 4 μsec at the beginning. Also, the second barrier timing is reduced by 10% to hasten the bunch shortening.

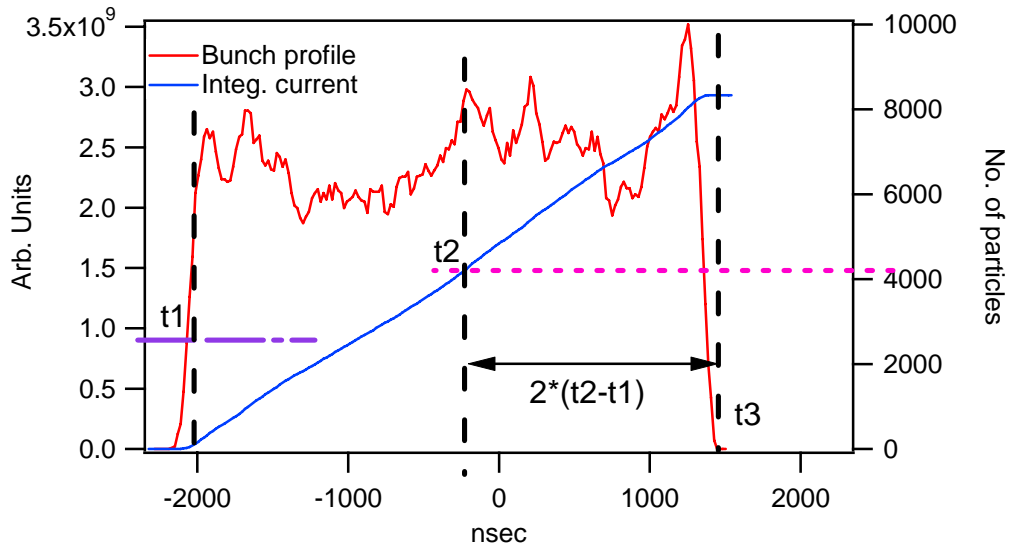


Fig. 41. A schematic diagram of the generation of the trigger timing from the bunch signal. The threshold in the bunch profile is shown in purple, and the threshold in the integrated current is shown in pink. Here 't1' and 't2' represents timing information.

In Stage III, a bunch is placed at the center of the barrier voltage described in 4.3. Therefore, the bunch center timing information is only used for generating the barrier voltage and the acceleration voltage pulse.

Effects of pulse density control

The pulse density is controlled in the simulation by summing the acceleration voltage in each turn decided by the magnet ramping. When the sum exceeds the unit of the fixed induction cell voltage, a single acceleration pulse is generated. Hence, with the increase in acceleration voltage amplitude, the pulses are generated at a faster rate. Figs. 42(a) and (b) show the phase plots just before and after the first acceleration pulse is generated. Furthermore, the maximum $\Delta p/p$ is $\pm 0.65\%$, and the pulse density profile for the first 1 msec is shown in Fig. 43.

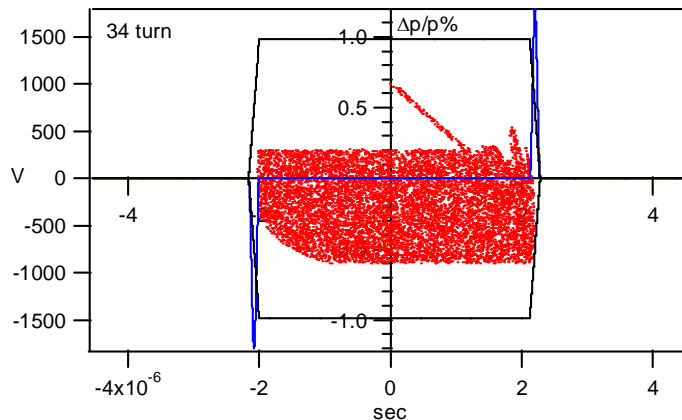


Fig. 42(a) Phase plot before the generation of the first acceleration pulse. The particles are shown in red, and the blue lines shows the confinement voltage pulse.

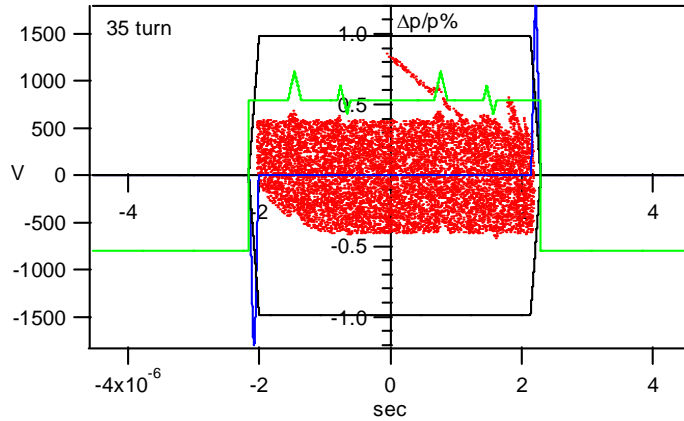


Fig. 42(b) Phase plot after the first acceleration pulse is generated. The particles are shown in red, the blue and green lines shows the confinement voltage pulse and the acceleration voltage, respectively.

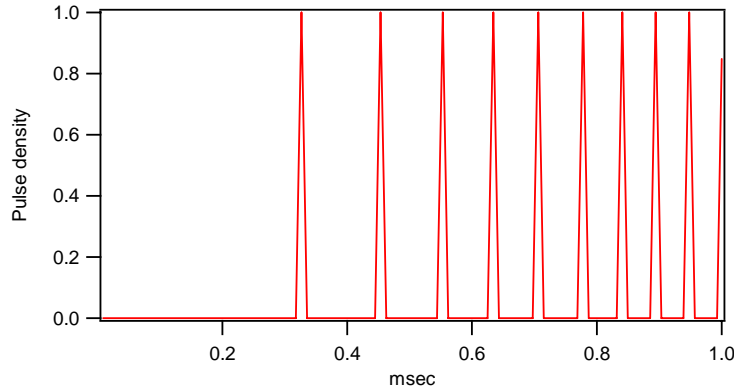


Fig. 43 Pulse density until 1 msec during acceleration

Loss of particles

In the simulations, each particle is tracked with an ID number, viz. `err_ch[n]`. If the momentum error ($\Delta p/p$) $< \pm 1\%$, then it has a value of 1. When ($\Delta p/p$) becomes greater than $\pm 1\%$, then it is set to zero and the count of lost particles is increased by 1, and these particles are not tracked any further.

The phase space plots at different times are shown in Fig. 44. The confinement voltage of 1.8 kV, with a 160 nsec pulse width forms the barrier bucket. It should be noted that the positive pulse for the first barrier voltage and the negative pulse for the second barrier voltage is not shown in these plots. The longitudinal phase space plots shown in Fig. 44 (a), (b), (c), (d), and (e) are at 0 msec, 1.789 msec, 10 msec, 25 msec, and 40.77 msec from the time of injection, respectively. The green waveform denotes the acceleration voltage pulse. The maximum energy gain per nucleon is 40 MeV/au for the given KEK-DA parameters, and the survival of particles is 85%, as shown in Fig. 45. There is some beam loss near the transition from Stage I to Stage II. The longitudinal bunch length near the transition is larger than 2 μ sec, and therefore both ends of the bunch fall outside the barrier in Stage II. This loss can be reduced by moving the barrier pulse quickly but adiabatically in Stage I before the transition occurs.

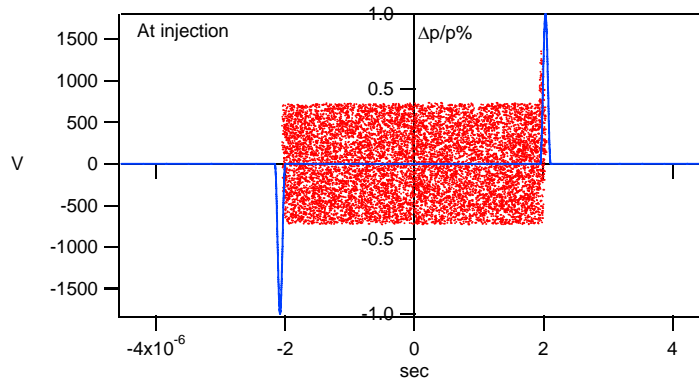


Fig. 44 (a). Longitudinal phase space plot at injection. The particles are shown in red, and the blue and green lines denote the confinement voltage pulse and the acceleration voltage, respectively.

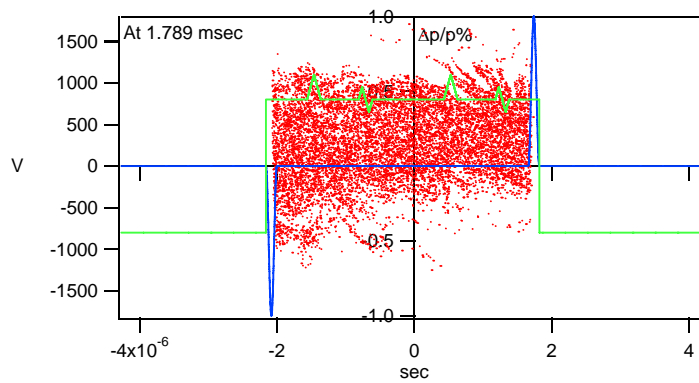


Fig. 44 (b). Longitudinal phase space plot at 1.789 msec. The particles are shown in red, and the blue and green lines denote the confinement voltage pulse and the acceleration voltage, respectively.

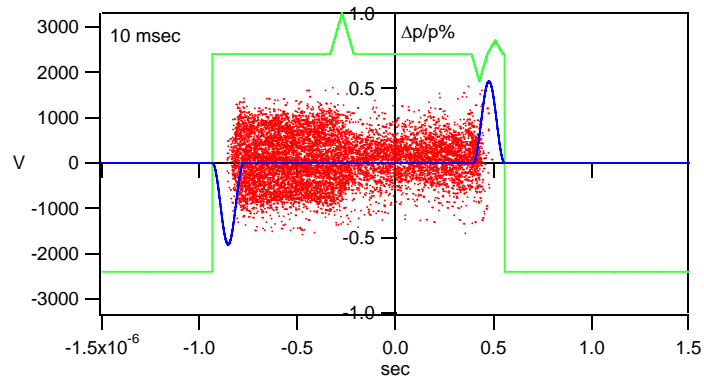


Fig. 44 (c). Longitudinal phase space plot after 10 msec. The particles are shown in red, and the blue and green lines denote the confinement voltage pulse and the acceleration voltage, respectively.

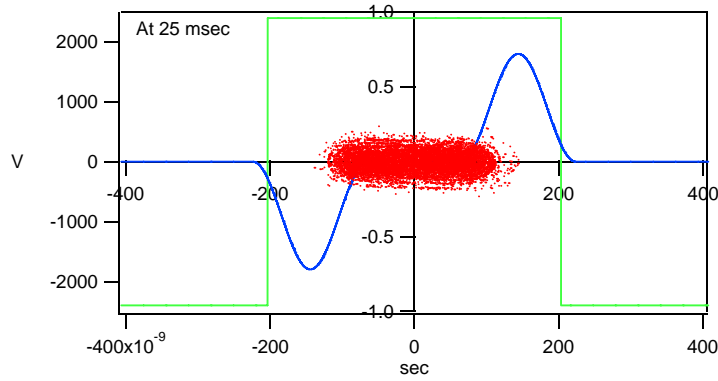


Fig. 44 (d). Longitudinal phase space plot at 25 msec. The particles are shown in red, and the blue and green lines denote the confinement voltage pulse and the acceleration voltage, respectively.

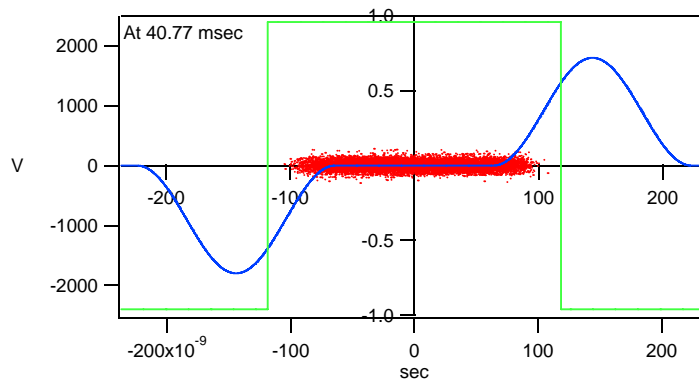


Fig. 44 (e). Longitudinal phase space plot at 40.77 msec. The particles are shown in red, and the blue and green lines denote the confinement voltage pulse and the acceleration voltage, respectively.

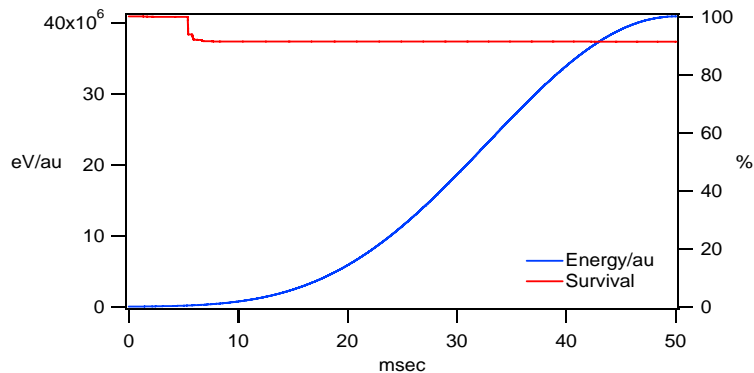


Fig. 45. Survival rate and energy/nucleon ratio for argon ions over the acceleration period

Perturbation

The main sources of perturbation are the reflection voltage superimposed on the acceleration voltage pulse and inherent jitter in the DSP clock pulse. The high voltage measurements of the induction cell indicate the first and the second reflection on the top of the pulse. The first reflection occurs at approximately 650 nsec from the rising edge, and the second reflection occurs at $\sim 1.45 \mu\text{sec}$ at the top of the pulse. This corresponds to the round-trip time of the backward pulse generated at the load edge

through the transmission line. The delay in the transmission line is ~ 5 nsec/m, and the measured length of the transmission cable is roughly ~ 60 m, which yields an estimation of 600 nsec for the round trip. The amplitude of the first and second reflection was 300 V and 150 V, respectively, as shown in Fig. 56. In parallel operation, where three cells are triggered simultaneously, the amplitude of the reflection increases threefold, as shown in Fig. 57. This effect is included in the simulation in the acceleration voltage profile. The reflection voltage on the flat top of the acceleration voltage is acceptable, as verified in the simulations. There is no significant change in the survival of the particles due to the reflection voltage at certain locations on the acceleration voltage. There is a growth in emittance when compared to the case with no reflection in the early acceleration region in Stage I and Stage II. The reflection can be reduced by changing the length of the transmission cable for the KEK-DA operation.

Also, a jitter in time of 8 nsec in the confinement voltage pulse is added to the trigger timing information. The source of the jitter is the clock of DSP, which generates gate trigger signals for the MOS-FETs of the switching power supply. The effects of the jitter are not as prominent in the early acceleration region when the bunch size is of the order of μ sec. When the bunch is placed at the center of the barrier in the Stage III, then the emittance blow-up becomes visible. With a large jitter value, the emittance blow-up affects the survival of particles, as shown in Fig. 46. However, a jitter level of 10-15 nsec appears to be acceptable.

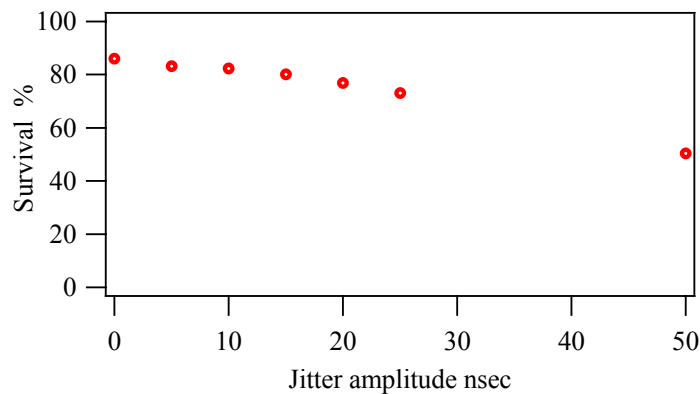


Fig. 46. Jitter amplitude of the confinement voltage pulse V/s survival rate of the argon ions over the acceleration period.

There are some other perturbations associated with the stage transition mentioned in the previous section. In order to ensure a proper transition of state (from low to high or vice versa) in the logic gate of the acceleration control unit, a dead time during the stage transition must be assumed. The time necessary for the state transition to occur in a logic unit is approximately 25 to 30 nsec. However, a few logic units operate in series, and therefore a dead time of the order of several hundred ns is considered to be sufficient. Therefore, a dead time of the order of 10 μ sec is included in the simulations. During this dead time, an acceleration voltage pulse is not generated. The simulation results showed no significant changes in the survival rate caused by the introduction of dead time. If a dead time greater than 20 μ sec is taken during the stage transition, then losses start to occur.

Chapter 6 Necessary devices - a long-pulse induction acceleration cell

In order to capture and accelerate a large number of low-velocity ions, a long pulse induction cell is indispensable due to the long revolution period in the early acceleration stage. Uniformity in the acceleration voltage profile is extremely important. Unfortunately, the output voltage pulse produced by the existing induction cell displays a droop due to the inherent nature of the electric circuit, which is 15% in a 250 nsec pulse. The droop profile in the acceleration voltage plays the role of additional focusing or defocusing in the longitudinal direction, as extensively discussed in [24]. The use of the existing induction cells is not acceptable for the generation of an acceleration voltage pulse of 2 μ sec due to the larger droop. In order to solve this problem, the existing acceleration cell has been modified for the purpose of mitigating the droop.

6.1 The droop

The droop is a phenomenon in which when a pulse voltage is applied to a circuit with a time constant τ , then the voltage across the circuit falls gradually by a value proportional to $\exp(-\tau_p/\tau)$, as shown in Fig. 47. This gradual fall is attributed to overlapping of reflected voltage having an opposite sign (after the reflection from the induction cell), which causes the forward voltage wave to decrease with time.

Pulse response of an electrical circuit

When a pulse voltage of amplitude V with a time constant τ is applied to a circuit, then the output voltage takes the following form

$$v_0 = c_1 + c_2 e^{-\tau_p/\tau} \quad (6.1)$$

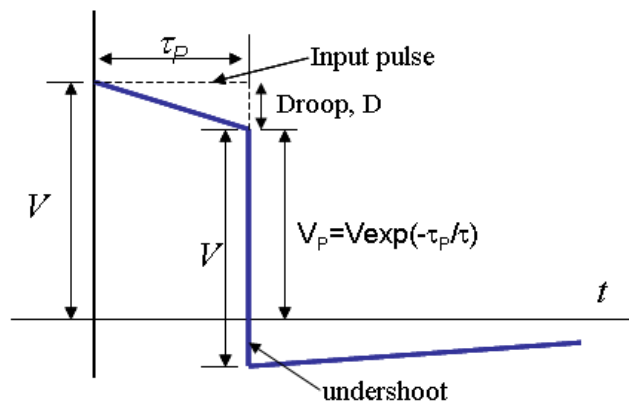


Fig. 47. Pulse voltage response of a circuit with a time constant τ

where τ_p is the pulse width c_1 which corresponds to a steady state value of the output voltage say V_f . Furthermore, c_2 is determined by the initial output voltage V_i , and therefore at time $t=0$ we can write $c_2 = V_i - V_f$. Thus, the general solution becomes

$$v_0 = V_f + (V_i - V_f)e^{-\tau_p/\tau} \quad (6.2)$$

When the initial output voltage is equal to zero, then the output voltage is written as

$$v_0 = V_f(1 - e^{-\tau_p/\tau}) \quad (6.3)$$

The output has a droop and an undershoot in the negative region. The amplitude of the undershoot is equal to $V - V_p$.

A parallel LCR equivalent circuit representation of the induction cell is shown in Fig. 6. The droop D in the rectangular pulse is written as

$$D \propto e^{(-Z_1/L)t} \quad (6.4)$$

where, $1/Z_1 = 1/Z_0 + 1/Z + 1/R$, Z_0 is the characteristic impedance of the transmission line Z is the matching resistance R is due to core loss in the induction cell, and L is the inductance.

6.2 2:1 transformer as a long pulse induction acceleration cell

For the existing 1-turn induction cell, the droop is estimated to be 14% by using the parameters given in Table 1, which is consistent with the measured value. In order to reduce the droop, either Z_1 is reduced or L is increased in Eq. (6.4). In the originally developed induction cell configuration, changing Z_1 is ruled out since it is fixed. Therefore, the only possible way is to increase the core inductance L . In addition, the undershoot in the secondary loop voltage might become a separate issue when the induction cells are operated sequentially.

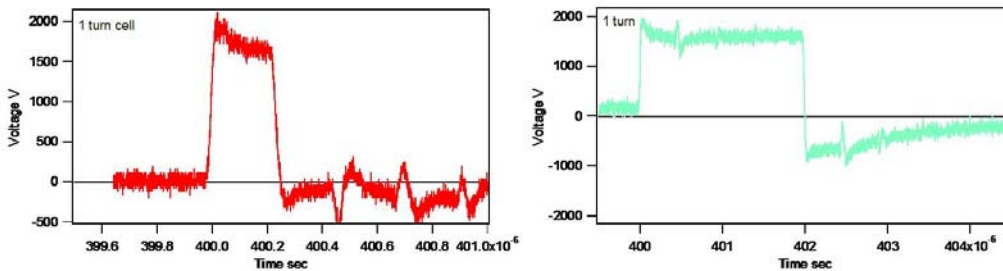


Fig. 48 Droop and undershoot in a 1-turn induction cell

The output waveforms at 250 nsec and 2 μ sec for a high-voltage operation of the 1-turn configuration are given in Fig. 48. In the 2 μ sec pulse excitation, the initial part shows a droop as observed in the 250 nsec pulse excitation and the reflection on the top of the pulse. The latter part of the pulse is almost constant. Also, the undershoot in the output pulse is very large, becoming approximately 800 V. This is not acceptable for serial operation.

Various options exist for the reduction of the droop, e.g., using a magnetic core with a large radius increases the inductance but requires changing the dimensions of the induction cell. An induction cell with a large diameter cannot be accommodated inside the existing space due to the fixed height of the main magnets, thus putting a restriction on the size in radial direction. Also, if the number of Finemet® bobbins is increased, then the inductance increases, although this changes the dimension of the induction cell in longitudinal direction. However, since only the space occupied by the RF cavities is available for the induction cells, there are restrictions in both

horizontal and vertical dimensions which can be accommodated into the booster ring. Therefore, the modification of the induction cell from a 1:1 transformer to a 2:1 transformer configuration is the most practical and economical option available. This modification simply increases the inductance four times due to the N^2 dependence, where N is the number of turns. Therefore, an estimated value of the droop in a 2-turn configuration is 3.4%, where $R = 4R_{1:1}$ and $L = 4L_{1:1}$ is assumed in the calculation ($R_{1:1}, L_{1:1}$ are the 1-turn induction cell values).

The modifications to the 2-turn transformer were carried out by modifying the two circular conductors connected to the feeder lines. Both circular conductors were split into two semi-circular rings, and a copper bar was attached in order to create a 2-turn configuration, as shown in Figs. 49(a) and (b). This modification was implemented while keeping the existing overall dimensions of the induction cell. Three induction cells were modified to 2-turn configuration.

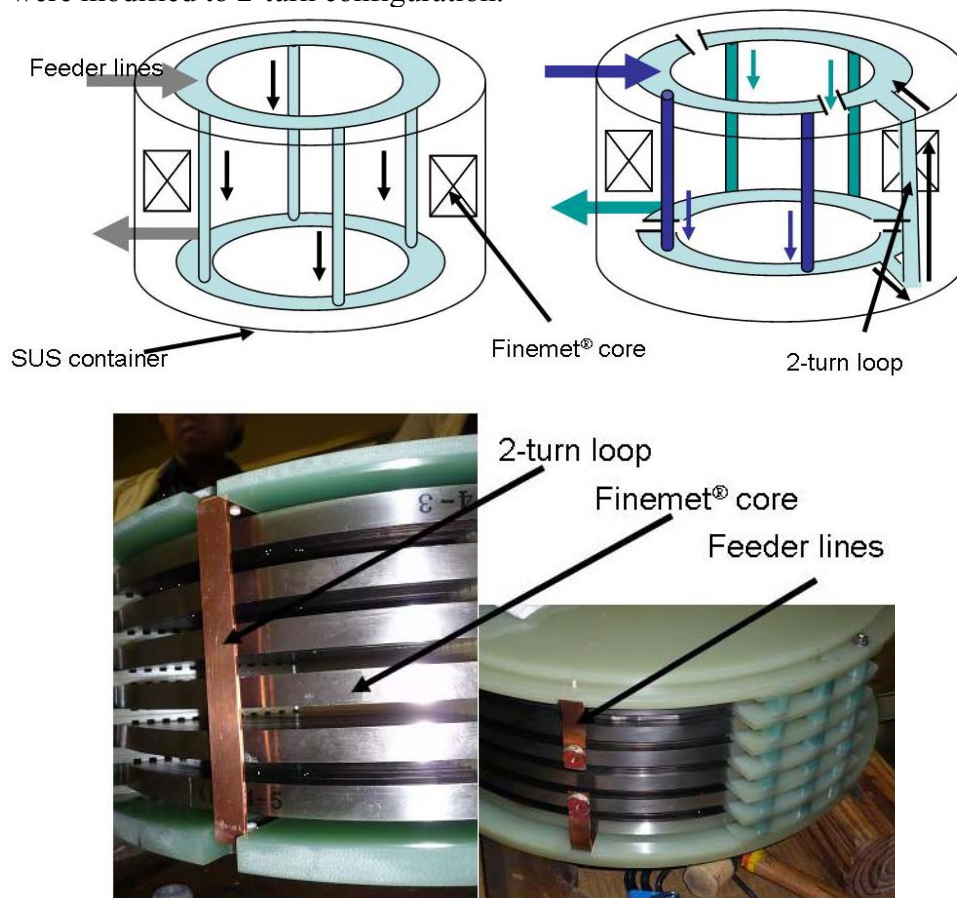


Fig. 49 (a). A schematic diagram of a 1-turn and a 2-turn induction cell. (b). Induction cell with a 2 turn loop, which is implemented by a copper bar.

6.3 Characteristics of 2-turn induction cells

The parameters of the 2-turn modified induction cells are confirmed by impedance measurements. The impedance value is required for achieving maximum transfer efficiency from the matched transmission line impedance, thus reducing the reflection

amplitude. In the case of assuming a parallel L, R equivalent circuit of the magnetic material, the impedance of the magnetic material can be defined as

$$Z = j\omega\mu L_0 \quad (6.5)$$

where $L_0 = \frac{\mu_0 w}{2\pi} \ln\left(\frac{b}{a}\right)$ is the free space inductance, with $\mu = \mu_0 \mu_r$, and $\mu_r = 1$ for free space. Furthermore, “ w ” is the width, “ b ” is the outer radius, and “ a ” is the inner radius of the core, while $\mu_r = \mu' - j\mu''$ is the complex permeability of the magnetic material. Substituting for ‘ μ_r ’ in Eq. (6.5), we obtain

$$Z = j\omega L_0 \mu' + \omega L_0 \mu'' \quad (6.6)$$

In the parallel circuit model,

$$L \frac{di_L}{dt} = Ri_R = V \quad (6.7)$$

where $I = i_L + i_R$ is the total current through the inductor and the resistor. Therefore, assuming a $\exp(j\omega t)$ variation of the current, we can write

$$\frac{1}{Z} = \frac{1}{j\omega L} + \frac{1}{R} \quad (6.8)$$

Substituting the value of Z as obtained in Eq. (6.6), we obtain

$$\frac{\omega L_0 \mu''}{(\omega L_0 \mu'')^2 + (\omega L_0 \mu')^2} - \frac{j\omega L_0 \mu'}{(\omega L_0 \mu'')^2 + (\omega L_0 \mu')^2} = \frac{1}{j\omega L} + \frac{1}{R} \quad (6.9)$$

Comparing the real and imaginary terms, we arrive at

$$L(\omega) = \frac{(\mu'')^2 + (\mu')^2}{\mu'} L_0, \text{ and} \quad (6.10)$$

$$R(\omega) = \frac{(\mu'')^2 + (\mu')^2}{\mu''} \omega L_0 \quad (6.11)$$

The induction cell is represented by a parallel LCR equivalent circuit, as mentioned earlier. The impedance of the circuit is written as

$$Z(\omega) = \frac{1}{\left[\frac{1}{R(\omega)} + j \left(\omega C - \frac{1}{\omega L(\omega)} \right) \right]} \quad (6.12)$$

where $L(\omega)$ and $R(\omega)$ are given by Eq. (6.10) and Eq. (6.11), respectively. Using complex permeability data as supplied by Hitachi metals [25], L and R can be calculated as functions of the frequency. These values are then used to determine the impedance of the induction cell. The value of the capacitance C is chosen to match the measured impedance data. The impedance measurement was performed using a Vector Network Analyzer (VNA). Smith chart measurements with VNA directly yield the real and imaginary parts of the impedance at various frequencies. The parameters of the 2-turn induction cell are given in Table 8.

Table 8. 2-turn cell electrical parameters

Capacitance (pF)	180
Inductance (μ H)	440

Resistance (Ω)	1280
-------------------------	------

The impedance plot after the modification is shown in Fig. 50. After ascertaining all the parameters, the matching resistance value was calculated. The value of the required matching resistance Z_{mat} connected in parallel to the induction cell is $\sim 134 \Omega$.

$$\frac{1}{120} = \frac{1}{Z_{cav}} + \frac{1}{Z_{mat}} \quad (6.8)$$

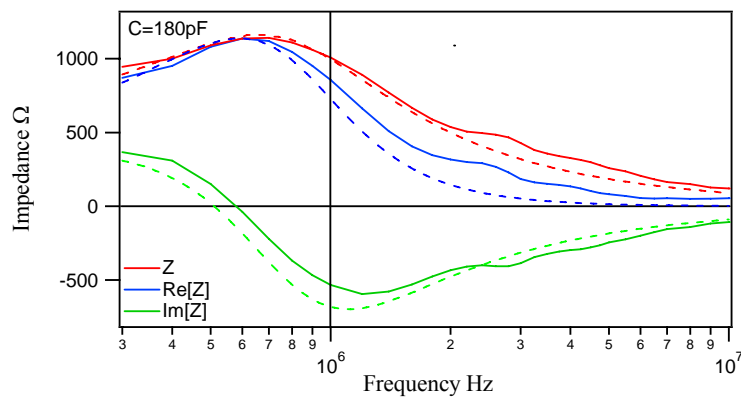


Fig. 50. Impedance measurement plot for a 2-turn cell induction cell (measured using VNA). The measured value is shown by bold lines and the calculated value by dashed lines with a capacitance value of 180 pF.

Since most of the current flows through the matching resistance, a heat run test was carried out in order to check the increase in temperature and the cooling water flow requirements. A flow rate of 15 l/min is found to be sufficient to maintain the temperature below 40°C, as shown in Fig. 51.

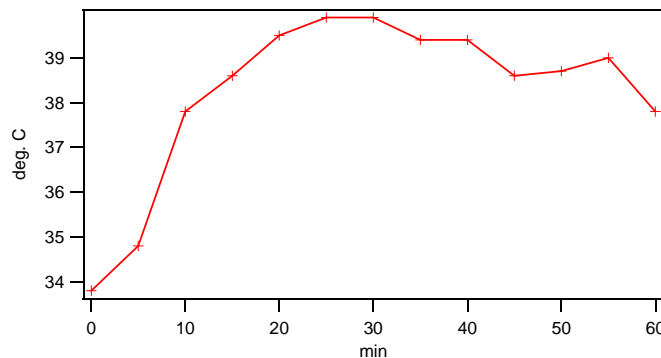


Fig. 51. Temperature of the matching resistance during 1 hour of continuous operation.

6.4 Voltage profile of the modified induction cell

High-voltage measurements were performed in order to verify the parameters as well as to ascertain the reduction in droop in the output voltage profiles of the

modified induction cells. The wire measurement setup is shown in Fig. 52. A wire connects two ends of the induction cells, and the voltage induced across the ceramic gap is measured by a high-voltage probe. Furthermore, the induction cells are insulated from the stand, and the matching resistance is connected in parallel to the induction cell.

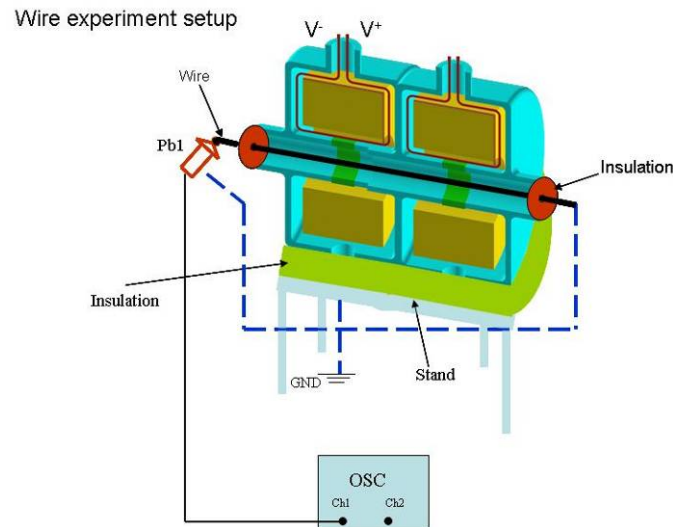


Fig. 52. High-voltage measurement setup.

The waveforms in the modified induction cell indicate an overshoot of ~ 400 V at the beginning of the pulse, a reduced droop and an undershoot, as shown in Fig. 53. The rise time of the pulse is determined by the capacitance of the induction cell. In the modified induction cell, the measured capacitance is smaller, which results in an overshoot in the output voltage. The reflection on the top is prominent, and the first reflection voltage appears at ~ 650 nsec. This corresponds to the round trip delay in the transmission line. The latter part is flat due to the multiple reflections, which overlap with the input pulse. The measured undershoot is within 200 V in the 2-turn configuration, as compared to the 800 V in the 1-turn configuration.

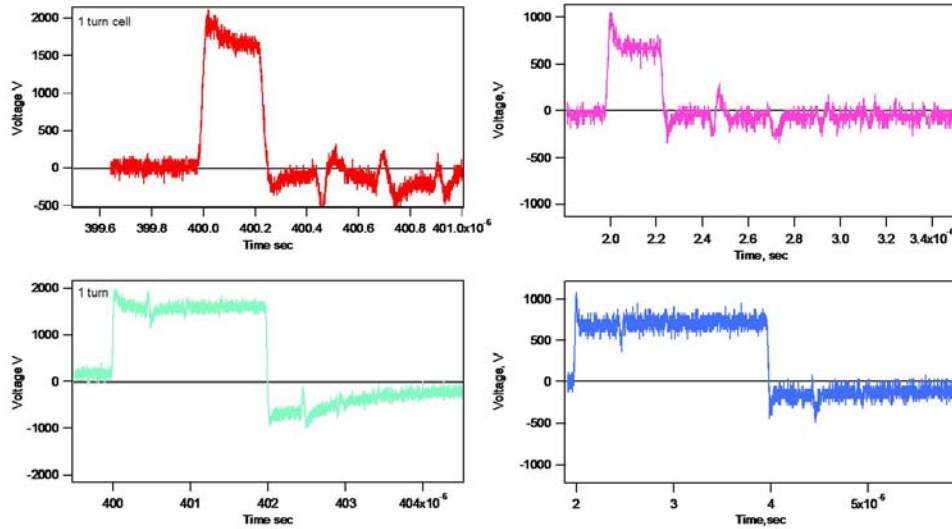


Fig. 53. A comparison of the droop and undershoot plots corresponding to the 1-turn and 2-turn configurations for pulse widths of 250 nsec and 2 μ sec.

The measurement results from the high-voltage tests were verified using the SPICE circuit simulation software. The induction cell parameters as obtained from the impedance measurements are used shown in Fig. 54 (a), and the results of the simulation are shown in Fig. 54 (b). An inductance of 0.9 μ H and a resistance of 10 Ω are included in parallel to the switch in order to simulate the arm of the switching power supply in the SPICE simulation. This was required for simulating the undershoot in the pulse. An inductance of 3 μ H is added in series with the matching resistance in order to obtain proper polarity of the reflection voltage in the pulse. The matching resistance inductance value of \sim 3.6 μ H was later verified by measurements (for 134 Ω resistor chain) with an LCR meter, as shown in Fig. 55.

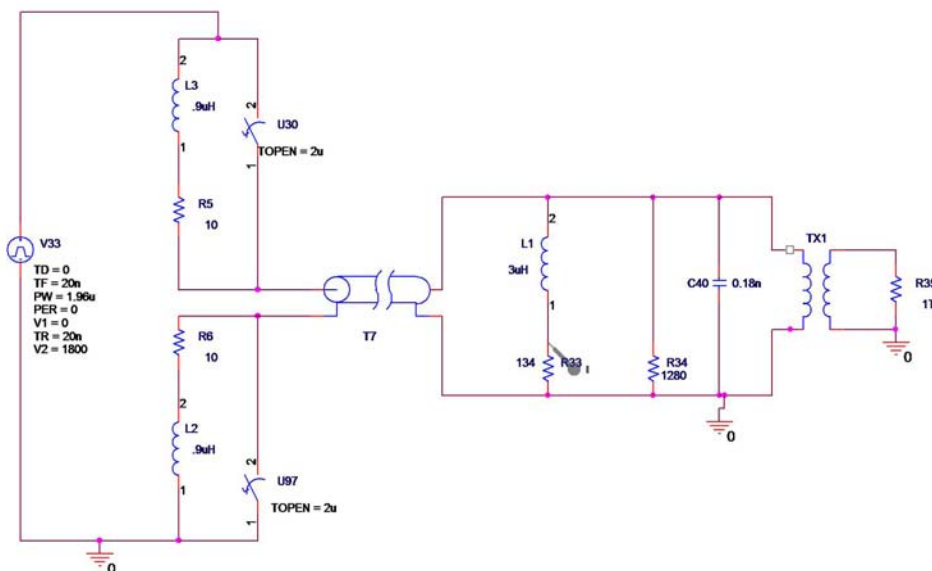


Fig. 54(a) SPICE simulation circuit

The current measured with a CT connected to the matching resistance is compared with the SPICE simulation results.

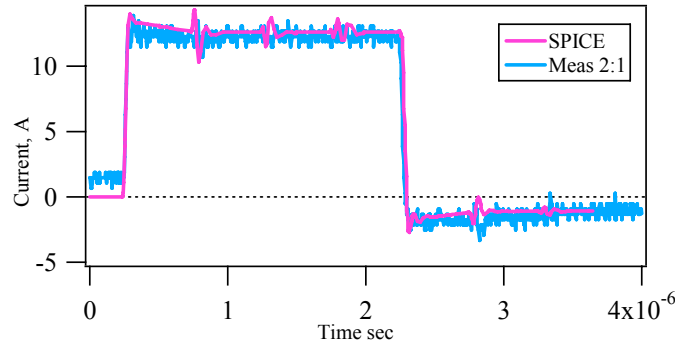


Fig. 54(b). Comparison of the SPICE results and the measurement results corresponding to 2-turn cells

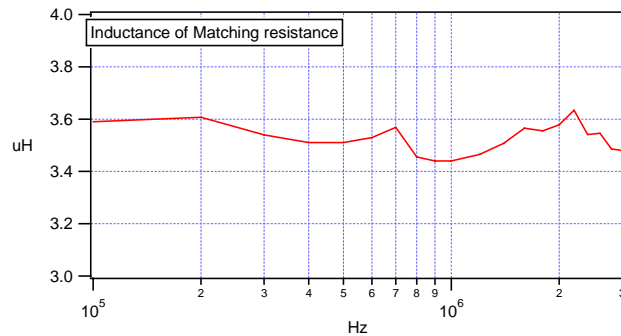


Fig. 55. Matching resistance inductance as measured with an LCR meter

6.4 Sequential and parallel operation of the long-pulse induction cells

As described in Chapter 4, it is necessary to operate the induction cells in both parallel and serial trigger mode. The output voltage in serial mode is shown in Fig. 56. The overshoot mentioned in Section 6.3 is reduced by connecting a 2.2 nF capacitor in parallel to the induction cell. However, the rise time of the induction cell increased to 110 nsec. The voltage induced on the wire stretched between the two ends of the induction cell is measured, and the reflection on the top of the pulse occurs at ~650 nsec, 1.4 μ sec and 2.6 μ sec. A reflection at 650 nsec and 1.4 μ sec exists on the first induction cell output, and a reflection at 2.6 μ sec exists on the second induction cell output. It was observed during the experiment that the trigger timing for the second induction cell needs to be adjusted with a process of trial and error in order to reduce the dips and peaks at the center of the output pulse.

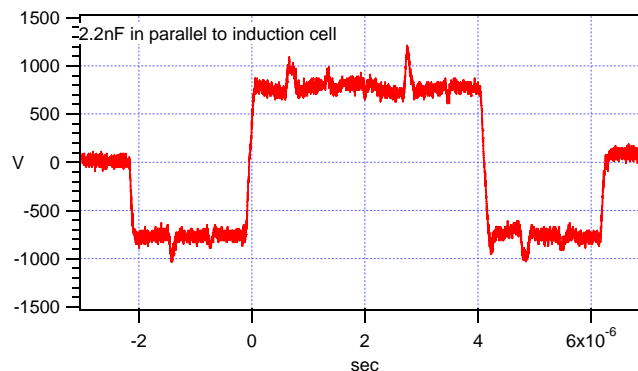


Fig. 56. Output waveform when the serial trigger is applied to two 2-turn induction cells with a 2.2nF capacitor connected in parallel to the feeder lines in order to reduce the overshoot.

The measurement results for the parallel trigger mode are shown in Fig. 57. A simultaneous trigger is applied to three induction cells. As expected, the voltage superposition resulted in a 2.4 kV output from three cells. However, the reflection amplitude also increased proportionally.

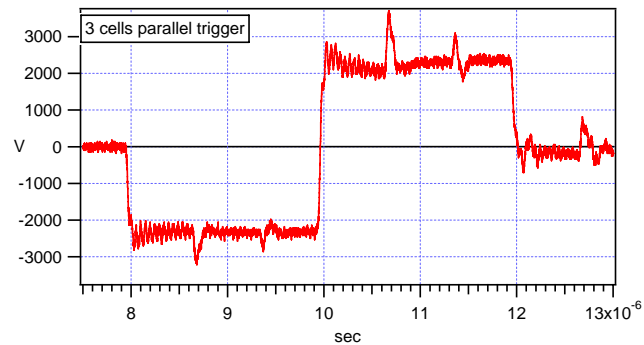


Fig. 57. Output voltage waveform when a parallel trigger is applied to three 2-turn induction cells

The 2-turn configuration has another major disadvantage; the secondary voltage is halved in comparison to the primary voltage.

Chapter 7 Beam simulator

The beam simulator is an imitation of a bunch monitor signal. The bunch monitor signal yields a pulse output corresponding to the rotating bunch. The pulse shape depends on the shape and the size of the bunch. The beam simulator signal is required in order to verify the control system designed for the KEK-DA induction acceleration system.

The bunch monitor signal is simulated using an arbitrary function generator, AFG-3252. The beam simulator signal has a varying frequency and a varying duty. The particle simulation results show that as the bunch accelerates, the velocity of the particles increases, thus changing the revolution period and the adiabatic barrier movement reduces the bunch size shown in Fig. 58. The bunch intensity also increases with acceleration, thereby changing the signal amplitude. However, the present beam simulator signal mimics the changing period and the pulse width of the bunch. This signal is required to refer to the intelligent control of induction acceleration system.

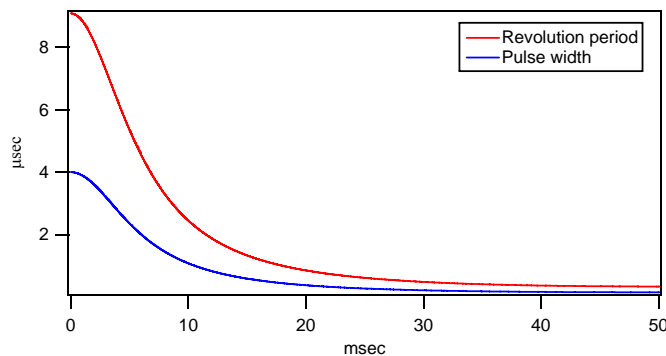


Fig. 58. Revolution period of argon +18 ions and the changes in pulse width with time

AFG is programmed to produce rectangular pulses as an approximation of the bunch signal. The period of the pulse corresponds to the revolution period in each turn, and the duty corresponds to the bunch length. The data regarding the revolution period is taken from particle simulations and is used to generate an input file for the software, which in turn generates a file in .txt format suitable for the ArbExpress® AXW100 software. This software is used for editing and creating waveforms for AFG, and yields a .set file and a .wfm file. The .set file is a settings file containing the amplitude, the period, the mode of operation, and the offset. On the other hand, the .wfm file describes the waveform which needs to be generated. After creating these files, they are placed in the memory of AFG [26]. The typical output of the beam simulator is shown in Fig. 59.

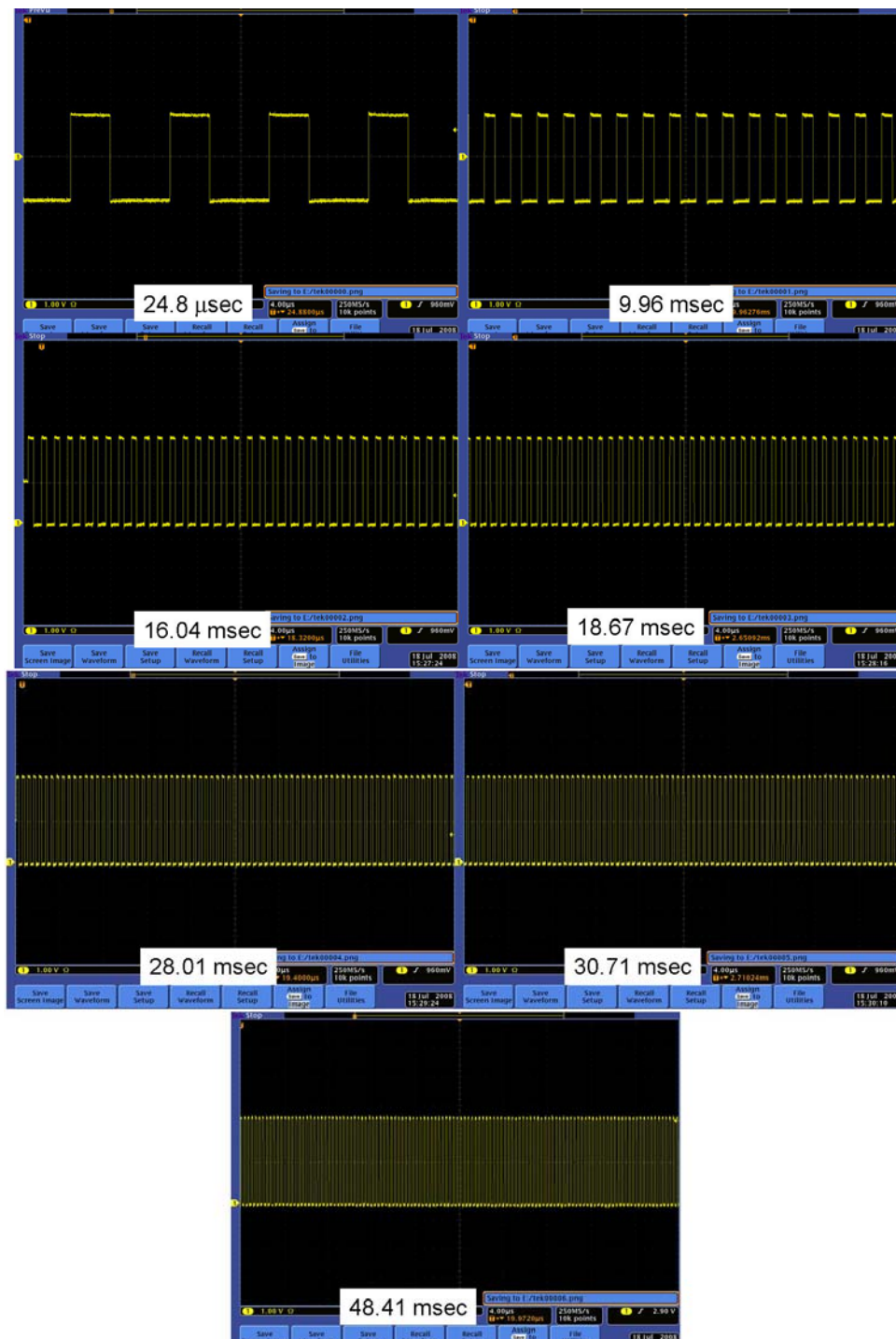


Fig. 59. Beam simulator signal at different times of the acceleration period.

The main limitation of the beam simulator comes from the maximum number of points which can be programmed into the AFG3000. For the AFG 3000 series, the maximum number of points on which a waveform can be described is ~ 131000 , where each point corresponds to a user-defined unit of time, e.g. 1 point $\equiv 1 \mu$ sec. This

sets an upper limit on the resolution of the waveform. If an acceleration period of 50 msec is accommodated in one file of the beam simulator, then each point corresponds to ~400 nsec. However, the pulse duty required at the end of the acceleration is less than 400 nsec, and therefore, in order to produce a waveform with a good resolution, the beam simulator signal is divided into four parts. In the first part, a 9.8 msec acceleration period is designed with a resolution of 75 nsec per point. Within these 9.8 msec, both Stage I and Stage II of the acceleration are covered. A 20 nsec resolution is set for the Stage II to Stage III transition, and approximately 2.3 msec is simulated around the stage transition in part two. The same settings are maintained for the Stage III to Stage IV signal in part three and part four for the signal near 48 msec. Hence, the induction acceleration control experiment is performed in parts near each stage transition.

Chapter 8 Intelligent acceleration control system for the KEK-DA

The acceleration scheme for KEK-DA is divided into four stages, as mentioned in Chapter 4. At each stage, different configuration of the gate trigger pulses is required since

- different sets of induction cells take part in changing the acceleration voltage depending on the stage,
- the induction cells are operated in a sophisticated operation mode, such as serial mode in time, parallel mode in time, and intermittent mode, depending on the stage,
- the set/reset timing always changes following the revolution of the ion bunch at all stages.

The developed gate control system can adjust the performance of all of these factors. Before providing the details of the logic of this control system, the technical aspects of the main components comprising the intelligent control system are described.

DSP introduction

DSP stands for Digital Signal Processor; therefore, analog signals are first converted into digital signals using an analog-to-digital converter, or ADC, after which the signal is processed digitally in the processor and then again converted to the analog signal with a digital-to-analog converter, or DAC. DSPs have a wide application in the communication industry. Wireless networks use DSPs for coding and decoding audio signals before and after transmission. DSPs are also used to control induction motors via monitoring feedback signals including current, voltage and position. In our application, DSPs are used extensively for the generation of gate trigger pulses for dynamic pulse lengths, and the signal from the ΔR monitor, which is an analog signal, is inputted into the DSP for processing, and, depending on the threshold cross over point a trigger pulse for the acceleration voltage, is generated or blocked by the DSP. The DSP has a fast processor ensuring real-time processing, which means that the input signal is processed and an output is produced before the next signal arrives for processing. This fast processing feature has applications in feedback processing. Here, we used a Texas instruments C64x series 1 GHz DSP starter kit (DSK 6416), which is shown in Fig. 60. Furthermore, Code Composer Studio is an environment used for programming DSP boards by using a high-level language such as C. The CPU clock frequency is 1 GHz. An AIC23 codec samples the analog signals at a frequency of 48 kHz. The analog input is provided at the line-in input by using an audio connector. The DSP has three timers denoted with T0, T1, and T2. T2 is the master timer, and its clock frequency is 125 MHz. There are 4 external interrupts, which, when activated, can start or stop a process running in the CPU [27]. These interrupt signals are located at peripheral expansion. Furthermore, the output of timers T0 and T1 is also taken from the peripheral expansion.

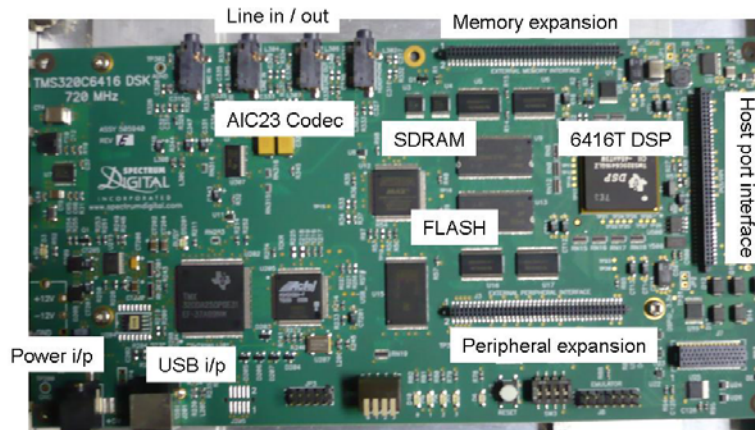


Fig. 60. A DSK 6416T board

8.1 Stage selector

The function of the stage selector is to generate level signals to indicate the stage of acceleration. It is required for controlling the acceleration stages in the downstream units, as will be described shortly. The stage selector signals are obtained by two DSPs working in synchrony to provide four digital outputs corresponding to each stage shown in Fig. 61. The state at each output depends on the stage of the acceleration. At each stage, only one output is held in the high state (logic 1), while the others are set to the low state (logic 0). During stage transitions, all outputs of the stage selector are held in the low state, which means no output. The onset of the acceleration B_{\min} signal (from a pulse generator operated at 10 Hz) is triggered as an interrupt signal to the two DSPs to start counting. EXTINT5 is used to input the B_{\min} input the current signal from a pulse generator operated at a frequency of 10 Hz. the TIMER0 and TIMER1 periods are set in the program in the DSP memory. These timers can be operated in clock mode, as shown in Fig. 62 [28], where clock mode operation is used to provide a digital signal. In order to ensure proper stage change without spurious signals, which can occur as a result of a mismatch of the logic gate state change (from high to low or vice versa), a 10 μ sec OFF time is set in the stage selector during stage transitions. The stage selector outputs are shown in Fig. 63.

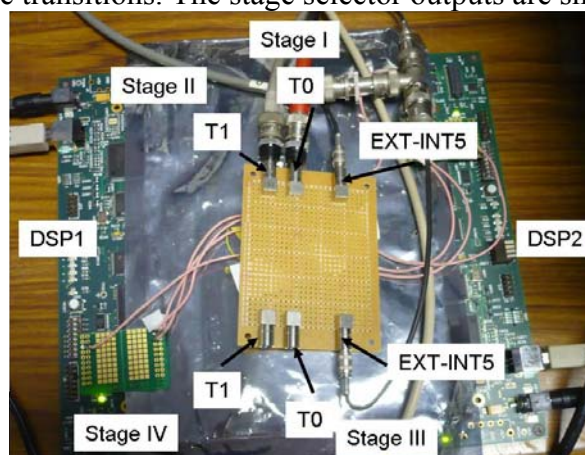


Fig. 61. Stage selector DSP

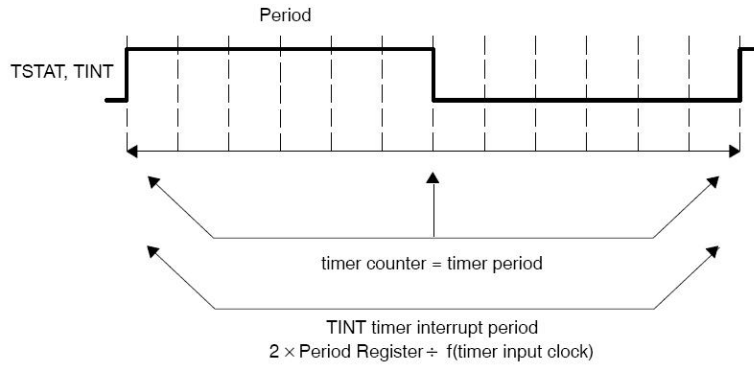


Fig. 62. Clock mode

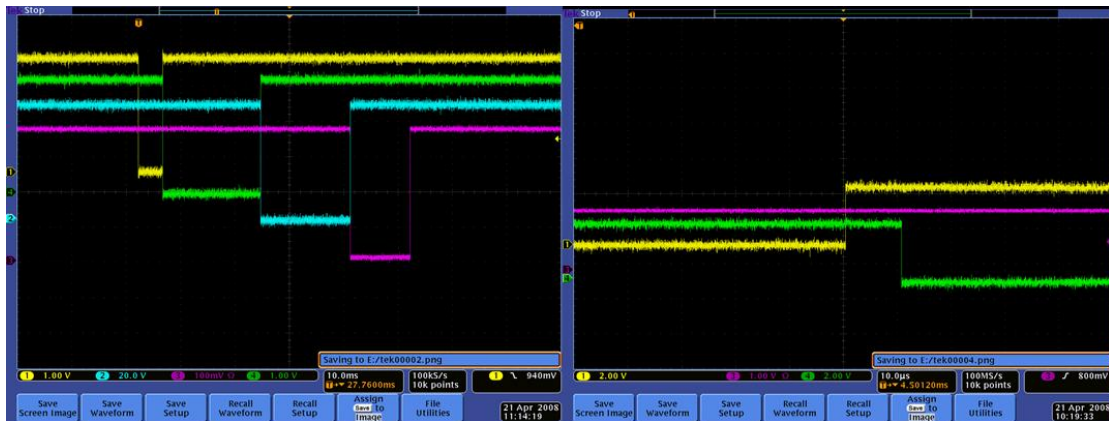


Fig. 63. (a) Output of the stage selector DSP. Stage I (yellow), Stage II (green), Stage III (blue), and Stage IV (pink). (b) The 10 μ sec difference between stage transition.

8.2 DSP sets for dynamic pulse width and amplitude

DSP set1 and set2, as described in regard to the intelligent acceleration control system, are capable of generating dynamic pulse lengths depending on the bunch monitor signal (in the present case, the beam simulator signal). The beam simulator signal is applied to interrupt EXTINT4, and the B_{\min} 10 Hz signal is applied to EXTINT5 in all DSP's in each set for the purpose of generating a synchronized output. Each DSP set consists of four DSPs giving the start and the end of the SET and RESET pulses shown in Fig. 64 as well as additional hardware, presented in Fig. 65, where 8 PCs are connected to the respective DSPs for the purpose of programming the DSP functions. These pulses are generated at timer output T0 and T1 of the DSP. Then, the pulses are applied to a pulse stretcher unit for obtaining a long pulse. The pulse stretcher is essentially a flip-flop circuit which changes its state with the arrival of each pulse. Thus, the flip-flop is held at the logic high between two pulses from DSP, yielding a longer output pulse. Since the start and end pulses are controlled by separate DSPs, it is possible to generate a dynamic pulse width by using this scheme.

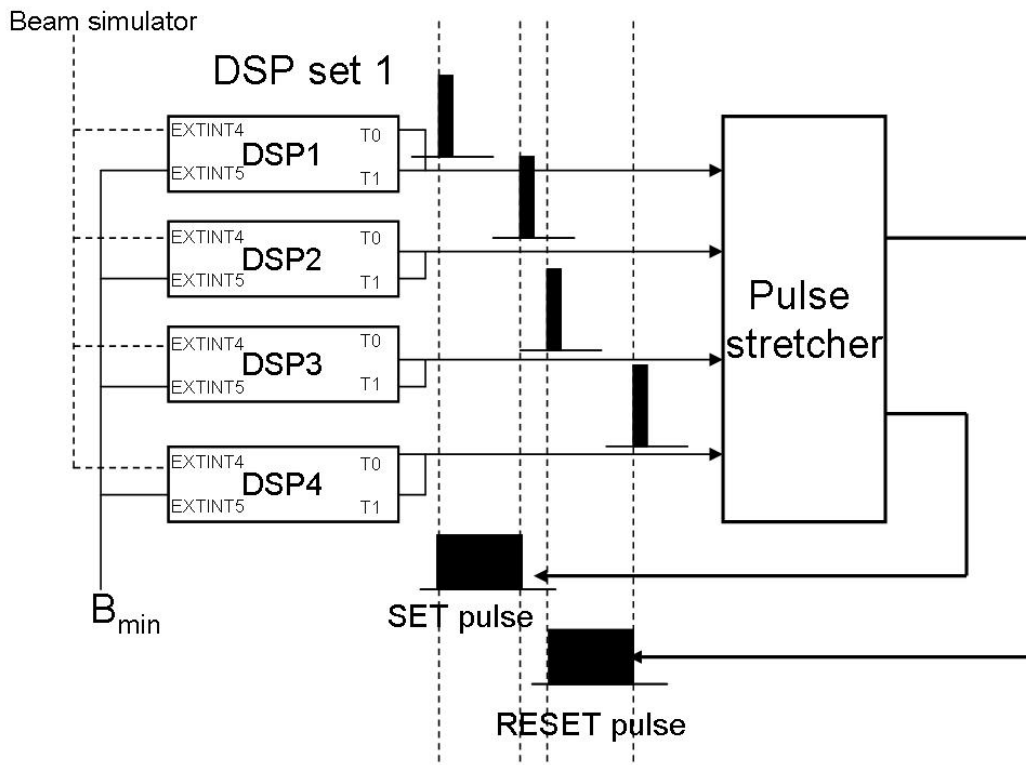
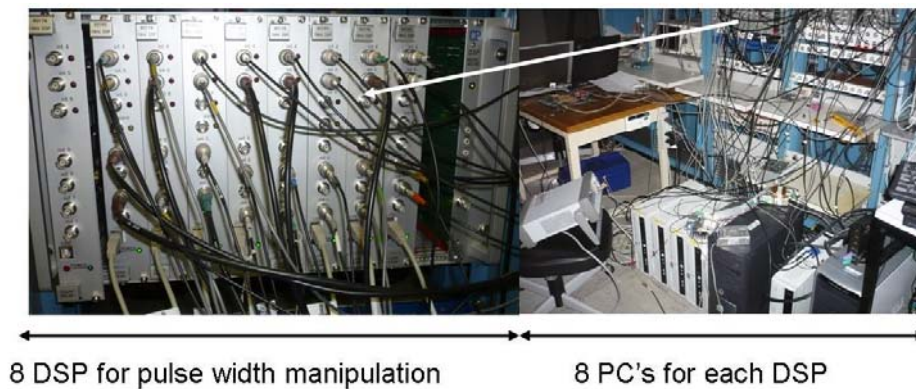


Fig. 64. A schematic diagram of the dynamic pulse generation using a DSP set.



8 DSP for pulse width manipulation 8 PC's for each DSP

Fig. 65. DSPs for the generation of long pulses

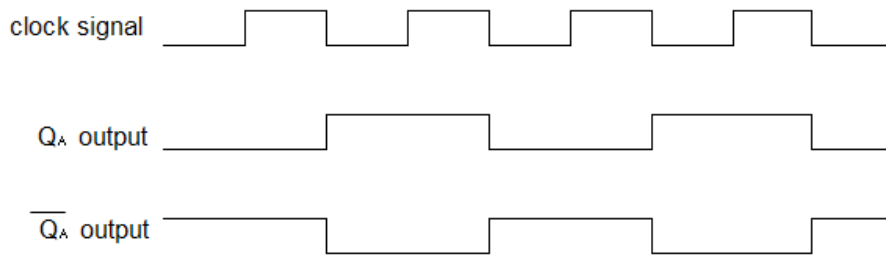
In Stage I, a long acceleration pulse is achieved by using two DSP sets in serial operation. Thus, four signals from DSP set1 are used for generating set and reset pulses for cell#1, and the DSP set2 provides signals for cell#2.

8.3 Frequency dividers for intermittent operation

The intermittent operation of the induction cells above frequencies of 1 MHz is controlled by using a frequency divider circuit. A frequency divide-by-2 circuit is essentially a synchronous 4-bit counter. The output Q_A of the counter IC 74161 produces an output of half the clock frequency. The beam simulator signal is provided as a clock signal to the frequency divider circuit. Another output \bar{Q}_A is obtained after passing through a NOR gate to obtain the opposite output (i.e. when Q_A output is high,

the output after the NOR gate is low). Thus, the two outputs alternatively become high at half the beam simulator frequency shown in Fig. 66 (a), and different induction cells are selected at alternate turns.

(a)



(b)

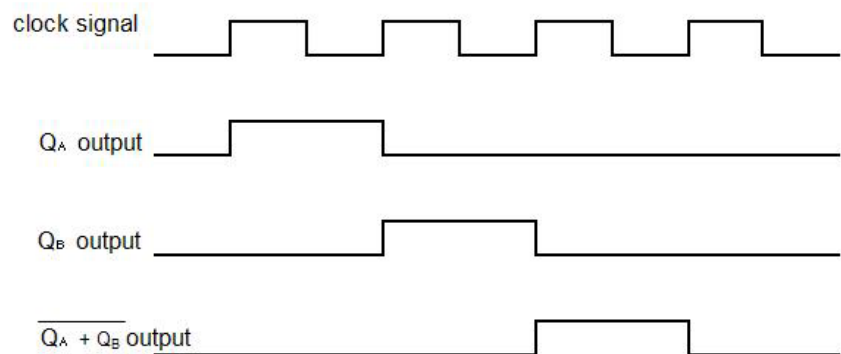


Fig. 66. A schematic representation of (a) frequency divided by 2, and (b) frequency divided by 3.

In Stage IV, a frequency divide-by-3 circuit (again using one more IC 74161 is made with three outputs Q_A and Q_B and $(\overline{Q_A + Q_B})$) is used, and each output is held high alternatively at the $1/3$ of the input frequency shown in Fig. 66 (b). The maximum switching time for the IC 74161 is 25 nsec according to the datasheet.

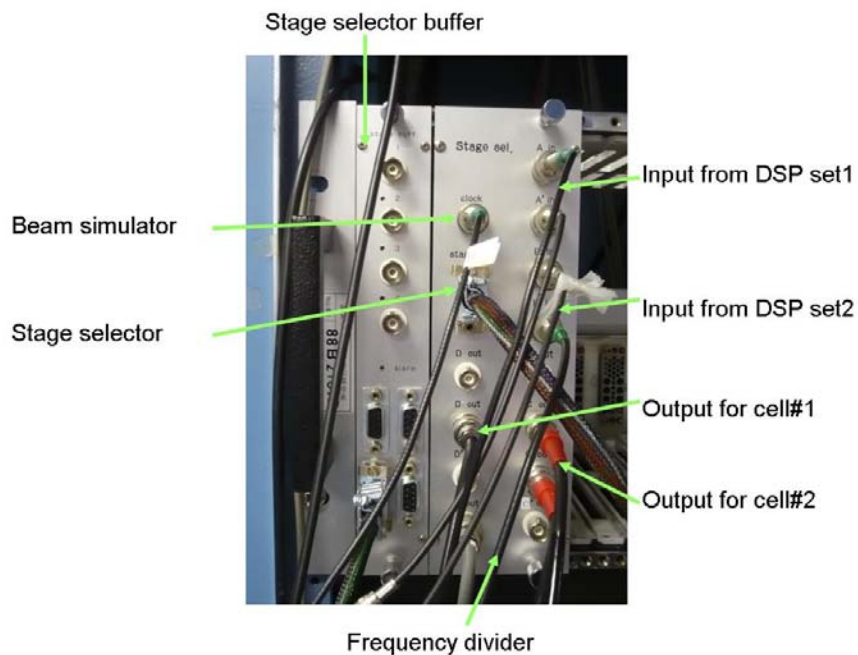


Fig. 67. Frequency divider

The picture of the frequency divider is shown in Fig. 67. The beam simulator signal, the stage selector, and the DSP set1 and DSP set2 signals are applied as inputs, while the output for cell#1 is taken from C and D for set and C' and D' for reset, respectively. The bunch monitor signal needs to be processed before applying it as an input clock frequency to the frequency divider circuits in actual operation. Also, the delay time in the signal processing and in the downstream circuit needs to be carefully taken into account, as described later.

8.4 Logic units

The logic units are various logic gates used to connect the right pair of induction cells in each stage and during the intermittent operation. Since many logic gates are connected in series, the state change time for each logic unit is accumulated in the total delay time in the intelligent signal processing. The main logic units are the stage selector signal divider units for distribution of stage selector outputs using IC 7442. The maximum propagation delay in this unit is 30 nsec according to the datasheet. Eight input positive NAND gates IC 7430 are used to direct set and reset signals to the switching power supply. This takes a maximum of 22 nsec from the switching of the state.

8.5 Induction acceleration control system

Stage I of the acceleration period lasts for 7 msec from the start of acceleration for Argon ion acceleration in KEK-DA. In this stage, two cells are triggered in serial mode, forming a long acceleration voltage pulse as shown in Fig. 32. Therefore, a 2-turn long pulse induction cell is used in this stage with an output voltage of 800 V. The start of the acceleration signal comes from the B_{\min} signal of magnet ramping, which is labeled as "c" in Fig. 68. This gives an interrupt signal to the stage selector DSP and the DSP set1 and set2. The stage selector DSP is responsible for the selection of the induction acceleration cells in each stage, while DSP set 1 and set 2 are programmed for the generation of set and reset gate trigger signals.

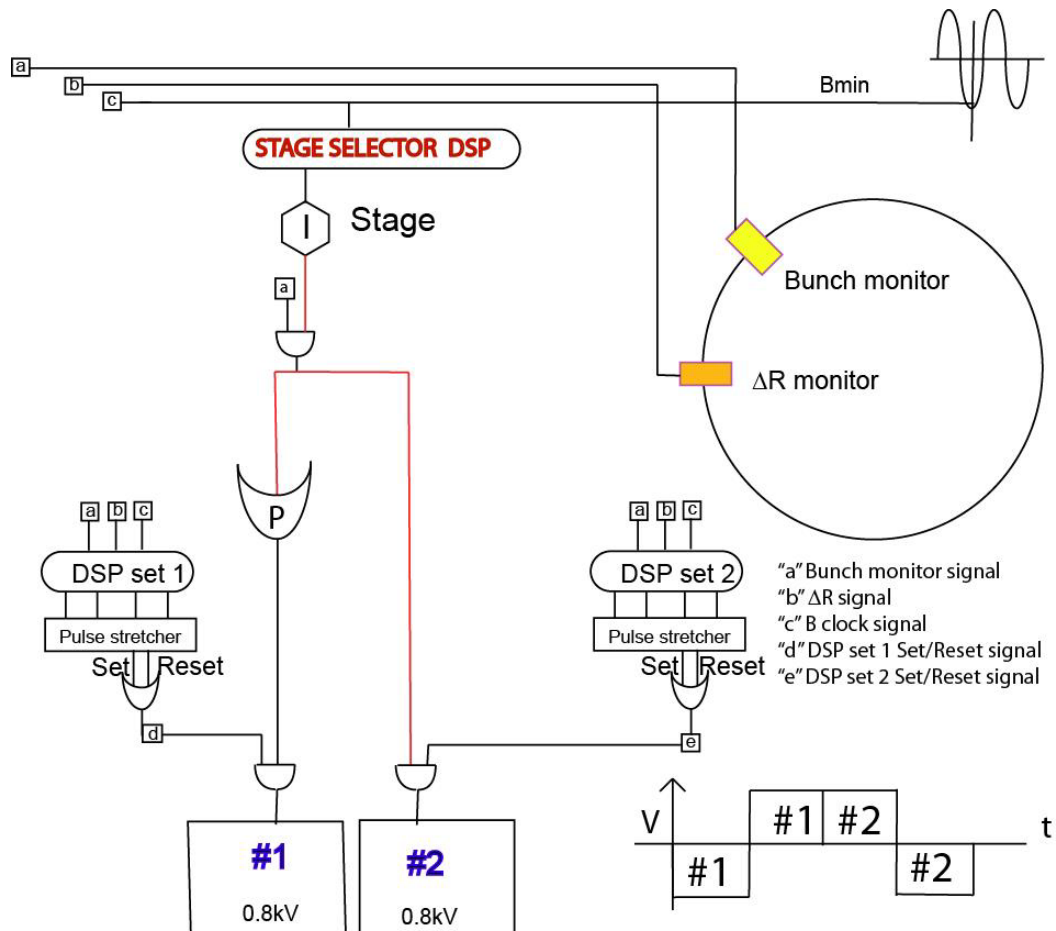


Fig. 68. A schematic diagram of the control of induction acceleration scheme in Stage I.

The correct timing and length of the acceleration voltage pulse are synchronized with the bunch signal, which is labeled as "a". Each DSP set consists of four DSPs, which process information of regarding the bunch signal, and generates four signals for the start and stop of the set/reset signals. These signals then pass through the pulse stretcher to obtain a long-step voltage pulse. The signal labeled as "b" is from the ΔR signal, which decides the pulse density control on the basis of the beam orbit. These three signals are first logically processed in the DSPs, and then the set/reset pulses are directed to the switching power supply through logic gates. DSP set2 is used when long acceleration voltage pulses are required.

In Stage II of acceleration period, i.e. from 7 msec to 21.6 msec, three cells are triggered in parallel mode, thus forming a superimposed acceleration voltage pulse of $3 \times 0.8 \text{ kV} = 2.4 \text{ kV}$ as shown in Fig. 69. Therefore, when the Stage II signal is set at logic high, the set and reset pulses are directed to cells #1, #2 and #3 at the same time. Only DSP set1 is used in this stage.

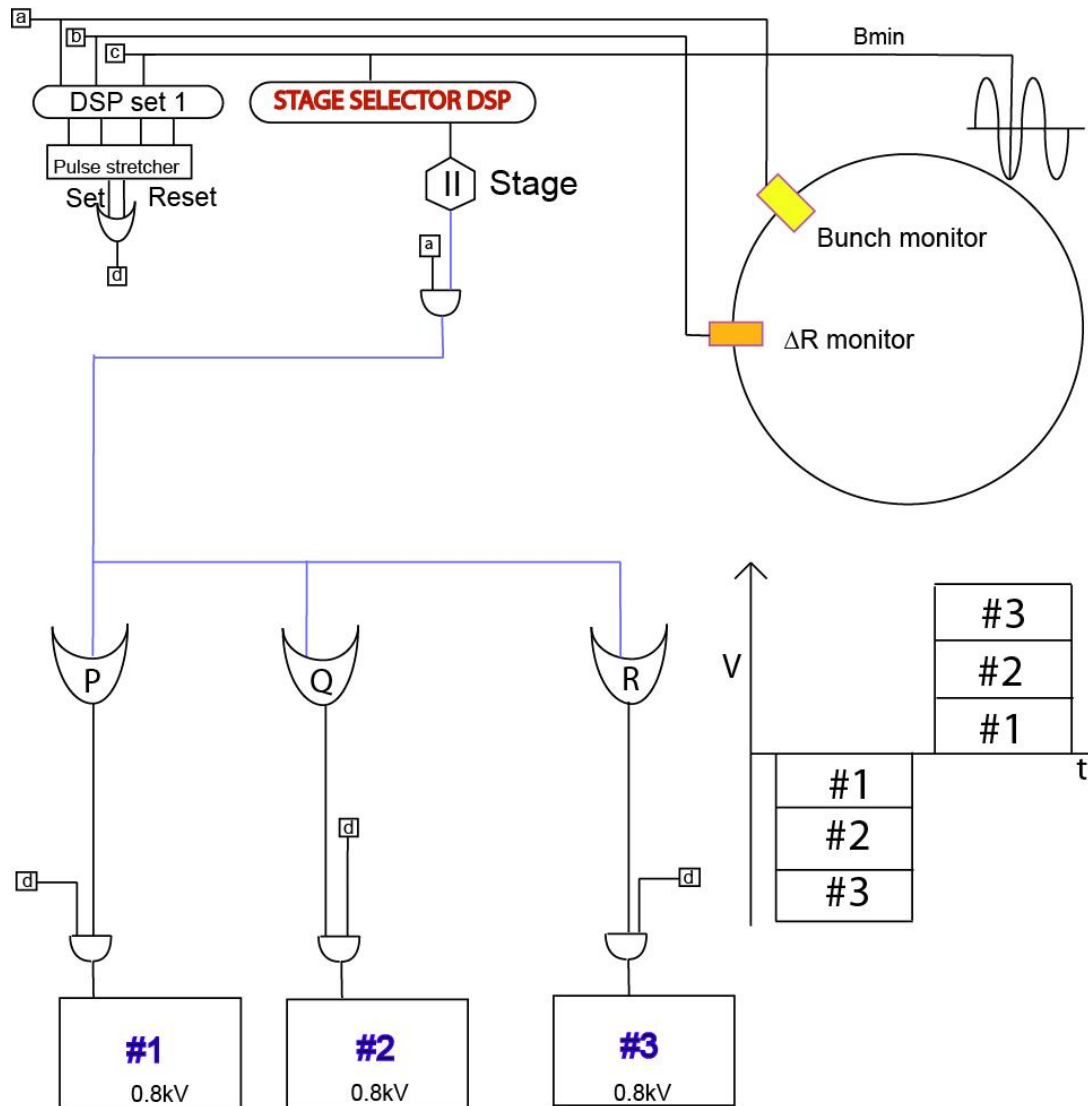


Fig. 69. A schematic diagram of the control of the induction acceleration scheme in Stage II.

In Stage III of the acceleration period, i.e. from 21.6 msec to 38 msec, the revolution frequency becomes greater than 1 MHz. Therefore, the intermittent operation of the induction cell starts in this stage. Since the intermittent operation starts from this stage onwards, additional processing is required to direct the set and reset signals to the correct set of induction cells. The bunch signal is processed to give an input clock frequency to the frequency divide-by-2 circuit. The frequency divider circuit outputs are denoted as N^{th} and $(N+1)^{\text{th}}$ in Fig. 70, and are connected to cell #1 and #4 and #2 and #5, respectively. Both the old and the new induction cells are used in order to obtain a symmetric acceleration voltage providing $(0.8+1.8) \text{ kV}=2.6 \text{ kV}$. The gate trigger frequency for each cell is therefore maintained at less than 1 MHz.

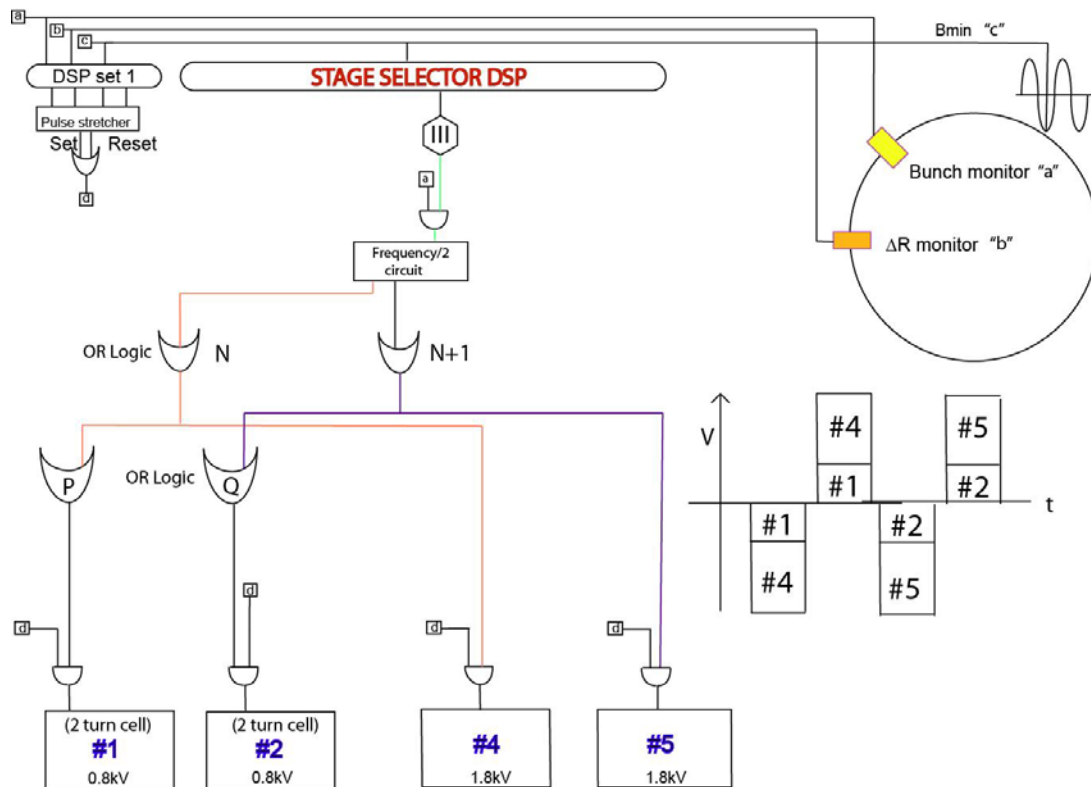


Fig. 70. A schematic diagram of the control of the induction acceleration scheme in Stage III.

Finally, in Stage IV of the acceleration period, i.e., from the beginning at 38 msec until the end at 50 msec, the particle revolution frequency becomes greater than 2 MHz. Therefore, three sets of induction cells are triggered intermittently. A frequency divide-by-3 circuit is used in order to select the correct pair for each turn in this stage. The output N^{th} , $(N+1)^{\text{th}}$ and $(N+2)^{\text{th}}$ are selected once in three revolution periods. A superimposed acceleration voltage pulse of $(0.8+1.8) \text{ kV}=2.6 \text{ kV}$ is provided in each turn, as shown in Fig. 71.

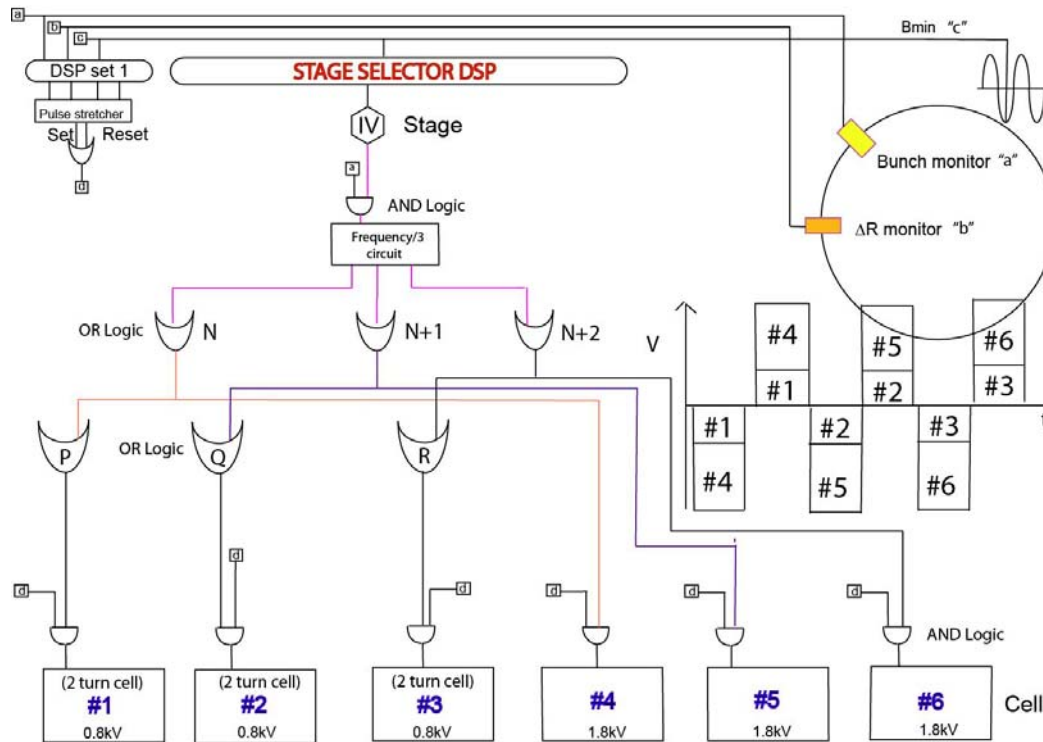


Fig. 71. A schematic representation of the control of the induction acceleration scheme in Stage IV.

The complete induction acceleration control system is shown in Fig. 72. One of the important requirements for this control system is that the stage transition, i.e. the transition from Stage I to Stage II, etc. should be smooth, ensuring that the correct pair of cells operate in each stage. Therefore, when a stage transition takes place, the gate trigger should not be allowed to reach the switching power supply in order to avoid mistrigging and the accidental generation of operation frequencies greater than 1 MHz. The ambiguity in stage selection during transition also depends on the time required by the logic units to change state from low to high or vice versa. The state change time is of the order of tens of nanoseconds for logic gates. Therefore, if time of the order of microseconds is applied to the logic gates, then mistrigging will not occur. Therefore, the stage selector DSP is programmed to maintain the outputs at logic 0 level for $10 \mu\text{sec}$ during stage transitions. In this time period, acceleration voltage is not generated, and this off time of $10 \mu\text{sec}$ is safe from the point of view of beam dynamics, as confirmed by the simulations.

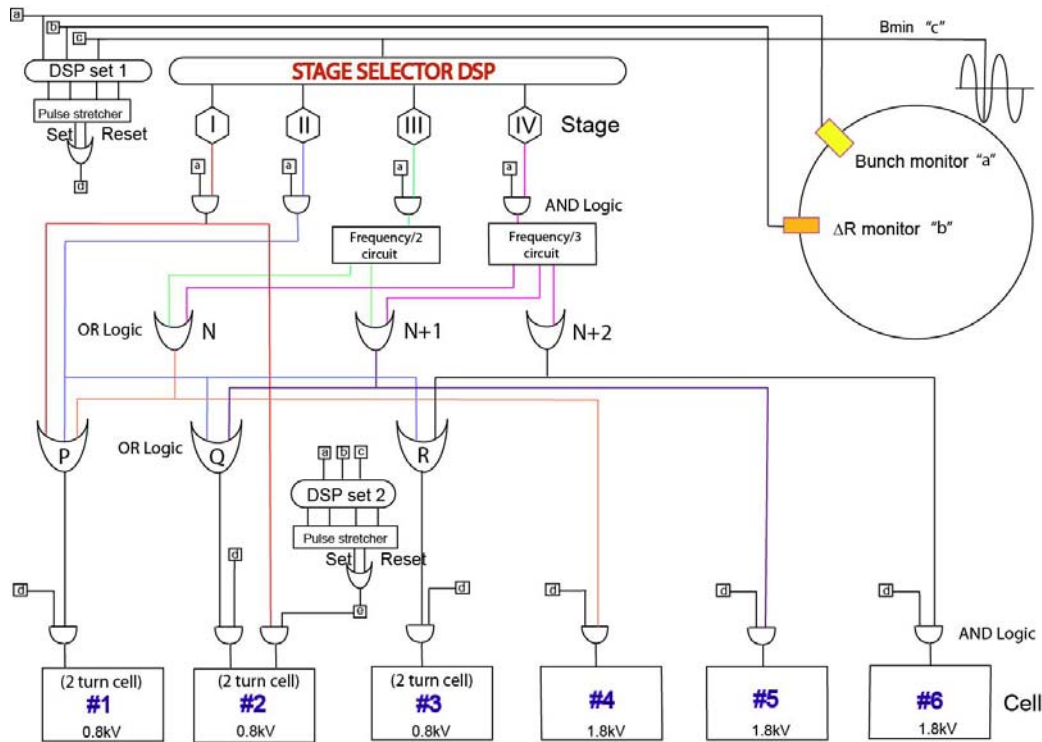


Fig. 72. A schematic representation of the complete induction acceleration control system.

A block diagram of the setup required for the generation of confinement voltage pulses is shown in Fig. 73. Since two induction cells are used in Stage I and Stage II to provide barrier voltage, two induction cells, namely ID#7 and ID#8, which are dedicated for confinement, are triggered depending on the timing information generated from the bunch signal. In Stage III and Stage IV, a single induction cell with fixed pulse width is triggered intermittently. Therefore, a frequency divider is required for distributing the trigger signals.

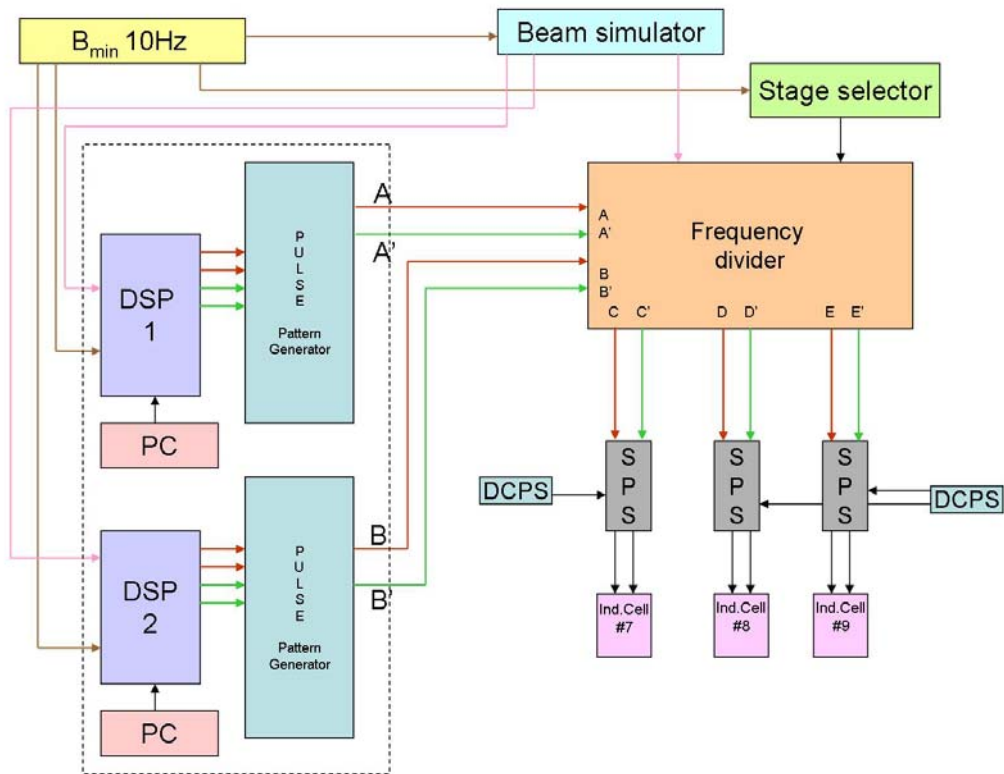


Fig. 73. A block diagram of the generation of confinement voltage

Chapter 9 Experimental demonstration of the acceleration scheme using the beam simulator

Presently, Stage I and Stage II are verified using the induction acceleration control system set up as shown in Fig. 74.

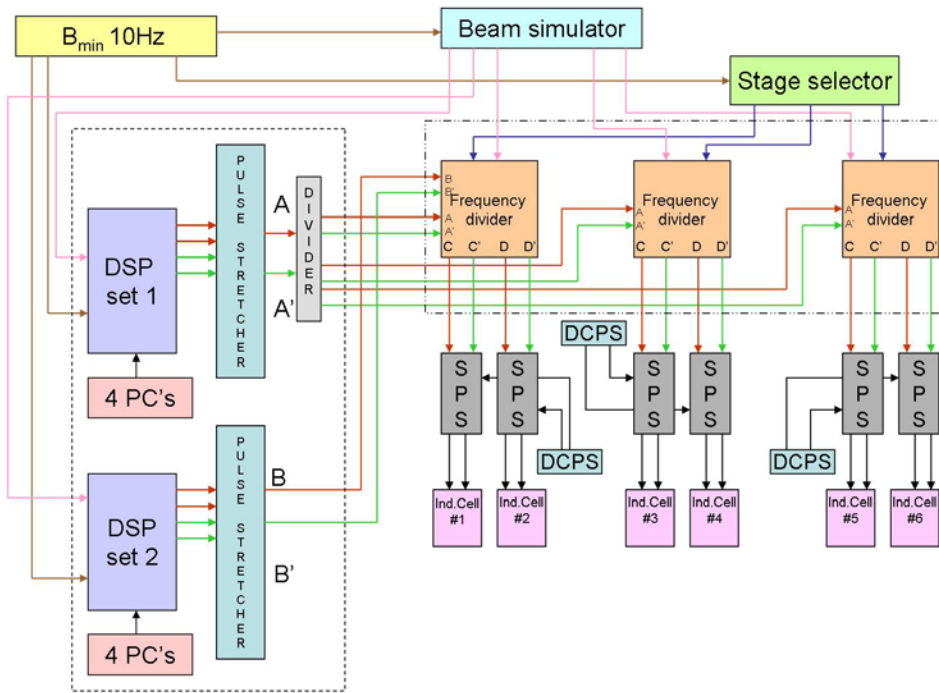


Fig. 74. Setup of the induction acceleration control system

The gate trigger output using the control module is shown in Fig. 75 (a) to (e). Fig. 75 (a) shows the beam simulator signal and the stage selector signals for Stage I and Stage II. A time lag of 10 μsec was observed between the beam simulator output and the stage selector output, which is adjustable in the DSP program. Fig. 75 (b) shows the first few pulses at the start of the acceleration in Stage I. As can be seen from the figure, spurious pulses are generated at the beginning. This is due to an error in the timer output of the DSP sets. Therefore, a process of trial and error is required in order to reduce this effect. Fig. 75 (c) shows the output after 100 μsec from the start of the acceleration. The serial trigger is generated as expected. Fig. 75(d) shows the transition region from Stage I to Stage II, i.e., from serial operation to parallel operation. A gap of 10 μsec is generated between the stages as designed in the stage selector logic. The transition from Stage I to stage II is smooth, without any error pulses in Stage II. Fig. 75 (e) shows the output later during Stage II near 9.8 msec. The triggers are generated in parallel mode throughout as expected, without any error pulses. Fig. 76 shows a schematic representation of the control system required for the generation of the confinement voltage pulse. As described in the acceleration scheme, the bunch is placed at the center of the barrier voltage in Stage III and Stage IV. In these stages, the revolution frequency is greater than 1 MHz and 2 MHz, respectively.

Therefore, the frequency divider is required for distributing the trigger signals to the correct cells.

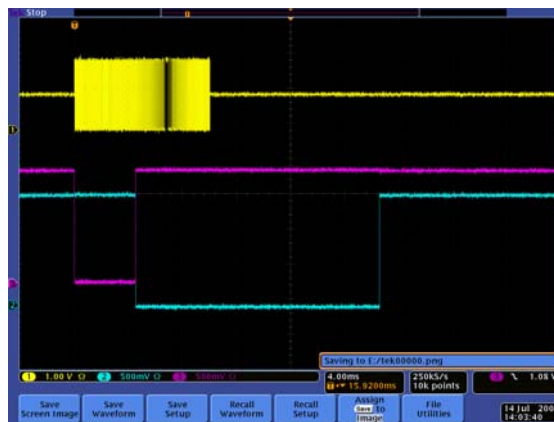


Fig. 75.(a) Stage selector signals Stage I is shown in pink, Stage II is shown in blue and beam simulator is shown in yellow.



Fig. 75. (b) Output from the induction acceleration control system in the early acceleration region of Stage I, together with the set signal (pink and yellow) and the reset signal (blue and green).



Fig. 75. (c) Output from the induction acceleration control system at 100 μ sec from the start. Long pulse generation in Stage I together with the set signal (pink and yellow) and the reset signal (blue and green).

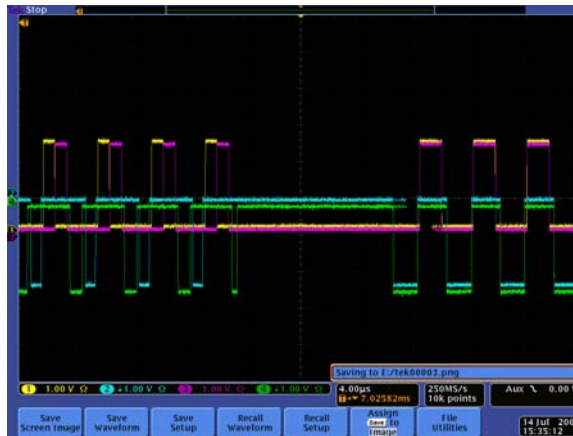


Fig. 75. (d) Output from the induction acceleration control system during the transition from Stage I to Stage II, where the 10 μ sec sleep time is included. The set signal (pink and yellow) and the reset signal (blue and green) are also shown.

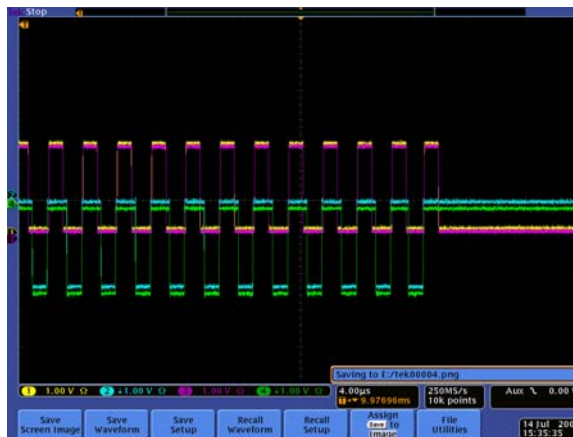


Fig. 75. (e) Output from the induction acceleration control system at the end of Stage II. The set signal (pink and yellow) and the reset signal (blue and green) are shown.

The generation of an acceleration voltage trigger in Stage I and Stage II is verified using the control system. Another two frequency dividers are awaited in order to demonstrate the intermittent operation of Stage III and Stage IV. The high-voltage tests and the intermittent operation will be verified after the hardware becomes available. Furthermore, the experimental results at high voltages demonstrating all stages will be included in the final stage of the thesis submission.

Remaining tasks-

1. High-voltage run using the control system in Stage I and Stage II.
2. Demonstration of the intermittent operation in Stage III and Stage IV by using the control system.
3. High-voltage run for Stage III and Stage IV.

Chapter 10 Conclusion

An induction acceleration scheme has been designed for the acceleration of argon ions in the KEK-DA, and the required devices, including the control system, have been developed and demonstrated. The process of acceleration has been verified with the help of extensive computer simulations. It is concluded that this scheme is achieved by employing the existing induction acceleration system and its modification, which is characterized by the finite and constant output voltage, the limited pulse length, and the limited repetition rate.

A long-pulse induction cell was developed in order to realize the acceleration scheme along with an intelligent induction acceleration control system. In the long-pulse acceleration cell, the droop and the undershoot were reduced by increasing the inductance of the cell by four times at the expense of a reduction of the output voltage. Owing to the nature of the pulsed power device, some level of reflection of the pulse is inevitable, and reflection voltage was observed on the flat top of the acceleration voltage pulse. Furthermore, the first reflection amplitude is considerable, and later reflections damp out quickly in a 2 μ sec long pulse. The performance of the long-pulse induction cell was verified in the experiment with the beam simulator signals for Stage I and Stage II, where these long-pulse induction cells are used exclusively in sequential and parallel operation. The gate trigger signals can be generated successfully for both types of operation by the DSP, with a smooth transition between the stages. These features are crucial to demonstrating the overall acceleration scheme.

In the near future, many further improvements can be incorporated into the present system. For instance, beam intensity fluctuations in the beam simulator signal must be incorporated in order to mimic a realistic bunch signal. A protection circuit dedicated to preventing the operation of the present switching power supply at a repetition rate greater than 1 MHz might be useful in case of a failure of the timing signals produced by the stage selector DSP. The delay in the signal transmission is not taken into consideration in the present experiment. The delay in signal transmission was studied for the proof-of-principle experiment, and can be straightforwardly applied to the KEK-DA. If the switching frequency of the switching elements can be increased without serious heat deposition problems, then fewer cells will be required for acceleration.

The highlights of the present thesis can be summarized as follows:

- (1). Development of the acceleration scheme for KEK-DA.
- (2). Verification of the acceleration scheme with simulations.
- (3). Development of long-pulse induction cells.
- (4). Development of intelligent induction acceleration control system.

Appendix A

From the force balance equation, we obtain

$$\frac{Am_0\gamma(\beta c)^2}{\rho} = q(\beta c)B \quad (\text{A.1})$$

where $q = Ze$

The energy $E = Am_0\gamma c^2$

$$\text{Changes in the energy } \Delta E = q\bar{V}_{acc} \quad (\text{A.2})$$

Taking the average of the energy change over one turn, $T = \frac{C_0}{\beta c}$, we can rewrite Eq.

(A.2) as

$$\frac{d\bar{E}}{dt} = \frac{q\bar{V}_{acc}\beta c}{C_0} \quad (\text{A.3})$$

$$\frac{Am_0c(\beta\gamma)}{\rho} = qB$$

Also, $\beta\gamma = \sqrt{\gamma^2 - 1}$

$$\frac{d(\beta\gamma)}{dt} = \frac{dx}{dt} \text{ where } x = \sqrt{\gamma^2 - 1}$$

$$\frac{dx}{dt} = \frac{1}{\beta} \frac{d\gamma}{dt}$$

$$\frac{Am_0c^2}{c\rho\beta} \frac{d\gamma}{dt} = q \frac{dB}{dt}$$

$$\text{However, } \frac{dE}{dt} = Am_0c^2 \frac{d\gamma}{dt} = \frac{q\bar{V}_{acc}\beta c}{C_0}$$

$$\frac{\bar{V}_{acc}}{\rho C_0} = \frac{dB}{dt}$$

$$\bar{V}_{acc} = \rho C_0 \frac{dB}{dt} \quad (\text{A.4})$$

Appendix B

Transverse focusing provided by the lattice of the booster remains the same for the acceleration of ions, as shown below. The transverse motion of the particles is governed by the following equation

$$Am \frac{d(\gamma v_{\perp})}{dt} = -Zev_{\parallel} B' x \quad (\text{B.1})$$

Where $B' \equiv \frac{\partial B}{\partial x}$

Changing from time to space coordinates, we can rewrite Eq. (B.1) as

$$\gamma c \beta_{\parallel} \frac{d}{ds} \left(\frac{dx}{ds} \right) = -\frac{Z}{A} \left(\frac{e}{m} \right) B' x \quad (\text{B.2})$$

Rearranging Eq. (B.2), we can write

$$\frac{d^2 x}{ds^2} + K(s)x = 0$$

$$\text{where } K(s) = \frac{Z}{A} \left(\frac{e/m}{c\beta\gamma} \right) \frac{\partial B_y}{\partial x} \quad (\text{B.3})$$

Also, since $\beta\gamma = \frac{Z}{A} \left(\frac{e\rho}{mc} \right) B$, substituting into Eq. (B.3), we obtain

$$K(s) = \frac{1}{B\rho} \frac{\partial B_y}{\partial x} \quad (\text{B.4})$$

The $K(s)$ value does not depend on either the ion mass or its charge state, as seen from Eq. (B.4). Therefore, the tuning of the betatron for any ion or any charge state remains the same.

References -

- [1] K. Takayama and J. Kishiro, *Nucl. Inst. Meth. A* **451** (2000) p. 304.
- [2] K. Takayama, Y. Arakida, T. Dixit, T. Iwashita, T. Kono, E. Nakamura, K. Otsuka, Y. Shimosaki, K. Torikai, and M. Wake, *Phys. Rev. Lett.* **98** (2007) pp. 054801.
- [3] R. J. Van de Graaff, *Phys. Rev.* **38**, 1919 (1931).
- [4] L.W. Alvarez, *Phys. Rev.* **70**, 799 (1946)
- [5] E. O. Lawrence and N. E. Edelfsen, *Science*,**72**, 376-7 (1930)
- [6] D. W. Kerst and R. Serber, *Phys. Rev.* **60**, 53-8 (1941)
- [7] E. M. McMillan, *Phys. Rev.* **68**,143 (1945)
- [8] M. Watanabe, M. Nakajima, K. Horioka, K. Takayama, M. Shiho and J. Kishiro, *Rev. Sci. Inst.* **73**, pp. 1756-1760 (2002)
- [9] M. Watanabe, Ph.D Thesis, Tokyo Institute of Technology, (2001)
- [10] K. Torikai, Proceedings of RPIA2002, p. 70-73 (2002)
Ph.D Thesis, Kyushu University (2006)
- [11] K. Koseki, K. Takayama, and M. Wake, *Nucl. Inst. Meth. A* **554**, (2005) pp. 64.
Ph.D Thesis, The Graduate University of Advanced Studies (2005)
- [12] M. Wake, Y. Arakida, K. Koseki, Y. Shimosaki, K. Takayama, K. Torikai, W. Jiang, K. Nakahiro and A. Tokuchi, Proceedings of PAC07, p. 251, (2007)
<http://accelconf.web.cern.ch/AccelConf/p07/PAPERS/MOPAN042.PDF>
- [13] K. Takayama, K. Koseki, K. Torikai, A. Tokuchi, E. Nakamura, Y. Arakida, Y. Shimosaki, M. Wake, T. Kouno, K. Horioka, S. Igarashi, T. Iwashita, A. Kawasaki, J. Kishiro, M. Sakuda, H. Sato, M. Shiho, M. Shirakata, T. Sueno, T. Toyama, M. Watanabe, and I. Yamane, *Phys. Rev. Lett.* **94**, (2005) pp. 144801.
- [14] K. Torikai, K. Takayama, Y. Shimosaki, Y. Arakida, E. Nakamura, D. Arakawa, S. Igarashi, T. Iwashita, A. Kawasaki, J. Kishiro, K. Koseki, T. Kouno, H. Sato, M. Shirakata, T. Sueno, A. Tokuchi, T. Toyama, and M. Wake, KEK Preprint 2005-80 (2005), submitted to *Phys. Rev. ST-AB*
- [15] K. Takayama, Y. Shimosaki, K. Torikai, and Y. Arakida, Japan Patent No.3896420 and PCT/JP2006/308502.
- [16] T. Dixit, Y. Shimosaki, and K. Takayama, *Nucl. Inst. & Meth. A*, **582** (2007) pp. 294-302

- [17] H. Wiedemann, Particle Accelerator Physics, Springer.
- [18] K. Takayama , Y. Arakida, T. Iwashita, Y. Shimosaki, T. Dixit , and K. Torikai , *J. Appl. Phys.* **101** (2007) pp. 063304
- [19] H. Suzuki, Y. Arakida, T. Iwashita, M. Kawai, T. Kono, K. Takayama , K. Okazaki, and S. Inagaki, Proceedings of EPAC08, MOPC156
<http://cape.elettra.eu/E08Papers/MOPC156.PDF>
- [20] E. Nakamura, T. Adachi, Y. Arakida, T. Dixit, S. Inagaki, T. Iwashita, M. Kawai, T. Kikuchi, T. Kono, K. Okazaki, H. Sato, Y. Shimosaki, K. Takayama, K. Torikai, and M. Wake, Proceedings of PAC07, Albuquerque, NM USA, p. 1490
- [21] T. Dixit, T. Iwashita, and K. Takayama, *to be submitted to Nucl. Inst. & Meth.A*
- [22] K. Takayama, T. Adachi, E. Nakamura, and H. Someya, Proceedings of EPAC08, THPC156, <http://cape.elettra.eu/E08Papers/THPC107.PDF>
- [23] T. Iwashita, T. Dixit, Y. Arakida, T. Kono, K. Okazaki, Y. Shimosaki, and K. Takayama, Proceedings of PAC07, Albuquerque, NM USA, p. 1484 *to be submitted to Nucl. Inst. & Meth.A*
- [24] Y. Shimosaki, E. Nakamura, K. Takayama, K. Torikai, M. Watanabe, M. Nakajima, and K. Horioka , *Phys. Rev. ST - AB*, **7**, (2004), pp. 014201.
- [25] <http://www.hilltech.com/pdf/hl-fm10-cFinemetIntro.pdf>
- [26] AFG3000 series reference manual
- [27] TMS320C6416T DSK Technical Reference
- [28] TMS320C6000 DSP 32-Bit Timer Reference Guide

List of Figures:

1.	A schematic diagram of the Van de Graaff accelerator
2.	The 40MeV Proton linac
3.	A schematic diagram of a cyclotron
4.	A schematic diagram of a betatron
5.	KEK-12 GeV proton synchrotron ring composition
6.	(a) A schematic diagram of the RF synchrotron and the induction synchrotron (b) Accelerator configuration
7.	Voltage profile of the induction synchrotron
8.	Equivalent circuit for an induction acceleration system.
9.	Cross-sectional view of an induction cell
10.	Switching power supply
11.	DSK 6416 unit
12.	Optical trigger unit
13.	Hardware components of an induction synchrotron
14.	A schematic diagram of an induction synchrotron control system used in the POP experiment
15.	Results from the proof-of-principle experiment of the induction synchrotron. From top to bottom, ΔR feedback signal (green), slow intensity monitor signal (yellow), acceleration voltage pulses (pink), bunch monitor signal (blue), and bending magnet ramping pattern (orange)
16.	A schematic diagram of the accelerator ring showing an observation point
17.	RF acceleration voltage and synchronous particle phase
18.	Hamiltonian contours in phase space for the RF voltage
19.	A schematic diagram of the Hamiltonian contours in an induction synchrotron
20.	Voltage profile of the rectangular barrier
21.	(a) Barrier voltage shape with three distinct regions encountered by the particles (b) A schematic diagram of the Hamiltonian contour in phase space (W, ϕ).
22.	(a) A schematic diagram of the rise and fall shape of the barrier pulse. (b) A Hamiltonian contour in phase space (W, ϕ).
23.	A schematic diagram of the stationary bucket in RF acceleration
24.	A schematic diagram of the stationary bucket in an induction synchrotron
25.	Variation of the synchrotron tune in RF and induction synchrotrons
26.	A schematic diagram of the KEK-PS booster synchrotron
27.	Picture of the KEK-PS booster synchrotron
28.	Dispersion function plot of the KEK-PS booster synchrotron
29.	Plot of the beta functions and the phase advance of $1/8^{\text{th}}$ of the KEK-PS booster synchrotron
30.	A schematic diagram of the KEK-digital accelerator
31.	Plot of the designed acceleration voltage and revolution period for the KEK-DA at 10 Hz operation for a fully stripped argon ion.
32.	A schematic diagram of the 8-shaped back-leg coil

33.	A schematic representation of the pulse density control
34.	A schematic diagram of the acceleration and confinement voltage pulse profile in Stage I. The confinement voltage pulses are given in pink and green, the acceleration voltage pulse in black and the bunch in red.
35.	A schematic diagram of the acceleration and confinement voltage pulse profile in Stage II . The confinement voltage pulses are given in pink and green, the acceleration voltage pulse in black and the bunch in red.
36.	A schematic diagram of the acceleration and confinement voltage pulse profile in Stage III. The confinement voltage pulses are given in pink and green, the acceleration voltage pulse in black and the bunch in red.
37.	A schematic diagram of the acceleration and confinement voltage pulse profile in Stage IV. The confinement voltage pulses are given in pink and green, the acceleration voltage pulse in black and the bunch in red.
38.	The designed acceleration voltage is shown in blue, revolution period is shown in red and the acceleration voltage provided by the induction cell throughout the acceleration period is shown in purple.
39.	Initial distribution of the argon ions for the simulations
40.	Simulation diagram
41.	A schematic diagram of the generation of the trigger timing from the bunch signal. The threshold in the bunch profile is shown in purple, and the threshold in the integrated current is shown in pink. Here 't1' and 't2' represents timing information.
42.	(a) Phase plot before the generation of the first acceleration pulse. The particles are shown in red, and the blue line shows the confinement voltage pulse (b) Phase plot after the first acceleration pulse is generated. The particles are shown in red, the blue and green line shows confinement voltage pulse and acceleration voltage pulse respectively.
43.	Pulse density until 1 msec during acceleration
44.	(a). Longitudinal phase space plot at injection. The particles are shown in red, and the blue and green lines denote the confinement voltage pulse, and the acceleration voltage pulse respectively. (b). Longitudinal phase space plot after 1.789 msec. The particles are shown in red, and the blue and green lines denote the confinement voltage pulse, and the acceleration voltage pulse respectively. (c). Longitudinal phase space plot after 10 msec. The particles are shown in red, and the blue and green lines denote the confinement voltage pulse, and the acceleration voltage pulse respectively. (d). Longitudinal phase space plot after 25 msec. The particles are shown in red, and the blue and green lines denote the confinement voltage pulse, and the acceleration voltage pulse respectively. (e). Longitudinal phase space plot after 40.77 msec. The particles are shown in red, and the blue and green lines denote the confinement voltage pulse, and the acceleration voltage pulse respectively.
45.	Survival rate and energy/nucleon ratio for argon ions over the acceleration period.
46.	Jitter amplitude of the confinement voltage pulse V/s survival rate of the argon ions over the acceleration period.
47.	Pulse voltage response of a circuit with a time constant τ

48.	Droop and undershoot in a 1-turn induction cell
49.	(a). A schematic diagram of a 1-turn and a 2-turn induction cell. (b). Induction cell with a 2-turn loop, which is implemented by a copper bar.
50.	Impedance measurement plot for a 2-turn induction cell (measured using VNA). The measured value is shown as bold lines and the calculated value as dashed lines with a capacitance value of 180pF.
51.	Temperature of the matching resistance during 1 hour of continuous operation
52.	High-voltage measurement setup.
53.	(a) A comparison of the droop and undershoot plots corresponding to the 1-turn and 2-turn configurations for pulse widths of 250 nsec and 2 μ sec.
54.	(a) SPICE simulation circuit (b) Comparison of the SPICE results and the measurement results corresponding to 2-turn cell
55.	Matching resistance inductance as measured with an LCR meter
56.	Output waveform when a serial trigger is applied to two 2-turn induction cells with a 2.2 nF capacitor connected in parallel to the feeder lines in order to reduce the overshoot.
57.	Output voltage waveform when a parallel trigger is applied to three 2-turn induction cells.
58.	Revolution period of argon +18 ions and the variation of pulse width with time.
59.	Beam simulator signal at different times of the acceleration period
60.	DSK 6416T board
61.	Stage selector DSP
62.	Clock mode
63.	Output of the stage selector DSP. Stage I signal is shown in yellow, stage II signal in green, stage III signal in blue and stage IV in pink. (b) The 10 μ sec difference between stage transition.
64.	A schematic diagram of the dynamic pulse generation using a DSP set.
65.	DSPs for the generation of long pulses
66.	A schematic representation of (a) frequency divided by 2 and (b) frequency divided by 3
67.	Frequency divider
68.	A schematic diagram of the control of the induction acceleration scheme in Stage I
69.	A schematic diagram of the control of the induction acceleration scheme in Stage II
70.	A schematic diagram of the control of the induction acceleration scheme in Stage III
71.	A schematic diagram of the control of the induction acceleration scheme in Stage IV
72.	A schematic representation of the complete induction acceleration control system
73.	A block diagram of the generation of confinement voltage
74.	Setup of the induction acceleration control system
75.	(a) Stage selector signal of Stage I and Stage II shown in pink and blue respectively and beam simulator signal is shown in yellow.

	<p>(b) Output from the induction acceleration control system in the early acceleration region of Stage I together with the set signals (pink and yellow) and reset signals (blue and green)</p> <p>(c) Output from the induction acceleration control system at 100 μsec from the start. Long pulse generation in Stage I together with set signals (pink and yellow) and reset signals (blue and green)</p> <p>(d) Output from the induction acceleration control system during the transition from Stage I to Stage II where the 10 msec sleep time is included. The set signals (pink and yellow) and reset signals (blue and green) are also shown.</p> <p>(e) Output from the induction acceleration control system at the end of Stage II. The set signals (pink and yellow) and reset signals (blue and green) are shown.</p>
76.	

List of Tables :

Table No.	Caption
1	Electrical parameters of the Induction cell
2	Specifications of the switching power supply
3	Machine parameters for the proof-of-principle experiment
4	Parameters for the calculation of the synchrotron frequency of protons.
5	Machine and lattice parameters of the KEK-PS Booster synchrotron
6	KEK-DA parameters
7	KEK-DA simulation parameters
8	2-turn cell parameters

Constants

$h=6.626 \times 10^{-34}$ J.sec	The Planck constant
$c=2.997925 \times 10^8$ m/sec	Velocity of light
$e=1.6021 \times 10^{-19}$	Electronic charge
$m_p=1.6726 \times 10^{-27}$ kg	Mass of protons
$\pi = 3.14 159$	